CONSTRAINING PARTICLE PHYSICS MODELS WITH COSMOLOGY AND ASTROPHYSICS: TWO DIFFERENT CASES

Ángel Gil Muyor

CONSTRAINING PARTICLE PHYSICS MODELS WITH COSMOLOGY AND ASTROPHYSICS: TWO DIFFERENT CASES

A thesis presented for the degree of Doctor of Physics by:

Ángel Gil Muyor

Supervisors: Luigi Delle Rose, Ricardo Zambujal Ferreira

Tutor: Alex Pomarol Clotet

May 30, 2024

Abstract

In this thesis, we have studied two different cases in which cosmological and astrophysical observables can be used to constrain extensions of the Standard Model. The first one was centered on the bubble wall dynamics at a First-Order Electroweak Phase Transition. The main achievements of this thesis regarding this topic have been the following: first, we developed a very efficient numerical method with which we could find, for the first time, the full solution of the linearized Boltzmann equation in the context of the mentioned cosmological transition. Second, we extended our method by including the equations describing the evolution of the background plasma and the bubble wall. By doing so we were able to find the value of the bubble wall velocity for a benchmark model. Third, we confirmed that the out-of-equilibrium perturbations have an important impact on the value of the bubble wall speed, so they need to be included in the analysis. The other case studied in this thesis involved the QCD axion, the particle proposed to solve the strong CP problem. In particular, we computed the luminosity resulting from the resonant conversion from axions to photons inside a superradiant cloud around a Black Hole. Regarding this project, the main achievements are the following ones: first, the method we used to compute the luminosity is analytical, is mathematically very transparent and allows to have clear quantitative and qualitative control over the assumptions. Second, we find that for Primordial Black Holes and axion masses around $10^{-5}\,M_{\odot}$, 10^{-7} eV respectively the resulting signal is so intense that it could be detected by the LOFAR telescope. Third, the mentioned values of PBH masses for which such detection could be possible match the mass range that has been used to explain some ultra-short microlensing events observed by OGLE.

Contents

List of publications

This thesis is submitted for assessment in partial fulfillment of the requirements of the PhD in Physics program at the Universitat Autònoma de Barcelona. It consists of a collection of three papers, which are listed below. After an introduction in Part I, the three papers are displayed in Part II.

[1] S. De Curtis, L. Delle Rose, A. Guiggiani, A. Gil Muyor and G. Panico, *Bubble wall dynamics at the electroweak phase transition*, *Journal of High Energy Physics* **2022** (2022)

[2] S. De Curtis, L. Delle Rose, A. Guiggiani, A. Gil Muyor and G. Panico, *Collision integrals for cosmological phase transitions*, *Journal of High Energy Physics* **2023** (2023)

[3] R. Z. Ferreira and A. Gil Muyor, *Lighten up Primordial Black Holes in the Galaxy with the QCD axion: Signals at the LOFAR Telescope*, 2404.12437

Part I
Introduction

1 Cosmological and astrophysical phenomenology of BSM models

The Standard Model of Elementary Particles (SM) has been extremely successful in explaining the smallest scales of Nature accessible to human observation, and its predictions are among the most accurate in the history of science. However, it is well known that it is not complete since it does not provide satisfying answers to several questions, like the unexpected preservation of the CP symmetry by the strong interaction (known as the Strong CP Problem) or the particle content of Dark Matter.

Many of these problems are addressed by adding new particles and/or new interactions to the Standard Model; these modifications are known as Beyond Standard Model (BSM) extensions. The efforts of physicists over the last decades to explain the open questions in the SM have led to a large population of BSM models, including supersymmetry [4], right-handed neutrinos [5], new Higgs sectors [6, 7], etc.

These BSM models need to be tested experimentally, and since most of them predict the existence of new particles, much hope was pinned on finding such new particles in collider experiments, with LHC at the forefront. However, despite the remarkable success of the discovery of the Higgs particle, no new scale of Physics has yet been found.

New experiments, like the Future Circular Collider [8], will continue the journey of colliders climbing to higher energies. However, Cosmology and Astrophysics can complement this search for new Physics. Many processes in the early and late Universe strongly depend on the BSM extension, and they are governed by extremely high energies at scales that are inaccessible for collider experiments. In addition, detecting hypothetical light and weakly coupled particles, like the axion or (possibly) Dark Matter, is especially challenging for colliders,

For this reason, the Particle Physics community has turned its attention to cosmological and astrophysical systems, trying to find new ways to probe models of microscale Physics. The recent discoveries of gravitational waves (as single events and as a stochastic signal) have been particularly exciting, as they represent a new way to look into the Universe, different from electromagnetic radiation. The prospect of combining future gravitational wave experiments, such as LISA [9, 10] or the Einstein Telescope [11], with new telescopes like the Square-Kilometer-Array [12] or CMB S4 [13], is particularly motivating, as they could finally open the door to the discovery of new Physics.

In this thesis, two different cases of cosmological and astrophysical phenomenology of BSM models have been studied. The first one is related to cosmological phase transitions. The evolution of the Universe after the Big Bang is determined by the particle content in the primordial plasma; if the SM model is modified, then the history of our Universe also changes. In particular, different BSM extensions, like the scalar singlet extension [6] or the two-Higgs doublet model [7], modify the nature of the cosmological electroweak phase transition: while according to the SM it is a continuous process where thermal equilibrium is not broken, many of these BSM extensions predict

a first-order phase transition [9], the phenomenology of which is very rich and could be used to constrain the corresponding BSM models.

Among the observational consequences of a First-Order Electroweak Phase Transition (FOEWPhT), probably the most relevant ones are the production of gravitational waves and the possibility of explaining the matter-antimatter asymmetry. First-order phase transitions take place through the nucleation of bubbles and their consequent expansion; the collision of such bubbles and their interaction with the primordial plasma lead to the production of gravitational waves, which would be measured today as a background signal [10]. On the other hand, the expansion of the bubble wall drives the plasma out of thermal equilibrium; if the particular BSM extension also provides sufficient violation of baryon number, C and CP, then the three Sakharov conditions would be fulfilled, and such a model would predict a certain amount of matter-antimatter asymmetry [14].

As we will see later, the most important parameter controlling this phenomenology is the bubble wall velocity. Intuitively, it can be expected that the gravitational wave production will be greater at higher bubble velocities, while a greater amount of matter-antimatter asymmetry will be produced if the bubble wall is slower and the transition therefore lasts longer. Then, in order to control the cosmological implications of a BSM model that predicts a FOEWPhT, it is necessary to have a reliable prediction of the bubble wall velocity.

Computing the bubble wall velocity was the main goal of the first part of the thesis. Such velocity is determined by the interaction between the bubble wall and the plasma. This interaction produces a friction force against the bubble wall, and part of such friction comes from out-of-equilibrium Physics. To find such out-of-equilibrium friction one needs to solve a Boltzmann equation, which is especially challenging in this context. In our work, we built a new efficient method to solve this equation and we proved that previous approaches, which relied on several restrictive simplifying assumptions, were not capturing correctly the out-of-equilibrium Physics. We used this method to couple the Boltzmann equation with the rest of the equations governing the transition to find the bubble wall velocity, and we checked that the out-of-equilibrium physics has a relevant impact on the prediction of the bubble wall velocity, and thus on the observational consequences of the model. This research, which will be introduced in deep detail in section 2, was developed in [1, 2], included in this thesis, but also in [15–17].

The other BSM phenomenology case studied in this thesis is related to the axion, or QCD axion[1], a field that is added to the Standard Model to solve the Strong CP Problem by dynamically relaxing the θ parameter in the QCD lagrangian, responsible for the breaking of the CP symmetry.

Although the axion was originally proposed for this purpose [18], nowadays the interest in this hypothetical particle goes beyond the Strong CP Problem. For example,

[1]In this thesis, axion is synonymous with QCD axion. If axion-like particles are discussed they will be explicitly mentioned.

thanks to the misalignment mechanism it is possible to generate a relic population of non-relativistic axions, turning this particle into a very well-motivated candidate for light cold dark matter [19].

Several experiments, like XENON [20] or the Axion Dark Matter Experiment [21], have been putting a lot of effort into trying to discover the axion, but there is no positive detection for the moment. Again, as we said before, these efforts can be complemented with other cosmological and astrophysical searches. In this thesis, we have studied the possibility of detecting with Earth-based telescopes the flux of photons resulting from the axion-photon conversion in a superradiant cloud around a rotating Black Hole. Inspired by the formalism used in the literature to study the resonant conversion around neutron stars [22–28], we developed a new method to compute the luminosity of the mentioned system. Using such a method we obtained an analytical expression of the luminosity, and we found out that, for Primordial Black Holes (PBHs) and an axion with masses around $10^{-5}\ M_\odot$, 10^{-7} eV respectively, the luminosity through axion-photon conversion is high enough for it to be detected with the LOFAR radiotelescope. In addition, this same range of PBH mass is the one used to explain some microlensing events measured by the OGLE experiment [29]. We will give an extended introduction about this work, published in [3], in section 3.

At the end of the present Part I of this document, we conclude with the main achievements of the work done in this thesis and we outline some possible future lines of research. In Part II we include the articles [1–3], which constitute the main body of this thesis.

Throughout this document we use natural units fixing $c = \hbar = k_B = \epsilon_0 = 1$, and we choose $(+ - - -)$ as the signature for the Minkowski metric.

2 Bubble wall dynamics during a First-Order Electroweak Phase Transition

Among the two cases of BSM phenomenology studied in this thesis, we start with the FOEWPhT. In particular, we have focused on the computation of the velocity of the bubble wall, a parameter that plays a key role in the observational consequences of such a process. We were able to compute this velocity thanks to our development of a new method to find the full solution of the Boltzmann equation, which we also used to evaluate the effect of out-of-equilibrium physics on the value of the bubble wall velocity. This work of research was published in [1,2]. A continuation of this work was published in [17], which is not included in this thesis but will be summarized in section 5.

The goal of this section is to give an explanatory introduction and to motivate the work done in this thesis, providing the required context together with a (non-exhaustive) revision of related literature. In 2.1 we give a brief introduction to spontaneous electroweak symmetry breaking. In 2.2 we explain the electroweak phase tran-

sition, which is the cosmological context in which such symmetry breaking took place. We explain the phenomenological interest in the case of a FOEWPhT in section 2.3, focusing on gravitational wave production and Baryogenesis. In section 2.4 we explain the formalism we use to deal with the relevant ingredients for studying the dynamics of the transition: the bubble wall profile, the out-of-equilibrium perturbations, and the background plasma in local equilibrium.

2.1 Electroweak symmetry breaking

The spontaneous breaking of symmetries is one of the most important aspects of the Standard Model of Elementry Particles. This phenomenon is based on the idea that, even if a theory respects a given symmetry, some states described by that theory do not need to respect such symmetry. Yoichiro Nambu introduced spontaneous symmetry breaking in the realm of Particle Physics; inspired by his knowledge of Condensed Matter Physics, Nambu explained how the spontaneous breaking of a chiral symmetry leads to a spectrum of massive composite bosons [30]. This same idea is used in the Standard Model to explain why the mass of the hadrons is much bigger than the sum of the mass of the quarks.

The Higgs Mechanism is another crucial application of spontaneous symmetry breaking in the Standard Model of Elementary Particles. In the famous *1964 PRL symmetry breaking papers* [31–33], three different research groups used the idea introduced by Nambu some years before, but in this case in the context of gauge theories. They discovered that gauge bosons, which in principle need to be massless to respect the gauge symmetry itself, can acquire a mass if the theory contains a particle that takes a non-zero vacuum expectation value, i.e. a particle whose vacuum state spontaneously breaks a gauge symmetry[2].

In the SM, the Higgs mechanism is used to explain the origin of the mass of the $W^{\pm}$, Z bosons, which correspond to the gauge bosons of the weak interaction, whose symmetry group is $SU(2)$. The Higgs mechanism is needed also to explain the origin of the mass of the fermions in the SM since their bare mass terms also break the $SU(2)$ symmetry. In this context, the symmetry breaking required by the Higgs Mechanism corresponds to the Electroweak symmetry breaking (EWSB), which has been central in this thesis and on which we will focus from now during in this section.

Ignoring the QCD sector, the SM can be written as a gauge theory with $SU(2) \times U(1)$ as a gauge group. This is the so-called electroweak unification, and the corresponding Lagrangian is

$$\mathcal{L} = -\frac{1}{4}W^i_{\mu\nu}W^{i,\mu\nu} - \frac{1}{4}B_{\mu\nu}B^{\mu\nu} + i\bar{\psi}_L \not{D}\psi_L + i\bar{\psi}_R \not{D}\psi_R + |D_\mu h|^2 - V_0(h) + \mathcal{L}_Y \ , \quad (1)$$

[2]This statement is not completely correct from a formal point of view; Elitzur's theorem states that gauge symmetries can never be spontaneously broken [34]. However, the Higgs mechanism can be deduced in a completely gauge-invariant way in the so-called FMS framework [35].

where we called ψ_L the fermions that behave as doublets under the $SU(2)$ group, or *left-handed fermions*, and ψ_R the fermions that behave as singlets under $SU(2)$, or *right-handed fermions*. $W^i_{\mu\nu}$, $B_{\mu\nu}$ are the gauge tensor fields corresponding to the $SU(2)$ and the $U(1)$ gauge groups, respectively. The covariant derivative associated with these gauge groups is D_μ. Finally, h is the Higgs boson, which acts as a doublet under $SU(2)$ and has charge $1/2$ under $U(1)$ transformations, and is responsible for the EWSB. We also included a potential term $V_0(h)$ for the Higgs field. Finally, $\mathcal{L}_Y$ stands for the interactions between the fermions and the Higgs boson.

Let us now rewrite the Higgs field in the following way [36]:

$$h(x) = U(x)\frac{1}{\sqrt{2}}\begin{pmatrix}0\\ v+H(x)\end{pmatrix} \equiv U(x)\frac{1}{\sqrt{2}}\begin{pmatrix}0\\ h_2(x)\end{pmatrix} \ . \tag{2}$$

We added the matrix $U(x)$ to write the most general two-component spinor, but it can be removed from the Lagragian by a gauge transformation [36]. $H(x)$ is defined as a real scalar field fulfilling $\langle H(x)\rangle = 0$, so by construction $\langle h_2(x)\rangle = v$, $\langle h(x)\rangle = (0, v/\sqrt{2})$. Of course, the value of the vacuum expectation value v will depend on the potential $V_0(h)$. With this parametrization, we can rewrite the lagrangian 1 in terms of v and $H(x)$ instead of $h(x)$. This of course mixes the components of the left-handed doublets with the right-handed singlets, in such a way that several quadratic terms appear. In the same way, due to the interaction of the Higgs field with the gauge bosons through the covariant derivative, there appear also quadratic terms mixing different gauge bosons. All these terms can be written like

$$\mathcal{L}_{\text{mass}} = \sum_X -(y_X v)\bar{X}X + \sum_A -(y_A v)^2 A_\mu A^\mu \ . \tag{3}$$

The fermions X and the bosons A in 3 are defined as a particular recombination of the fermions and bosons in 1, and $y_{X,A}$ are constants which depend on the coupling constants of 1. This is how the Higgs mechanism generates masses for fermions and bosons: if $v \neq 0$, then we can redefine our fields in terms of the *mass states* in 3, where $m_{X,A} = y_{X,A}v$.

Notice that the Higgs mechanism is able to generate mass terms for the particle without explicitly breaking the gauge symmetry; when we rewrite the Lagrangian using 2, shuffling the gauge bosons and the components of the fermions doublets and singlets, we are not removing the gauge symmetry, we are just hiding it. This is why it is more enlightening to use the expression *hidden symmetry* rather than spontaneously broken symmetry.

It is also important to notice that the description in terms of the mass states is always valid, even if $v = 0$; in this thesis, the presence of the bubble implies that the value of v will change in time and/or space from zero to a non-zero value, which will imply a position/time-dependent mass for the particles: outside the bubble, the particles will be massless, and they will be massive inside. This will be explained in more detail in the following sections.

2.2 Cosmological Electroweak phase transition

Electroweak symmetry breaking, as well as other symmetry-breaking processes, are crucial for Cosmology. As we said, the vacuum expectation value of the Higgs field, responsible for the mass terms of all the SM fundamental fields, depends on the potential $V_0(h)$ in 1. However, to be completely precise we should take into account the interaction of the Higgs boson with the rest of the particles in the model. If we consider a system where the average number of interactions among the particles is very low (which we can call a system with *zero temperature*), then the Higgs vev will be determined by $V_0(h)$ (ignoring radiative corrections), but what if that is not the case? What if the average number of interactions per unit of time between the particles and the Higgs is not that small and so the temperature is different from zero?

Cosmology gives a perfect context where these questions are relevant. We know that in the Early Universe the rate of interactions between particles was very high. This fact can be modeled through temperature, and so we say that the particles in the Early Universe lived in a *thermal bath* with a temperature determined by the expansion history. Is it possible that at some point the temperature of the Early Universe was so high that the vev of the Higgs was zero and so the particles were massless, i.e. a temperature where the EW symmetry was *restored*? If that was the case, then at some point, as the Universe was cooling down, the temperature was low enough such that the vev of the Higgs changed from zero to a non-zero value, giving mass to the elementary particles.

We can anticipate that the answer to the question raised in the previous paragraph is yes, and it yields the so-called *Cosmological Electroweak Phase Transition*, which has been the subject of study in this thesis. To be able to study this physics properly, to know which is the temperature in which such transition happens and what are its properties, it is useful to use the machinery of *Thermal Field Theory*.

With the tools of Thermal Field Theory one can compute the thermal correction $V_T(T,h)$ to the potential $V_0(h)$, so the total potential is[3] $V(T,h) = V_0(h) + V_T(T,h)$. The shape of this potential will be crucial for the nature of the phase transition. We will now depict the computation of $V_T(T,h)$; more details can be found in [37, 38].

From now on we will consider that the primordial plasma hosting the phase transition is weakly coupled. This means that we will treat the collisions among particles in the plasma perturbatively. This is justified in the case of the electroweak phase transition. However, the formalism explained in this thesis cannot be applied to FOPhT within a strongly coupled plasma, which is the case of the QCD phase transition. In that case, holography is a more suitable tool to find the friction against the bubble wall and its velocity [39].

Let us consider a free bosonic or fermionic field of mass m in a thermal bath of

[3]The thermal correction is not the only relevant modification to the zero-temperature potential; one-loop corrections, for example, have an important quantitative impact on the Higgs potential [37]. This correction has been taken into account in the works included in this thesis, but we ignore them in this introduction for the sake of simplicity.

temperature T. The goal is to compute the thermodynamic free energy density of such fields, as it represents the exchange of energy between the field and the thermal bath. Since the mass of these particles depends on the value of the Higgs field h_2, this energy exchange with the thermal bath represents also the energy that the Higgs field h can extract from the thermal bath, i.e. $V_T(T,h)$.

Fermionic and bosonic fields can be decomposed in a sum of infinite harmonic oscillators; for instance, for the boson field ψ,

$$\psi(t,\vec{x}) = \int \frac{d^3k}{(2\pi)^3}\frac{1}{2E_k}\left(a_{\vec{k}}e^{i\vec{k}\vec{x}} + b^\dagger_{\vec{k}}e^{-i\vec{k}\vec{x}}\right) \ , \tag{4}$$

where $E_k^2 = |\vec{k}|^2 + m^2$. The analogous expression for the fermion field is similar, but in that case it is necessary to introduce the Dirac spinors. Since we are considering free fields, the corresponding equations of motions do not couple different $\vec{k}$ modes. Then, the free energy density of such free fields is the sum of the free energy of all possible modes, normalized with the volume of the phase space. Each mode is a decoupled harmonic oscillator, whose free energy is [38]

$$F_{\text{ho}} = \pm\frac{E_k}{2} \pm T\ln(1\mp e^{-\beta E_k}) \ , \tag{5}$$

where $\beta = 1/T$. The upper sign corresponds to the bosonic case, and the lower sign to the fermionic one. Then, the free energy arising from a fermionic or bosonic field is (assuming some regularization of the divergent ground state energy $E_k/2$ [37])

$$\begin{aligned} f_{\text{B,F}} &= \pm T\int\frac{d^3k}{(2\pi)^3}\ln(1\mp e^{-\beta E_k}) = \\ &= \pm\frac{T^4}{2\pi^2}\int dx\ x^2\ln\left(1\mp e^{-\sqrt{x^2+(m/T)^2}}\right) \equiv \frac{T^4}{2\pi^2}J_{\text{B,F}}\left(\frac{m}{T}\right) \ . \end{aligned} \tag{6}$$

The dimensionless functions $J_{\text{B,F}}$ are called thermal bosonic/fermionic functions. It is important to note that 6 corresponds to the free energy of each degree of freedom; for example, a Dirac field has four degrees of freedom, so the contribution to the total free energy by a single Dirac field is $4f_F$. If we recall now that the masses of the fields in the thermal bath depend on the vev of the Higgs field, we can find the thermal correction V_T to the tree-level potential $V_0(h)$:

$$V(T,h) = V_0(h) + V_T(T,h) = V_0(h) + \frac{T^4}{2\pi^2}\left(\sum_{\text{B dof}} J_{\text{B}}\left(\frac{y_i h}{T}\right) + \sum_{\text{F dof}} J_{\text{F}}\left(\frac{y_i h}{T}\right)\right) \ , \tag{7}$$

where the sum is over the bosonic and fermionic degrees of freedom and $m_i = y_i h_2$ is the field-dependent mass of each particle.

Now that we have the potential including the thermal correction we can start to address the questions that we raised before. The first one is if the electroweak symmetry

is restored at high temperatures. For high temperatures, we can expand the thermal functions J around zero; it happens that such expansion does not include linear terms, so the potential will behave like

$$V(T,h) \sim V_0(h) + CT^4 + DT^2h^2 + T^4\mathcal{O}\left(\left(\frac{h}{T}\right)^3\right) \tag{8}$$

for some constants C, D. For arbitrarily high temperatures, the tree-level potential $V_0(h)$ is arbitrarily negligible. The potential then behaves quadratically in h, which implies that its minimum is at $h = 0$ (assuming D is positive). Then, as we anticipated before, we can be sure that at some temperature the Higgs vev is $h = 0$ and then the EW symmetry is restored.

The next issue we need to address is *when*, or at what temperature, does this change, since it is crucial in order to determine how the transition took place. A necessary condition (although not sufficient) for this to happen is that at some temperature T_c a new minimum appears whose energy is equal to $V(T_c, 0)$. This means that T_c is the solution of the system

$$\begin{cases} \partial_h V(T_c, h_0) = 0 \\ V(T_c, h_0) = V(T_c, 0)\ . \end{cases} \tag{9}$$

The temperature T_c is called the *critical temperature*. As the Universe cools down, $T < T_c$, the true vacuum of the Higgs will not be $h = 0$, but the other value of h fulfilling $\partial_h V(T, h_0) = 0$, $V(T, h_0) < V(T_c, 0)$ (note that the position of the new true vacuum depends on the temperature, and changes its value as the Universe temperature drops). Although we have not imposed it, the second condition in 9 enforces that the solution of the system (or at least one of them) will be an absolute minimum, and not a local maximum[4].

The critical temperature T_c is not necessarily the temperature at which the transition occurs. This question is directly related to the type of phase transition taking place, and we shall address it now.

Phase transitions can be classified into two types: first-order phase transitions or continuous phase transitions. The main difference between both is related to the latent heat [40]: in a continuous phase transition, the change of state happens continuously so no latent heat is released. The previous stable state is unstable below T_c, so at every point in space the field rolls down to the new vacuum. Instead, in a first-order phase transition the previous state is metastable; both phases can coexist during some period of time, although the new one is energetically favored. Some parts of the Universe transition to the new favored state in the form of *bubbles*, as we shall discuss later. The difference in potential energy between the stable and the metastable state ΔV (the latent heat) is released as kinetic energy that yields the expansion of the bubbles,

[4]We are assuming that the potential $V(T, h)$ is a differentiable function.

until the whole Universe is covered in the new stable phase. This is the type of phase transition studied in detail in this thesis.

As we said, both types of phase transitions are distinguished in the possibility of coexistence of both states, which is directly related to the difference between the previous stable state being unstable or metastable for temperatures below T_c. In terms of the potential, the minimum before the transition at $h = 0$ is metastable for $T \leq T_c$ if $\partial_h^2 V(T_c, 0) > 0$, and is unstable if $\partial_h^2 V(T_c, 0) < 0$. This implies that, if the transition is first-order, at $T = T_c$, when the new minimum appears, there is a potential barrier separating both the previous and the new minimum.

We can conclude that continuous phase transitions happen at $T = T_c$ since the previous minimum becomes unstable and the field rolls down to the new minimum. However, what about first-order transitions? If at $T = T_c$ there is a potential barrier separating two minima, the field needs to overcome such barrier by quantum tunneling or by thermal fluctuations. The transition between the degenerate minima should then be suppressed (we can foresee that such suppression should depend on the height of the potential barrier and the potential difference between the 2 minima). At which temperature and how will the transition happen in that case?

This issue was addressed by Coleman [41, 42] and later applied to the specific case of the Cosmological EW Phase transition by Linde [43]. Let us assume we have a Higgs field permeating the space, sitting in the metastable state $h = 0$. We will use a path integral formalism; the partition function is

$$\mathcal{Z}_\beta = \int \mathcal{D}\pi \mathcal{D}h e^{-\beta H[\pi,h]} = \mathcal{N} \int \mathcal{D}h e^{-\beta E[h]} \, . \tag{10}$$

H is the Hamiltonian for the field h, including the thermal potential. In the second equality we have integrated out the canonical momentum variable, so

$$E[h] = \int d^3x \left(\frac{1}{2} (\nabla h)^2 + V(T, h) \right) \tag{11}$$

The probability per unit of time and volume $\Gamma/\mathcal{V}$ for the field to transition to a $h = h_0$ is computed using a saddle point approximation, which means that one needs to find field configurations corresponding to minima and maxima of the functional $E[h]$. It can be seen that the field configurations minimizing $E[h]$ are spherically symmetric [38]. This is why we talk about bubbles when dealing with first-order phase transitions: the transition will happen through the nucleation of spherical bubbles of the new stable state or *true vacuum*, in terms used by Coleman.

However, not every bubble nucleation process will lead to the phase transition; if the nucleated bubbles are too small, they will shrink due to the surface tension and disappear. We can check this by computing the energy difference between the bubble configuration and the constant $h = 0$ configuration. If we assume that the transition will happen shortly after T_c, so the height of the potential barrier will be much bigger than the potential difference $\Delta V = V(T, 0) - V(T, h_0)$. In that case,

the field configuration needs to change rapidly from $h = 0$ inside the bubble to $h = 0$ outside; this is called the *thin wall limit*. In this limit, the difference in energy $E[\bar{h}] - E[h = 0]$ between a bubble configuration of radius R and the constant $h = 0$ can be simplified to [44, 45].

$$E[\bar{h}] - E[h = 0] = 4\pi\sigma R^2 - \frac{4\pi}{3}\Delta V R^3 \ . \tag{12}$$

In 12 the first term can be understood as the work done by the surface tension σ (which value depends mainly on the height of the potential barrier), while the second one is the work done by the inner pressure of the bubble, which energy comes from the energy released after transitioning to the true vacuum, i.e. ΔV.

The energy in 12 has a maximum at $R_c = 2\sigma/\Delta V$. If the radius of the nucleated bubble is smaller than R_c, the bubble will minimize its energy shrinking until disappearing, while if the nucleated bubble has a radius bigger than R_c the bubble will expand; a bubble with the *critical radius* R_c is called a *critical bubble*.

The energy associated to a critical bubble configuration is

$$E_c \equiv \left(4\pi\sigma R^2 - \frac{4\pi}{3}\Delta V R^3\right)\Big|_{R=R_c} = \frac{16\pi\sigma^3}{3(\Delta V)^2} \tag{13}$$

The probability of nucleation of a critical bubble per unit time and volume is [37]

$$\frac{\Gamma}{\mathcal{V}} \sim T^4 e^{-E_c/T} \ . \tag{14}$$

The transition will take place once the probability of nucleating a critical bubble is high enough. A reasonable choice is to set as the *nucleation temperature* T_n the temperature at which the probability of nucleating a bubble in a Hubble volume H^{-3} (H stands for the Hubble constant) within a Hubble time H^{-1} is one, i.e. at $T = T_n$

$$H^4(T_n) = \left.\frac{\Gamma}{\mathcal{V}}\right|_{T=T_n} \tag{15}$$

We can summarize the discussion of the previous paragraphs in the following way: there exists a critical temperature T_c at which a new degenerate minimum different from $h = 0$ appears for the Higgs potential. If at such temperature there is no potential barrier between the two minima, the phase transition will be a continuous one, taking place at $T = T_c$. If otherwise there is a potential barrier, then the Universe will enter a metastable state until the nucleation temperature T_n, at which bubbles of the new stable nucleate across the Universe.

What happens then for the Standard Model? If we assume we know the Higgs potential at every temperature, then we can compute T_c and also the sign of $\partial_h^2 V(T_c, 0)$, to tell which type of phase transition takes place. This allows to draw a phase diagram in terms of the measured Higgs mass and the critical temperature, which is displayed in Fig. 2. The values of the Standard Model lie beyond the critical point, so according

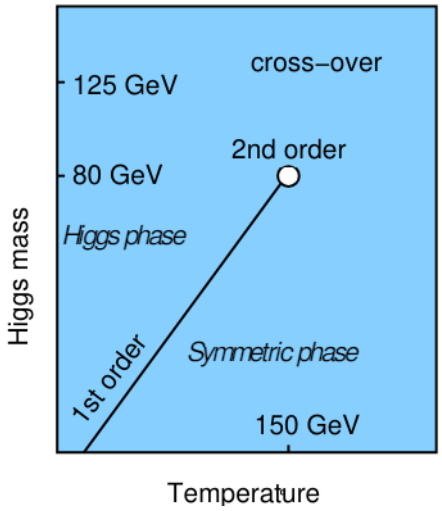

Figure 2: Phase diagram for the Electroweak phase transition in terms of the measured Higgs mass, according to the Standard Model. If the Higgs mass is above 80 GeV then such transition is continuous; this is the case since the Higgs mass is around 125 GeV. Figure taken from [38].

to such theory the cosmological EW phase transition was a continuous one. However, there are still many reasons to study the possibility of a first-order EW phase transition. In the next section we will motivate such a study, giving some details on some phenomenological consequences.

2.3 Why is a First-Order Electroweak Phase Transition interesting?

As mentioned in the introduction, there are many reasons to believe that the Standard Model is an incomplete description of Nature. Some of the most relevant unexplained observations, like the presence of Dark Matter, the matter-antimatter asymmetry in the Universe or the CP symmetry conservation by the strong interaction are often solved by extending the Standard Model, including new interaction terms or new particles. Some of the most popular extensions of the Standard Model, which are proposed to solve such issues, include a new scalar singlet coupled to the Higgs field [6] or a new Higgs doublet (the Two-Higgs-doublet model or "2HDM") [7].

These BSM modifications would have a relevant impact on the thermal history of our Universe, altering the predictions made by the Standard Model; if the Higgs sector is modified, the nature of the cosmological EW phase transition could change dramatically. Indeed, according to many of these extensions, a first-order EW phase transition took place in the Early Universe. A review of many BSM models predicting such a transition can be found in [9].

Probing such models can be challenging for collider experiments. For instance, in

some of these models the new particles have sizable coupling to the SM Higgs field, but interact only indirectly with the rest of the particles. It is then important to look for alternative ways of exploring such models, such as the imprints of their cosmological history on the present Universe. This sets a motivating and exciting prospect for the future of Physics, where collider and cosmological experiments can complement each other in the mission of finding new phenomena.

In the rest of this section we shall briefly discuss two of the most relevant phenomenological consequences of such models, in the context of Cosmology; the production of a gravitational wave background and the generation of matter-antimatter asymmetry, a.k.a. Baryogenesis.

2.3.1 Gravitational wave background

A first-order phase transition takes place through the nucleation of bubbles of the true vacuum, and the difference in energy turns into kinetic energy for the bubble wall, which expands through the primordial plasma until they collide with each other and the true vacuum state covers the whole space. During such expansion, the bubble wall interacts with the plasma, depositing part of its energy in the form of heat and bulk kinetic energy, which takes the form of sound waves traveling across the plasma.

Although the bubble expansion is a spherically symmetric process, their collisions and the plasma motion are very energetic and highly non-spherical. This will lead to the production of gravitational waves. Since the Hubble patches were causally disconnected back then, such gravitational waves would be measured today as a gravitational wave background, or a stochastic gravitational wave spectrum[5]. This means that BSM models predicting first-order phase transitions could be probed using Gravitational Wave detectors, either by already-built ones like LIGO, Virgo, or KAGRA or future ones like LISA or the Einstein Telescope.

In the context of a first-order phase transition there are three main contributions to the production of gravitational waves: the collision of bubble walls, the collision of sound waves, and the turbulent motion of the plasma produced by the motion of the bubble front. In this way we can write

$$\Omega_{\mathrm{GW}} = \Omega_{\mathrm{GW}}^{\mathrm{bw}} + \Omega_{\mathrm{GW}}^{\mathrm{sw}} + \Omega_{\mathrm{GW}}^{\mathrm{turb}} \ , \tag{16}$$

where each term stands for the energy contribution in the form of GW from each of the sources respectively.

It is challenging to do a general analysis of each of the contributions in 16; most of the studies on this issue are based on involved simulations of the transitions (e.g. [46–48]). However, the shape of the GW spectrum produced is thought to depend on

[5]The author of this thesis once assisted to a talk given by Daniel G. Figueroa, one of the most relevant figures in this field, and strongly agreed with him when he discouraged using the expression *stochastic gravitational wave background* or SGWB since the terms *stochastic* and *background* are redundant.

only a few parameters of the transition, namely the transition strength α (related to the latent heat released in the transition ΔV), the duration of the transition β^{-1}, the nucleation temperature T_n and the bubble wall velocity v_w. [10,38,49]. If the transition entered a runaway regime and the bubble wall accelerated to velocities very close to the speed of light, most of the energy would be concentrated at the bubble front and 16 would then be dominated by $\Omega_{\rm GW}^{\rm bw}$. However, for most of the typical values of the transition parameters the bubble wall is expected to achieve a constant velocity below c. In this case, an important part of the available energy is transferred to the plasma. This produces energetic sound waves traveling across the plasma, the collision of which has been found to produce GW well after the end of the phase transition when all the bubbles have collided. This means that, for the typical region of the parameter space, $\Omega_{\rm GW}^{\rm sw}$ is the dominant term in 16 [10].

As mentioned before, the GW power spectrum is expected to depend only on α, β, T_n and v_w. This means that the position and the amplitude of the peak frequency in the power spectrum will depend on such values; however, there is something special about the parameter v_w: it does not only affect the position and the amplitude of the peak, but it also affects the shape of the power spectrum (see Fig. 3). Therefore the bubble wall velocity would be the best determined parameter if a GW background was detected. This means that to efficiently test BSM models, it is crucial to have control over the prediction of v_w made by such models.

In the particular case of the EW phase transition, the frequency peak is expected to be around $10^{-4} - 10^{-3}$ Hz. This frequency range is of interest for LISA, a future space-based GW interferometer, which will operate in the frequency range $10^{-4} - 1$ Hz starting next decade. LISA will be able to test, through the (possible) detection of GW of cosmological origin, new models of microscale Physics.

2.3.2 Baryogenesis

It is an observational fact that the Universe contains much more matter than anti-matter. No anti-baryonic structures are found in the Universe, and even the only few detections of antiparticles coming from space can be explained by a Universe filled only with matter [51]. It is natural to assume that the initial conditions of our Universe included an equal amount of matter and antimatter, so we expect that at some point during the history of the Universe a large asymmetry was produced, leading to current observations. Such a process is called *Baryogenesis* (since normally the solution to the problem focuses on the production of baryons over anti-baryons), and a FOEWPhT provides a suitable cosmological context where it can take place.

In 1967, Andrei D. Sakharov[6] established the conditions required for Baryogenesis, famously known as *Sakharov conditions* [52]. In this section we shall explain what are these conditions, and why a FOEWPhT is a well-motivated candidate.

[6]It is always worth mentioning that Sakharov was awarded the Nobel Peace Prize for his Human Rights activism, reminding us that even if we study the smallest and largest scales of Nature, there are some scales in the middle that may also be relevant.

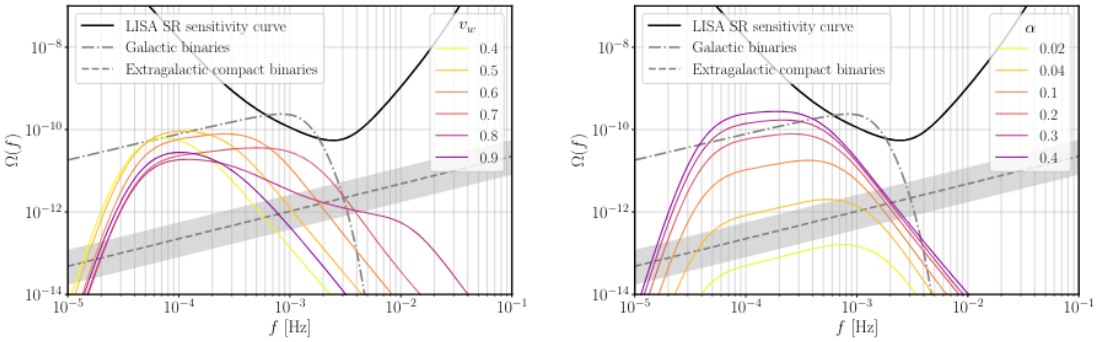

(a) Fixed: $\alpha = 0.2$, $r_* = 0.1$, $T_\mathrm{n} = 100$ GeV. (b) Fixed: $v_\mathrm{w} = 0.6$, $r_* = 0.1$, $T_\mathrm{n} = 100$ GeV.

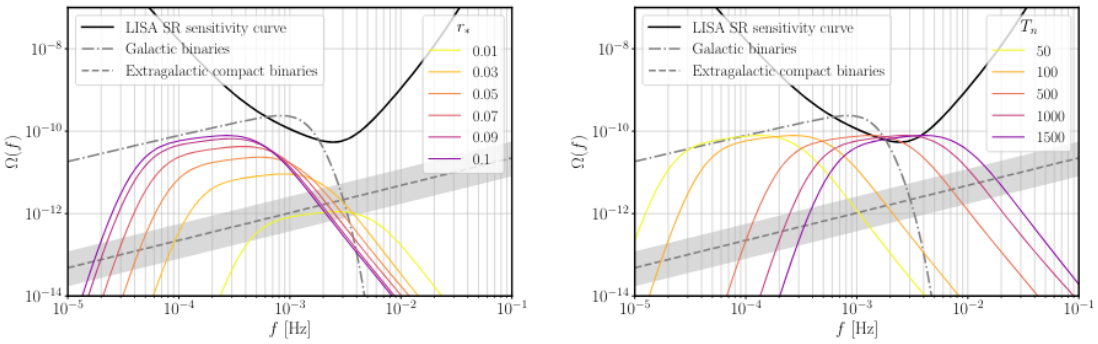

(c) Fixed: $v_\mathrm{w} = 0.6$, $\alpha = 0.2$, $T_\mathrm{n} = 100$ GeV. (d) Fixed: $v_\mathrm{w} = 0.6$, $\alpha = 0.2$, $r_* = 0.1$.

Figure 3: Gravitational wave power spectra predicted in [50], varying the values of the four relevant parameters: the strength of the phase transition α, the nucleation temperature T_n, the bubble wall velocity v_w and the Hubble-scaled bubble spacing r_* (which is determined by v_w and the duration of the transition β^{-1}). One can see that while varying the parameters changes the position and the height of the peak frequency, in particular changing the bubble wall velocity also affects the shape of the spectrum.

The three Sakharov conditions are the following ones:

- **B-nonconserving interactions**: if we need to generate an asymmetric population of baryons and anti-baryons, we need interactions that do not conserve the baryonic number B. The Standard Model provides such interaction: since the gauge group of the electroweak interaction is non-abelian (it includes an $SU(2)$ group), we know that the topological structure of the vacuum is non-trivial, and there are many possible vacua. Each different vacuum is labeled by a different value of the number $B + L$ while conserving $B - L$, where L is the leptonic number: going from one vacuum to a neighbor one changes 3 baryons for 3 antileptons (or 3 antibaryons for 3 leptons) [53]. Then, field configurations that interpolate between vacua allow changes in the $B + L$ number. If the mechanism from changing between vacua is quantum tunneling, such solutions are called *instantons*. However, thermal fluctuations also allow to overcome the energy difference between the vacua; these solutions that connect different vacua without tunneling through the barrier are called *sphalerons*.

- **C and CP violation**: In addition to the B violation, we also need the C symmetry not to be conserved. Otherwise we would exchange as many particles for antiparticles as antiparticles for particles. In the same sense, we need CP violation to avoid that the change from left-handed particles to right-handed antiparticles is the same as the change from right-handed antiparticles to left-handed particles. It is known that the Standard Model does not provide enough C and CP violation to generate the required matter-antimatter asymmetry, so some BSM extension is required in order to have Baryogenesis [10].

- **Departure from thermal equilibrium**: If the Universe was constantly in thermal equilibrium, the rate of any process generating a net gain in B would be, by definition of equilibrium, the same as the rate of the opposite process. If the Universe started being matter-antimatter symmetric, thermal equilibrium would wash out any generated asymmetry.

A first-order EW phase transition provides a scenario where the third condition is fulfilled, since the bubble expansion drives the primordial plasma out of equilibrium. The BSM extension required to have a first-order transition can also be responsible for generating the required C and CP violation [14]. We need then to discuss the first condition, the B-nonconserving interactions. At the scale of the EW transition, barrier penetration is highly suppressed, so the instanton solution is not useful [37]. However, since the temperature is high, sphalerons are very efficient, so B-violating interactions are very common. We can do a rough guess stating that the sphaleron rate Γ_{sph} should behave like $\Gamma_{\text{sph}} \sim e^{-E_{\text{sph}}/T}$, where E_{sph} is the energy of the sphaleron solution, which we can expect to depend on the height of the energy barrier between different vacua, which in turn will grow with the Higgs vev h_0 [53]. Therefore inside the bubbles, where $h_0 \neq 0$, the sphaleron rate will be rapidly suppressed. Then, as

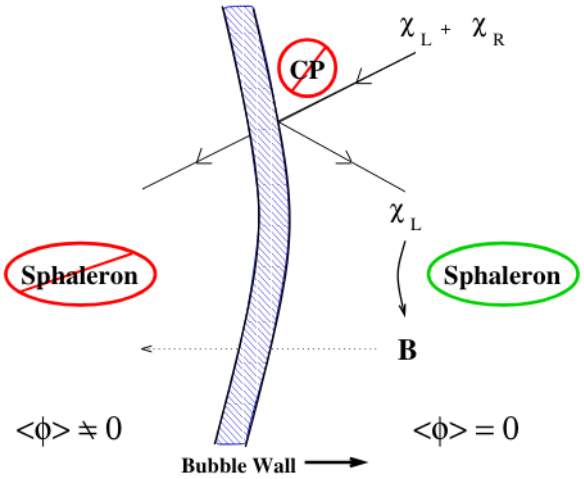

Figure 4: Summary of the Baryogenesis process during a first-order EW phase transitions. $\langle\phi\rangle$ stands for the Higgs vev. Drawing taken from [14].

sphalerons generate matter-antimatter asymmetry, part of that asymmetry will leak inside the bubble, where it will stay conserved since sphalerons are frozen. Fig. 4 displays a summary of this process.

The bubble wall velocity plays a crucial role in this process. If v_w is too small, there will be not enough departure from equilibrium to have Baryogenesis. If it is too big, there will not be enough time to generate the required amount of asymmetry. If one wants to use a BSM model predicting a FOEWPhT to explain the observed matter-antimatter asymmetry in our Universe, then one needs to have a reliable prediction of the value of the bubble wall velocity, as was the case for the GW power spectrum.

We conclude that to control the phenomenology of a BSM first-order phase transition, knowing the bubble wall velocity is critical. The computation of the bubble wall velocity v_w is especially challenging since it depends on the out-of-equilibrium Physics during the transition. One of the main goals of this thesis has been the development of a method to obtain reliable prediction of v_w, as well as evaluating the impact of the aforementioned out-of-equilibrium effects. In the next section we will discuss how to deal with the bubble wall dynamics to find v_w.

2.4 Bubble wall dynamics

In this section we study the dynamics of the bubble wall, with a particular focus on finding its velocity. We will discuss what mechanisms are relevant for such a computation and introduce the formalism used in this thesis. We will also discuss the methodology that was in use before the start of this thesis, to motivate the work developed in [1, 2], included in this document.

The general picture is as follows: during the Early Universe, at very high temperatures $T > T_c$, the EW symmetry was not broken. At $T = T_c$, another minimum in

the Higgs potential becomes degenerate with the symmetry-preserving one, and both minima are separated by a potential barrier (since we assume that the transition was first order). The Universe enters a metastable state until $T = T_n$, the moment when the energy difference between the minima is high enough so bubbles of the true vacuum state are nucleated. Such energy difference forces the bubble to expand. The bubble wall travels across the primordial plasma, driving it out of equilibrium and accumulating energy in front of it, which in turn acts as a source of friction for the expansion of the bubble wall. This changes the temperature and velocity of the plasma which is being pushed by the bubble, creating sound waves, also known as shock waves. The friction force against the bubble wall will compensate for the expansion driving force, bringing the bubble wall to a steady state of constant velocity.

With this picture in mind, we can divide our system into three different components. First, there is the bubble wall profile, which can be modeled as a scalar field representing the value of the Higgs vev at each position. This means that it is a mapping between the symmetry-preserving value of the Higgs vev in front of the bubble wall and the symmetry-breaking one behind it The bubble wall profile will be governed by a Klein-Gordon-like equation. The other components are related to the primordial plasma, which can be split in two: the part of the plasma which is in equilibrium, and the part which is out of it. Both components will be described by statistical distribution functions; the equilibrium part will be described by the energy and momentum conservation equations, and the out-of-equilibrium part will follow a Boltzmann Equation.

The three equations described above are not independent, and to fully solve the system one needs to solve the three of them simultaneously, as we did in [2]. In the next sections we will describe in more detail each of the components, and how each equation can be solved assuming the solutions of the others are known. We will focus especially on the Boltzmann equation which has received most of the effort done in this thesis and which was the main subject in [1].

From now on we will treat the bubble wall as a flat object, which is known as the *planar limit*. This limit implicitly assumes that the width of the bubble is much smaller than its radius, which is a safe assumption since we are considering the bubbles to be at least as big as the critical ones [45]. We will consider such a planar object to move in the z direction, which implies that the only relevant spatial variable for all the magnitudes involved in the problem is z, and they will be axially symmetric. For example, the dependence of the magnitudes on the momentum $\vec{p}$ will only appear through the dependence on the projection in the z direction, p_z, and the perpendicular component $p_\perp$.

Let us set now some notation. We will treat the bubble wall profile as a scalar classical field $\phi(z)$ (note the difference between ϕ and h; ϕ represents the vev of the field h, in such a way that the Higgs particles are perturbations of the field h around the background ϕ). Each particle degree of freedom in the plasma will be described with a statistical distribution function $f = f_v + \delta f$, where f_v represents the equilib-

rium distribution function and δf is the deviation from equilibrium. the subindex v represents the velocity of the plasma, which will depend on the reference frame. We will consider two possible frames: the *wall frame*, where the bubble wall velocity is zero and the plasma is moving towards it, and the *plasma frame*, where the plasma velocity is zero and the bubble wall is traveling across it. Unfortunately, there might be some inconsistency between this notation and the one in some of the works included in this thesis.

2.4.1 Scalar field Equation

The bubble wall is modeled as a scalar field $\phi(z)$ and so it follows a Klein-Gordon equation with the Higgs potential $V(T,\phi)$. Ignoring the Higgs perturbation over this vev,

$$\Box\phi + \partial_\phi V(T,\phi) = 0 \ . \tag{17}$$

Let us split the Higgs potential into V_0 and V_T, and use 7:

$$\Box\phi + \partial_\phi V_0(\phi) + \sum_i \partial_z(m_i^2) \int \frac{d^3p}{(2\pi)^3}\frac{1}{2E_p} f_v(p_\perp, p_z, z) = 0 \ , \tag{18}$$

We have used that the equilibrium distribution functions are

$$f_v = \frac{1}{e^{p^\mu u_\mu} \pm 1} \ , \tag{19}$$

where p^μ and $u^\mu = \gamma(1,0,0,v)$ are the 4-momenta and the 4-velocity of the plasma, respectively. In 18 the sum is over all the degrees of freedom in the plasma. However, we know that there is a part of the plasma that is out of equilibrium, so we need to add the corresponding term in 18. Joining again V_0 and V_T,

$$\Box\phi + \partial_\phi V(T,\phi) + \sum_i \partial_\phi(m_i^2) \int \frac{d^3p}{(2\pi)^3}\frac{1}{2E_p} \delta f_i(p_\perp, p_z, z) = 0 \ , \tag{20}$$

Let us now write eq. 20 in the wall frame. In such a frame nothing depends on time, and ∂_z is the only relevant derivative. Multiplying in addition by $\partial_z\phi$ both sides of the equation, we get

$$-\partial_z\phi(z)\partial_z^2\phi(z) + \partial_z\phi\partial_\phi V(T,\phi) + \sum_i \partial_z(m_i^2) \int \frac{d^3p}{(2\pi)^3}\frac{1}{2E_p} \delta f_i(p_\perp, p_z, z) = 0 \ . \tag{21}$$

The last term in the right-hand side of 21, sourced by the out-of-equilibrium part of the system, is called the *friction term* $F(z)$. It is one of the factors responsible for slowing down the bubble wall to a steady state, but as we will see next, it is not the only one. If we integrate 21 in z, we get

$$\Delta V - \int dz\ \partial_T V(T,\phi)\partial_z T + \int dz F(z) = 0\ . \tag{22}$$

Recall that ΔV is the potential energy difference between the true and the false vacuum. In equation 22 we can explicitly see that two quantities can compensate for the expanding energy ΔV: the friction term $F(z)$ and another one coming from the temperature profile across the bubble wall, which means that one can have steady-state solutions even if the plasma is completely in local equilibrium. The impact of out-of-equilibrium Physics is not obvious; evaluating its impact on the computation of the bubble wall velocity has been another goal of this thesis.

The standard way of solving this scalar field equation is assuming a specific shape of the bubble wall profile, which is called the *tanh ansatz*:

$$\phi(z) = \frac{h_0}{2}\left(1 \pm \tanh\left(\frac{z}{L}\right)\right)\ . \tag{23}$$

The sign of the $\pm$ sign depends on the direction in which the wall is moving; far away in front of the bubble wall the value of the vev needs to be 0, and behind needs to be h_0. The magnitude L represents the width of the wall in its own frame. As will be explained in more detail in [2], to find the values of v_w and L the scalar field equation we impose that the total pressure on the bubble wall is zero, so the wall velocity is constant, and that the gradient of such pressure is also zero, so the width of the wall does not change.

The validity of the tanh ansatz has been evaluated in [54], which concludes that in most cases this ansatz is a very good approximation.

2.4.2 Boltzmann Equation

The out-of-equilibrium distribution functions $f_v + \delta f$ are governed by a relativistic Boltzmann equation, which is the most challenging part of the process. As we will see next, it is an integro-differential equation, including the nine-dimensional integral collision operator.

The Boltzmann equation is deduced from the idea that the change in the particle number after an infinitesimal amount of time should be determined by the rate of interactions or collisions among the particles [38]. This means that after a change like

$$\begin{aligned} x^\mu &\to x^\mu + \frac{\partial x^\mu}{\partial \tau} d\tau = x^\mu + \frac{p^\mu}{m} d\tau \\ p^\mu &\to p^\mu + \frac{\partial p^\mu}{\partial \tau} d\tau \end{aligned} \tag{24}$$

then the change in the number of particles is given by

$$\frac{f\left(p^\mu + \frac{\partial p^\mu}{\partial \tau} d\tau, x^\mu + \frac{p^\mu}{m} d\tau\right) - f(p^\mu, x^\mu)}{d\tau} = \left(\frac{p^\mu}{m}\partial_\mu + \frac{\partial p^\mu}{\partial \tau}\partial_{p^\mu}\right) f = \\ = \frac{p^\mu}{m}\left(\partial_\mu + \partial_\mu p^\nu \partial_{p^\nu}\right) f \ . \tag{25}$$

This rate should be given by a collision operator $\mathcal{C}[f]$, which for $2 \leftrightarrow 2$ processes is defined as[7]

$$\mathcal{C}[f] = \sum_i \frac{1}{4 N_p E_p} \int \frac{d^3k d^3p' d^3k'}{2E_k 2E_{p'} 2E_{k'}} |\mathcal{M}_i|^2 \delta^4(p + k - p' - k') \mathcal{P}_i \ , \tag{26}$$

where the sum is performed over all the collision processes with squared amplitude $|\mathcal{M}_i|^2$, N_p is the number of degrees of freedom of the particle with momentum p, $E_p = \sqrt{p_z^2 + p_\perp^2 + m^2}$, and P_i is the population factor, which includes the Bose enhancement and the Fermi blocking:

$$\mathcal{P}_i = f(p)f(k)(1 \pm f(p')(1 \pm f(k')) - f(p)f(k)(1 \pm f(p')(1 \pm f(k')) \ . \tag{27}$$

The subindex i means that for each collision process with amplitude $|\mathcal{M}_i|^2$ the distribution functions f will depend on the bosonic or fermionic nature of the particles involved.

In this thesis and most of the literature only $2 \leftrightarrow 2$ processes are considered in the collision operator. The main argument to do so is that among all the processes between particles in the Standard Model they are the most efficient at thermalizing the particles in the plasma, bringing them back to equilibrium. However, another reason why this practice is common is for the sake of simplicity. As we mentioned before the collision operator is the main bump in the road to solve the dynamics of the bubble wall, and it needs a deep dedicated analysis. Besides the $2 \leftrightarrow 2$, it is known that $1 \leftrightarrow 2$ processes (which would inject and extract kinetic energy from the plasma) should have an important effect on the results [55, 56], so including them in the analysis would be a relevant continuation of the work done here.

With this definition of $\mathcal{C}[f]$, the Boltzmann equation reads

$$\frac{p^\mu}{E_p}\left(\partial_\mu + \partial_\mu p^\nu \partial_{p^\nu}\right) f = -\mathcal{C}[f] \tag{28}$$

Eq. 28 is written in a Lorentz-invariant way, but we will deal with it in the wall frame, where quantities depend only on the position in the z axis, and not on time. In this frame,

$$\left(\frac{p_z}{E_p}\partial_z - \frac{\partial_z(m^2)}{2E_p}\partial_{p_z}\right) f = -\mathcal{C}[f] \ . \tag{29}$$

[7] The definition of the collision operator is not unique, and different notations can be found in the literature.

Now let us take into account that, as we said before, the distribution f has an equilibrium and an out-of-equilibrium part, $f = f_v + \delta f$. If we assume that the δf is a small perturbation around equilibrium, we can linearize the population factor in 27:

$$\mathcal{P}_i = f_v(p)f_v(k)(1 \pm f_v(p'))(1 \pm f_v(k'))\left[-\frac{\delta f(p)}{f_v'(p)} - \frac{\delta f(k)}{f_v'(k)} + \frac{\delta f(p')}{f_v'(p')} + \frac{\delta f(k')}{f_v'(k')}\right] . \quad (30)$$

Recall that in this expression the functions f_v and δf are different, depending on which of the 4 particles involved in the process they describe. The function f' is the derivative with respect to the argument of the exponential in the equilibrium distribution. To find 30 one needs to use the conservation of energy and momenta, imposed by the Dirac delta in 26. Note that if the particles are in equilibrium, i.e. $\delta f = 0$ for every particle, the collision operator vanishes; this operator is responsible for bringing the fluid back to equilibrium, so if that is already the case then $\mathcal{C}[f]$ vanishes.

We can see then that the δf, which is the quantity we want to find by solving the Boltzmann equation, appears in the kinetic term of the left-hand side of 29 (term also known as *Liouville operator*) and inside the collision operator. This is the main reason why solving the Boltzmann equation constitutes a challenge; even if one wants to implement purely numerical methods, the collision operator is an integral with nine dimensions, which cannot be computed by brute force.

In the seminal works [40,57] the authors developed a method to simplify the Boltzmann equation. They assumed a specific ansatz for the dependence on the momentum of the perturbation δf known as *fluid approximation*: f is assumed to behave like

$$f = \frac{1}{e^{\tilde{E}_p/T - X} \pm 1}; \qquad X = \mu(z) + \frac{\tilde{E}_p}{T_n}\delta\tau(z) + \frac{\tilde{p}_z}{T_n}\delta v(z) \ , \quad (31)$$

where $\tilde{E} = \gamma(E - v_w p_z)$, $\tilde{p}_z = \gamma(p_z - v_w E)$ are the energy and the momentum in the plasma reference frame. Linearizing on the perturbation X, we get

$$f = f_v - f_v' X = f_v + \delta f \implies -\frac{\delta f}{f_v'} = X \quad (32)$$

Another common assumption when using the fluid approximation or its variations is to neglect the term proportional to δ_{p_z} in the Boltzmann equation. The reason to do so is that that term is proportional to the external force $\partial_z(m^2)$; such a term is also the source of δf, which then can be expected to be of order $\mathcal{O}(m^2/T^2)$ and which we are assuming to be small. Then, the term proportional to δ_{p_z} is order $\mathcal{O}(m^4/T^4)$, even smaller [40]. The Boltzmann eq. simplifies to

$$-f_v'\frac{p_z}{E_p}\left(\partial_z\mu(z) + \frac{\tilde{E}_p}{T_n}\partial_z\delta\tau(z) + \frac{\tilde{p}_z}{T_n}\partial_z\delta v(z)\right) + \mathcal{C}[f] = -f_v'\gamma v_w\frac{\partial_z(m^2)}{2E_pT_n} \ . \quad (33)$$

Take into account that the functions $\mu(z)$, $\delta\tau(z)$ and $\delta v(z)$ factor out in the collision integral since they do not depend on the momentum variables. This is one of the most important advantages of the fluid approximation.

Using the fluid approximation for solving the Boltzmann Eq. means finding the functions $\mu(z)$, $\delta\tau(z)$ and $\delta v(z)$. To do so, the Boltzmann eq. is integrated with three different moments, namely 1, E and p_z. This means that the following operators are applied on both sides of the Boltzmann eq.:

$$\int \frac{d^3p}{(2\pi)^3} \ , \quad \int \frac{d^3p}{(2\pi)^3} E_p \ , \quad \int \frac{d^3p}{(2\pi)^3} p_z \ . \tag{34}$$

This turns the Boltzmann eq. 33 into 3 linear differential equations which depend only on z, and not on the momenta:

$$A\ \partial_z \begin{pmatrix} \mu \\ \delta\tau \\ \delta v \end{pmatrix} + \Gamma \begin{pmatrix} \mu \\ \delta\tau \\ \delta v \end{pmatrix} = S \ , \tag{35}$$

where A is a matrix with coefficients coming from the Liouville term, Γ is also a matrix which coefficients some from the collision operator, and S is a vector sourced by the external force proportional to $\partial_z(m^2)$. The coefficients in A and S can be computed analytically without much effort [58]. In [40] the coefficients of Γ were approximated analytically for a given set of processes. However, they can also be computed numerically [58].

There are some features that we implicitly assumed when writing 35. Each particle in the plasma would have corresponding functions $\mu(z)$, $\delta\tau(z)$ and $\delta v(z)$, so there should be a system like 35 for the out-of-equilibrium part of each particle. Beyond this, the out-of-equilibrium parts of different particles appear in the equations of the rest through the interactions involving them (see 30), so in principle the system of equations of the particles in the plasma should be coupled to one another. However, the situation is simplified for two reasons: first, not every particle of the plasma is considered to be out-of-equilibrium because some particles interact much more with the bubble wall than others (the more the mass, the more the interaction). For example, in [59,60] they considered that only the top (most massive particle in the SM) is driven out-of-equilibrium, while in [40, 58] they also included the W and Z bosons; the rest of the particles are in local equilibrium. In addition, even if more than one particle is driven out of equilibrium, they are not considered to interact with each other, so the systems 35 of each of them are decoupled.

Equation 35 can be solved analytically using Green's functions. Once the solution is found, we can compute the friction term $F(z)$, which is crucial for finding the bubble wall velocity.

The solution obtained by this method presents two important features, which are related. One of them is that the total out-of-equilibrium friction (the integral of $F(z)$ across the bubble wall) presents a peak at the speed of sound $v_w = c_s = 1/\sqrt{3}$ (see blue

line in Fig. 5). Second, for supersonic bubble walls (i.e. bubble walls with $v_w > c_s$) the out-of-equilibrium perturbation δf is highly suppressed in front of the bubble wall, which implies that Baryogenesis is not efficient. The interpretation given to this fact is that, as the bubble front accelerates to velocities close to c_s, its distance from the shockwave decreases. This increases the friction against the bubble wall, as the nearby shockwave also perturbs the plasma. Once v_w overcomes c_s, the traveling bubble wall finds instead an unperturbed plasma, so a sudden decay of δf in front of the bubble should be expected.

However, this method opens up several questions. To begin with, the physical interpretation is not completely satisfactory. The sound speed is c_s *in the plasma frame*; the speed of sound in front of the bubble wall, where the plasma is being pushed, is greater. There is another velocity somewhat bigger than c_s, called *Jouguet velocity*, at which the bubble wall does overcome the shockwave. Exactly at $v_w = c_s$ there should be no critical change in the behavior since the shockwave is still in front of the bubble wall, so there is no reason to expect either a peak in the friction or a suppression of the perturbation.

It is reasonable then to think that the features mentioned above are sourced by mathematical artifacts. The fluid approximation ansatz is based on a given shape of the perturbation δf; such a shape might not be describing the perturbation correctly. Already in [40] it was argued that the fluid approximation is a truncation in a momentum expansion of δf, and that higher orders might be required. Besides this, there is an obvious arbitrariness in the choice of weights with which the Boltzmann equation is integrated. In Fig. 5 we show the integrated friction, also known as pressure, as a function of the velocity of the bubble wall for different choices of the mentioned weights. We can see that the result strongly depends on such a choice, changing the value of v_w where the peak is or even removing such a peak.

These issues were pointed out in [61], where the authors argued that the friction should behave continuously, with no special behavior at $v_w = c_s$. A solution was proposed later in [58]; in this work, the author suggested that the problem lies in the velocity perturbation δv, and they argued that the fluid approximation should be modified so the ansatz on δf does not assume any specific dependence on the momentum p_z. Instead, the authors assumed a *factorization ansatz* for the integrals of the perturbation. They also changed the set of weights with which the Boltzmann equation is integrated, choosing 1, E and p_z/E instead. Using this new method, which they called *new formalism* (in contrast with the previous *old formalism*), they recomputed the perturbation δf and the corresponding friction. They found that indeed the peak at $v_w = c_s$ or *sonic boom* [62] disappears, and instead the out-of-equilibrium friction was a monotonously increasing function, with no special behavior at any velocity.

However, [58] does not completely solve the questions raised before. The assumptions on the shape of δf are indeed relaxed, but they are instead substituted by a factorization ansatz on its behavior under the integral sign. In any case, [58] does con-

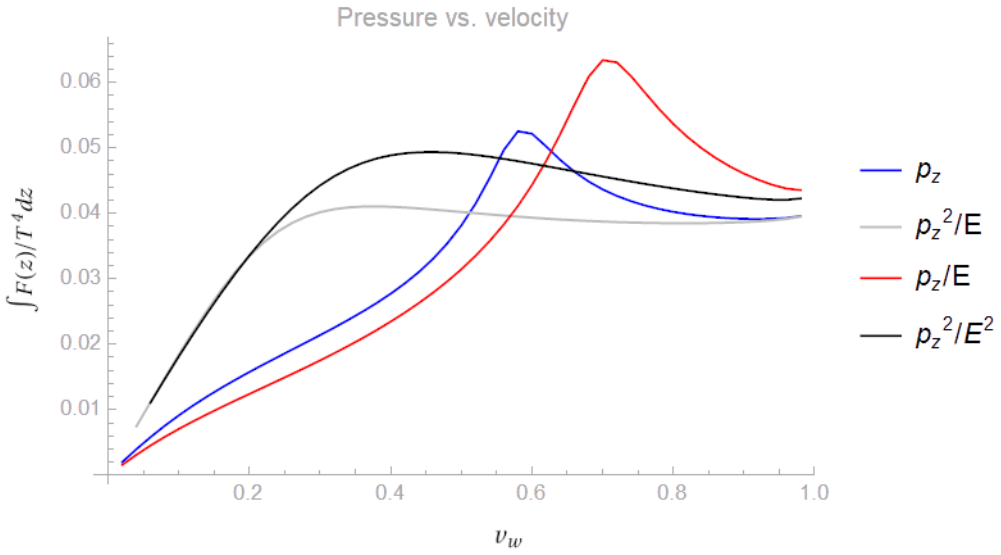

Figure 5: Integral of the friction as a function of the velocity of the bubble wall using different choices of a third weight, together with 1, E, using the method proposed in [40] (labeled as *old formalism* in [58]). In this plot, $h_0/T_n = 1.5$, $LT_n = 5$, and the top quark and the W/Z bosons are the only particles in the plasma driven out-of-equilibrium.

firm that the results significantly change when the fluid approximation is modified. We conclude then that the fluid approximation is not reliable and that using a weighted method to solve the Boltzmann Eq. suffers from some arbitrariness.

In [59] these issues were also addressed, but in a different way. In that work the authors modified the fluid approximation by extending it, adding more functions multiplying higher powers of E and p_z. They find an equation like 35, but where the matrices and vectors have higher dimension, so it can be solved exactly in the same way.

In Fig. 6 the resulting friction is shown, for different orders in the expansion of the fluid approximation. Order 1 corresponds to the old formalism explained first in this section. One can see that increasing the order of the expansion yields the appearance of new peaks in the friction. In addition, the height of these peaks decreases as the order increases; both features confirm the non-physical nature of the sonic boom in the out-of-equilibrium friction. Beyond this, the authors also proved that when the fluid approximation is extended, the out-of-equilibrium perturbation in front of the bubble wall is not suppressed anymore for supersonic walls. Fig. 6 suggests that the friction would converge to a given result if arbitrary orders are included.

The results from the works mentioned in this section strongly indicate that there is a need for an improvement of the methodology for solving the Boltzmann equation, which should relax the assumptions made on the shape of δf as well as avoid the

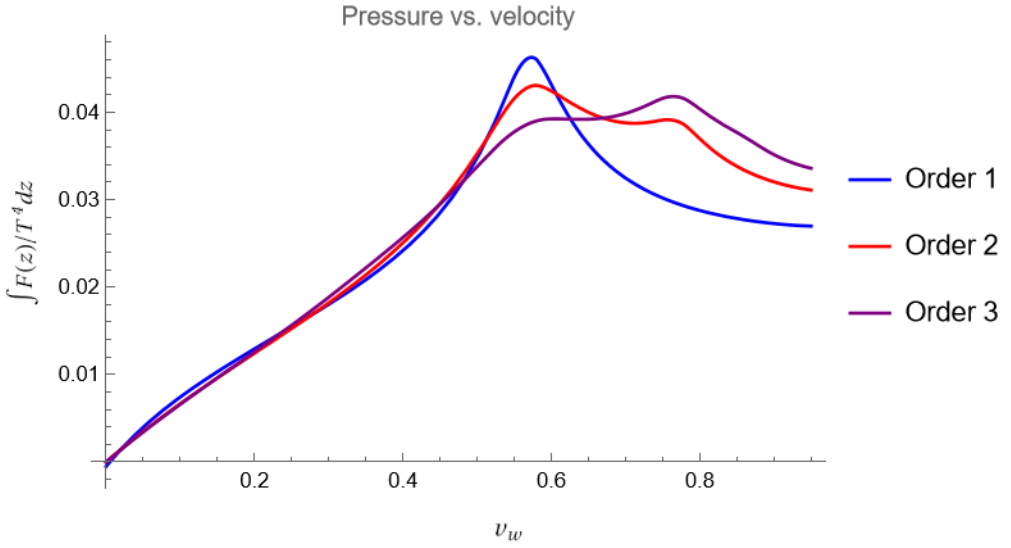

Figure 6: Integral of the friction as a function of the velocity of the bubble wall using the extended fluid approximation proposed in [59]. In this plot, $h_0/T_n = 1.5$, $LT_n = 5$, and the top quark is the only particle in the plasma driven out-of-equilibrium.

weighted method. This was the main motivation for [1], included in this thesis, where we developed a method to solve the Boltzmann equation in which the only assumption made on δf is that it is small compared to the equilibrium distribution.

2.4.3 Background fluid

The remaining ingredient is the background fluid in thermal equilibrium. It is constituted by all the degrees of freedom in the plasma, also the ones that are considered to be massless because their mass is much smaller than T_n, so they do not interact directly with the bubble wall. However, since there is a scalar field profile traveling through the plasma, the conservation of energy and momentum implies that the temperature and the velocity of such plasma cannot be constant, so the background fluid is not in global but in local equilibrium. The goal then of this section is to find such profiles for the plasma temperature and velocity.

In [40] this was achieved by assuming that the deviation from the asymptotic values are small, so $v = v_w + \delta v_{\rm bg}$ with $\delta v_{\rm bg}/v_w \ll 1$ and $T = T_n(1 + \delta\tau_{\rm bg})$ with $\delta\tau_{\rm bg} \ll 1$, in such a way that the distribution functions of the particles in the plasma can be written like

$$f_{\rm eq} = \frac{1}{e^{\tilde{E}_p/T_n - X_{\rm bg}} \pm 1}; \qquad X_{\rm bg} = \frac{\tilde{E}_p}{T_n}\delta\tau_{\rm bg}(z) + \frac{\tilde{p}_z}{T}\delta v_{\rm bg}(z) \ . \tag{36}$$

This modeling modifies the shape of the out-of-equilibrium distribution of the particles that do interact with the wall, so the fluid approximation explained in the previous

section is modified:

$$-\frac{\delta f}{f_v'} = X + X_{\rm bg} = \mu(z) + \frac{\tilde{E}_p}{T_n}(\delta\tau(z) + \delta\tau_{\rm bg}(z)) + \frac{\tilde{p}_z}{T}(\delta v(z) + \delta v_{\rm bg}(z)) \ . \tag{37}$$

Note that $\mu_{\rm bg} = 0$ since we assume the background plasma is in local equilibrium. One can then write a new matrix system analogous to 35, including now the background plasma temperature and velocity profiles, and the system can be solved similarly [40].

Including the background plasma with this formalism turns the bump in the friction at $v_w = c_s$ discussed in the previous section into a singularity, as was noted already in [40] and further discussed in [61] and [58]. However, in the previous section we saw that the special behavior of the friction at the speed of sound was an artifact of the fluid approximation and the specific choice of weights, so this divergence could also be non-physical.

This issue was solved in [62]. In that work, the authors found that the divergence of the friction is a consequence of linearizing the Boltzmann equation in terms of the temperature and velocity deviations $\delta\tau_{\rm bg}$ and $\delta v_{\rm bg}$. Including all the non-linearities in the treatment of the hydrodynamics of the plasma, they found that when $v_w \sim c_s$

$$\delta v_{\rm bg} \sim c_s + \frac{1}{1+\alpha}\left(c_s + \sqrt{\alpha^2 + \frac{2\alpha}{3}}\right) \ , \tag{38}$$

where α is the strength of the phase transition and is then related with $\delta\tau_{\rm bg}$. Linearizing in $\delta\tau_{\rm bg}$ corresponds to linearized in α, which cannot be done in 38 since the square root is a non-analytical function around $\alpha = 0$.

However, the authors of [62] pointed out that, even if the divergence is not physical, a *discontinuity* in the friction should be expected at the Jouguet velocity, since it is the velocity at which the bubble wall overcomes the shockwave, so the friction should suddenly decrease. However, to properly capture this behavior one needs to include all the non-linearities when modeling the equilibrium plasma hydrodynamics.

A suitable formalism for this goal was settled in [63] and applied to the computation of the bubble wall velocity in [60], and is also the formalism used in our work. In the rest of this section we will provide the main ideas; more details can be found in [2], added later in this document.

The starting point to find the profiles of the temperature and velocity that characterize the background plasma, which is the goal of this section, is the conservation of energy and momentum. Each of the ingredients of the system contribute to the total stress-energy tensor:

$$T^{\mu\nu} = T^{\mu\nu}_{\phi} + T^{\mu\nu}_{\rm pl} + T^{\mu\nu}_{\rm out} \ , \tag{39}$$

where the first term is the contribution from the bubble wall:

$$T^{\mu\nu}_{\phi} = \partial^{\mu}\phi\partial^{\nu}\phi - \eta^{\mu\nu}\left[\frac{1}{2}\partial_{\alpha}\phi\partial^{\alpha}\phi - V_0(\phi)\right] \ , \tag{40}$$

the second one is the contribution from the plasma in local equilibrium:

$$T^{\mu\nu}_{\rm pl} = w u^{\mu}_{\rm pl} u^{\nu}_{\rm pl} + \eta^{\mu\nu} V_T(T,\phi) \tag{41}$$

where $u^{\mu}_{\rm pl}$ is the 4-velocity of the plasma and the enthalpy is defined as $w \equiv -T\partial V(T,\phi)/\partial T = -T\partial V_T(T,\phi)/\partial T$. Finally, the third contribution to stress-energy tensor comes from the out-of-equilibrium species in the plasma

$$T^{\mu\nu}_{\rm out} = \sum_i \int \frac{d^3p}{(2\pi)^3 E_i} p^{\mu}p^{\nu}\delta f_i \ . \tag{42}$$

In the wall reference frame, all these quantities will depend only on z, and not on time. Then, conservation of $T^{\mu\nu}$ implies that the quantities T^{30} and T^{33} are conserved along the z axis. This leads to the following equations for the temperature and velocity profiles

$$\begin{cases} v_p = \dfrac{-w + \sqrt{4(T^{30} - T^{30}_{out})^2 + w^2}}{2(T^{30} - T^{30}_{out})} \ , \\ \dfrac{1}{2}(\partial_z\phi_i)^2 - V - \dfrac{1}{2}w + \dfrac{1}{2}\sqrt{4(T^{30} - T^{30}_{out})^2 + w^2} - (T^{33} - T^{33}_{out}) = 0 \ , \end{cases} \tag{43}$$

where the dependence on the temperature is implicitly encoded in V and w. Assuming that we know the out-of-equilibrium distributions (and thus their contribution to $T^{\mu\nu}$) and also the bubble wall profiles, the only thing required to determine $v_p(z)$ and $T(z)$ are the boundary conditions, which will fix the values of T^{30} and T^{33}. Such boundary conditions[8] $v_{\pm} \equiv v(\pm\infty)$, $T_{\pm} \equiv T(\pm\infty)$ are determined by the hydrodynamic regime, which in turn depends on the value of the bubble wall velocity. There are three possible regimes:

- **Deflagrations**: if the bubble wall velocity is smaller than the speed of sound, $v_w < c_s$, then the shockwave, which travels (at least) at the speed of sound is in front of the bubble wall. This means that the plasma behind the wall is at rest so in the wall frame $v_- = v_w$. Because of the presence of the shockwave $T_+ \neq T_n$; the nucleation temperature is the one of the plasma that the shockwave encounters when traveling through it, so $T^{\rm sh}_+ = T_n$. Energy-momentum conservation fixes only one possible value for T_- that yields $T^{\rm sh}_+ = T_n$.

[8] In these expressions, when we write $\pm\infty$ we mean arbitrarily in front or behind the bubble wall, but before the shockwave. This means that implicitly we are assuming there is enough distance between the bubble wall and the shockwave. This is why we cannot use our treatment exactly at the Jouguet velocity, since in that case the wall and the shockwave coincide.

- **Hybrid walls**: as we explained before, the velocity of the shockwave in front of the bubble wall is somewhat larger than c_s, since the plasma itself is being pushed by the wall. This means that a wall can travel faster than c_s and still have a shockwave in front. However, in this case the traveling bubble wall also develops a rarefaction wave behind it. This is called the hybrid regime, and the boundary conditions are found in a very similar way to the deflagration one, with the only difference being that in this case $v_- = c_s$ [63].

- **Detonations**: the hybrid regime is not possible for any velocity greater than c_s. There is a value of v_w in which no shockwave can travel faster than the bubble wall; such velocity is called the Jouguet velocity v_J. If $v_w > v_J$, the bubble enters the detonation regime: the bubble wall encounters an unperturbed plasma, so in this regime $T_+ = T_n$, $v_+ = v_w$. In this case there is also a rarefaction wave behind the bubble front.

Once the boundary conditions are known, the plasma temperature and velocity profiles can be found using 43.

During the last sections we have described each of the components of the physical system during a cosmological phase transition that are relevant for the bubble wall dynamics, which is crucial for having qualitative and quantitative control on the phenomenology of such phenomena. We have explained how each of them can be characterized, what is the Physics governing them, and how the corresponding equations might be solved.

We have discussed in special detail the Boltzmann equation. This equation needs to be solved to find the out-of-equilibrium perturbations of the plasma, which is a source of friction onto the bubble wall and so plays a pivotal role in finding the bubble wall velocity. The Boltzmann equation represents the most challenging part of the whole process, and for this reason, the equation was simplified by using the fluid approximation and the weighted method. We proved that these techniques are not reliable since the result strongly depends on the choice of weights and introduces mathematical artifacts that are not physical, indicating that the fluid approximation does not capture correctly the behaviour of the perturbations. This makes it clear that it is necessary to find a new way of solving the Boltzmann equation that relaxes the assumptions made on δf. This was the motivation for our first work [1], where we developed a numerical method that only relies on the linearization of the out-of-equilibrium perturbations. We were able to do so because we found an efficient way to compute the collision operator, which allowed us to solve the Boltzmann equation through an iterative method.

Once we had a reliable and efficient method for solving the Boltzmann equation, the next natural step was to couple it with the scalar field equation and the hydrodynamic equations to be able to find the value of the bubble wall velocity. This was done in [2] by solving the three equations using again an iterative method. This was possible thanks to an improvement in the computation of the collision integral developed in [1] which reduced the time necessary to solve the Boltzmann equation by some orders of magnitude. Both works can be found later in this document.

3 Axion-photon conversion around rotating Black Holes

Besides the cosmological Electroweak first-order phase transition, the other BSM phenomenology case studied in this thesis involves the axion. In particular, we studied the conversion of axion to photons in the superradiant cloud around a rotating Black Hole, considering the presence of an external magnetic field sourced by the accretion of matter by the Black Hole. We developed a detailed mathematical methodology to solve the axion-photon mixing in such context and we discussed the observational implications. The results of this work was published in [3], included in this thesis.

This section has the same spirit as section 2. In 3.1 we introduce the QCD axion and the basic properties that are used in this thesis, namely its mass and its coupling to photons. In 3.2 we explain how the axion-photon interaction in different astrophysical contexts has been used to constrain the axion properties, with special focus on the resonant conversion due to the presence of an external magnetic field. The mathematical methodology to solve such conversion is treated in detail. In 3.3 the superradiance mechanism is explained; such mechanism generates the axion superradiant cloud around rotating Black Holes, which is the system in which we have studied the axion-photon conversion during this thesis.

3.1 Basics of the QCD axion

The well-known Strong CP Problem is an unsolved enigma in the Standard Model of Particle Physics. From an observational point of view, this question can be phrased as: *why is the electric dipole moment of the neutron so small?* According to the Standard Model, the neutron is a bound state of one up quark and two down quarks, joined together by the gluon field. If we forget for a moment about the quantum field nature of these particles, we can compute the electric dipole moment $\vec{d}$ using the classical formula,

$$\vec{d} = \sum q_i \vec{r}_i \ , \tag{44}$$

where the sum is over the three quarks, q_i are their charge and $\vec{r}_i$ their position. Using that the radius of the neutron is around 10^{-15} m, we can give a rough estimate of the electric dipole moment: $|\vec{d}\,| \sim 10^{-16}\sqrt{1-\cos\theta}\ e$ m, where e is the electron charge and θ is the angle formed by the segments joining the up quark with each of the two down quarks [64]. This estimation can be compared with the experimental measurement, which is

$$|\vec{d}\,|_{\text{obs}} < 10^{-26}\ e \text{ cm} \ . \tag{45}$$

Such comparison yields an extraordinarily small value for the angle between the quarks: $-10^{-13} < \theta < 10^{-13}$, i.e. the quarks are arranged in a line. For some reason,

the strong interaction behaves in such a way that the quarks inside the neutron are always aligned. Why?

This fine-tuning enigma is the Strong CP Problem, and the axion solution can be already depicted using this classical simple picture: the axion solution states that there is another interaction, acting on gluons, that forces the neutron to have such an aligned internal structure.

Although the description above is enough to understand the basics of the Strong CP Problem and the axion solution, we know that quarks are not localized classical particles and 44 is not valid when studying the behavior of quarks inside a neutron. To have a more reliable picture we need to introduce the quantum field description of the strong interaction: Quantum Chromodynamics.

If we present the problem in terms of symmetries, as is common in field theories, the existence of a non-zero electric dipole moment for the neutron breaks CP symmetry. A simple way to see this is through T violation (given that CPT is a good symmetry of nature): neutron is a spin-1/2 particle, which means that it has an intrinsic magnetic dipole moment. Under T symmetry, the electric dipole moment is invariant since it is sourced just by the spatial distribution of charges inside the neutron. However, the magnetic dipole moment is related to the dynamics of such distribution of charges, which means that it changes sign under T symmetry. Then it is only possible to have neutrons with a non-zero electric dipole moment if the theory describing the interaction between the quarks can break the T symmetry or, equivalently, the CP one.

The QCD Lagrangian in the Standard Model allows for a CP-breaking term [19]:

$$\mathcal{L}_{\text{QCD},\theta} = \frac{\theta}{32\pi^2}\text{Tr}\left(\tilde{G}_{\mu\nu}G^{\mu\nu}\right) \ , \tag{46}$$

where $G_{\mu\nu}$ is the gluon field strength tensor, $\tilde{G}_{\mu\nu}$ is its dual, and the trace is taken over the $SU(3)$ index.

When constructing the lagrangian of a theory, one should consider every possible term that respects the assumed symmetries of such theory. It would be possible to assume that CP is a good symmetry of Nature, and so the term in 46. However, we know that this is not the case, since the complex phase of the CKM matrix breaks CP in weak interactions. Therefore there is no reason for not including the θ-term in the QCD lagrangian.

The angular constant θ can take any value from 0 to 2π and is the sum of two different contributions arising from uncorrelated parts of the Standard Model:

$$\theta = \bar{\theta} + \arg\left(\det(M_u M_d)\right) \tag{47}$$

where $\bar{\theta}$ is sourced by the non-trivial topological structure of the QCD vacuum and M_u, M_d are the quark mass matrices [64]. This CP-breaking term is responsible for generating a non-zero electric dipole moment for the neutron. Using again the measurement in 45, the physical parameter θ can be constrained to be $|\theta| < 10^{-10}$. This means that the two terms in 47, which come from independent sectors of the Standard Model,

cancel each other with extraordinary precision. This is why, in the language of QCD, the question *why is the electric dipole moment of the neutron so small?* translates to *why does QCD preserve CP symmetry?*

The main ingredient for the axion solution[9] to the Strong CP Problem lies in the Vaffa-Witten theorem, which guarantees that the energy contribution from the term in 46 is minimized for the CP-preserving value of θ. i.e. $\theta = 0$ [65]. Therefore if the parameter θ was able to change dynamically, the Vaffa-Witten theorem would ensure that it would relax to the CP-preserving value. This is exactly how the axion solution works: we postulate the existence of a spin-0 particle a, which we call the axion. This axion is assumed to respect a shift symmetry, which implies that in most of the couplings to the rest of the fields the axion will appear through derivatives $\partial_\mu a$, except for the topological terms like the one in 46: the coupling between the axions and the gluons will be

$$\mathcal{L} \supset \left(\frac{a}{f_a} + \theta\right) \mathrm{Tr}\left(\tilde{G}_{\mu\nu} G^{\mu\nu}\right) \ , \tag{48}$$

where f_a is an energy scale playing the role of an axion decay constant. We have also included in 48 the CP breaking term of QCD in 46. Since the Vaffa-Witten theorem guarantees that the energy contribution is minimized in CP-preserving value, the dynamics of a will drive the vacuum expectation value of the field to $\langle a \rangle = -\theta f_a$, thus solving the Strong CP Problem.

This idea was first proposed by Robert Peccei and Helen Quinn in 1977 [18]. In their solution, inspired by the Higgs mechanism, the axion arises as the Goldstone boson of a spontaneous symmetry breaking. Since then, different QCD axion models have been proposed [66, 67]. We will not discuss the details of these models, although as we shall comment on later some parameters of the axion field are sensitive to such UV completions.

We are now in a position to derive the basic properties of the axion that will be used in this thesis. Here we will briefly sketch the reasoning behind such derivation; for more details, see [19, 64, 66, 68]. The first property we shall discuss is the axion mass, which will arise from the potential term for the axion. At zero temperature, this potential will be determined by the interaction between axions and hadrons. We can obtain a good approximation of the axion potential using the lowest order of the chiral lagrangian with two quarks including the axion field.

The summary of this computation is the following: we start with the QCD lagrangian before the chiral symmetry breaking, including the quarks mass matrix M_q (which is a source of explicit breaking of the chiral symmetry) and the axion term in 48. Through a chiral transformation, this axion-gluon term can be removed from the lagrangian and added as a phase to M_q. Then, when writing the chiral lagrangian after the symmetry breaking, there will be terms coupling the pion matrix U with M_q,

[9] The axion is not the only solution for the Strong CP Problem. For a review of other possible solutions, see [64].

which includes the axion field. Expanding such terms one can find the axion potential, which should depend on the mass of the quarks and the pions. Following these steps, we get [66]:

$$V(a) = -m_\pi^2 f_\pi^2 \sqrt{1 - \frac{4 m_u m_d}{(m_u + m_d)^2} \sin^2\left(\frac{a}{2 f_a}\right)} \,, \tag{49}$$

where $f_\pi \approx 92$ MeV is the pion decay constant, $m_\pi \approx 135$ MeV is the pion mass and $m_u \approx 2$ MeV and $m_d \approx 5$ MeV are the up and down quark masses. To obtain 49 we have redefined the axion field to absorb in a the constant θ term in 48. We can confirm that the minimum of the potential in 49 happens at $a = 0$, as expected from the Vaffa-Witten theorem since $a = 0$ is the CP-preserving value of the axion field. The mass term for the axion can then be found to be:

$$m_a = \sqrt{V''(0)} = m_\pi f_\pi \frac{\sqrt{m_u m_d}}{m_u + m_d} \frac{1}{f_a} \approx 5.7 \ \mu\text{eV} \left(\frac{10^{12} \text{ GeV}}{f_a}\right) . \tag{50}$$

This relation between the axion mass m_a and its decay constant f_a is strongly connected with the axion field being coupled with topological QCD term 48 and solving so the Strong CP Problem. However, many BSM scenarios include scalar particles with a shift symmetry which are not coupled to gluons [69]. For such particles, the mass m_a and the decay constant f_a are uncorrelated (or at least not correlated in the same way as for the QCD axion) and they receive the name of *axion-like particles* (ALPs). ALPs have received a lot of attention in the past years for their rich phenomenology [19], but in this thesis we will only consider the QCD axion, although many of our results can be easily extended to the parameter space of ALPs.

The interaction between axions and pions described by the chiral lagrangian yields a non-zero anomalous coupling to photons [66]. The structure of such coupling needs to be similar to the one in 48 due to the shift symmetry governing the axion,

$$\mathcal{L} \supset \frac{g_{a\gamma}}{4} a F_{\mu\nu} \tilde{F}^{\mu\nu} \,, \tag{51}$$

and the coupling constant can be found at low energies using again the chiral lagrangian with two quarks [66]:

$$g_{a\gamma} = g^0_{a\gamma} - \frac{\alpha_{\text{EM}}}{2\pi f_a} \left(\frac{2}{3} \frac{4 m_d + m_u}{m_d + m_u}\right) \equiv \frac{\alpha_{\text{EM}}}{2\pi f_a} c_\gamma \,, \tag{52}$$

where α_{EM} is the electromagnetic fine-structure constant. Note that $g_{a\gamma}$ and m_a are related through f_a. The second term after the equal sign in 52 is the one present in the chiral lagrangian and the first one is a model-dependent coupling which depends on the UV completion of the theory, namely on the possible coupling to BSM electromagnetically charged particles. QCD axion models differ in the way the so-called Peccei-Quinn symmetry, which gives rise to the axion when broken, is implemented in the UV [19]. The coupling $g^0_{a\gamma}$ also depends on such symmetry breaking and this difference among

models has been encoded in the quantity c_γ. For example, for the KSVZ axion, where a scalar coupled to a doublet of heavy quarks is responsible for the symmetry breaking, $c_\gamma = -1.92$. For the DFSZ, where the scalar is coupled to two Higgs doublets[10], c_γ is instead not fixed [70]. To avoid model dependence, in our work we have used the conservative value $c_\gamma = 1$, although some models consider larger values of c_γ [71].

Of course, couplings with the rest of the particles in the Standard Model follow from considerations similar to those discussed above. However, as was mentioned in the introduction, in our work we have focused on the interaction between axions and photons. Such interaction leads to a variety of interesting astrophysical and cosmological phenomena which could be the key to the potential discovery of the axion.

The coupling between axion and photons modifies Maxwell's laws of Electromagnetism, mixing the dynamics of the electromagnetic and the axion fields. The new set of mixed equations of motion is called *Axion Electrodynamics* and will be discussed in the next section, together with its phenomenology.

3.2 Axion-photon mixing across the Universe

In this section we will study the mixing between axions and photons, and also how this interaction affects various astrophysical and cosmological observables through which the axion might be found, or otherwise constrained.

The effective lagrangian we will use to study such interaction is the following one:

$$\mathcal{L}_{a\gamma} = \frac{1}{2}(\partial_\mu a)^2 - \frac{1}{2}m_a^2 a^2 - \frac{1}{4}(F_{\mu\nu})^2 + j^\mu A_\mu - \frac{g_{a\gamma}}{4} a F_{\mu\nu}\tilde{F}^{\mu\nu} \ , \tag{53}$$

where j^μ is a possible four-current arising from the medium. In this thesis, we have focused on the study of the classical field dynamics of interacting axions and photons. Such dynamics are governed by the modified Maxwell's equations, which are the starting point of our work and will be discussed later.

However, before going on, let us briefly discuss how Solar Physics provides one of the most robust constraints on the axion-photon coupling[11]. The interacting term 51, present in 53, leads to the production of axions through a Primakoff effect, which can be summarized as the resonant conversion from photons to axions due to the presence of an external electric field provided by the ionized medium inside the Sun (see Fig. 7). This means that the Sun, and the stars in general, would also be a source of axion scalar radiation, using up their energy to emit such radiation. Such a process would reduce the lifetime of the stars; since the Sun is still up there in our sky, the axion-photon coupling cannot exceed a certain value. This constrains the coupling between axions and photons to fulfill $g_{a\gamma} \lesssim 23 \times 10^{-10}$ GeV^{-1} [72]. This idea can be taken one step further; for the Sun to be emitting axions while also emitting

[10] In both of these models the axion represents the complex phase of the introduced scalar fields.

[11] One of the most important experiments for axion-like particles is the *CERN Axion Solar Telescope (CAST)*, which provides similar constraints to the ones mentioned in this paragraph. However, we avoid discussing it in this thesis since it barely covers the QCD axion parameter space.

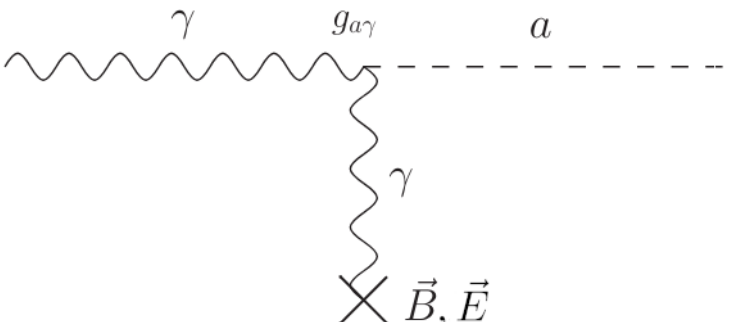

Figure 7: Scheme of the Primakoff effect: the production of photons from axions, or of axions from photons, is enhanced since one of the photons in the interaction vertex is provided by an intense external magnetic or electric field. Figure adapted from [74].

electromagnetic radiation through standard nuclear fusion, the temperature inside the star would need to be higher compared to the case where the photon-axion conversion does not take place. This higher temperature would imply higher neutrino fluxes, which would contradict the current measurements if again $g_{a\gamma}$ was too big. With this idea, the coupling can be constrained to fulfill $g_{a\gamma} \lesssim 6 \times 10^{-10}$ GeV^{-1}, which slightly improves the constraint related to the Sun lifetime discussed before [72, 73]. Since $g_{a\gamma}$ and m_a are related through the decay constant f_a, the constraints explained in this paragraph translate to a bound for the axion mass, which needs to fulfill[12] $m_a \lesssim 1$ eV.

A similar constraint for the mass of the axion can be found studying a different context: if we add the axion to the Standard Model, then the interactions within the cosmological thermal bath would produce a remnant population of axions. Since the axion is a very light particle this thermal population would be relativistic and then would be part of the so-called hot dark matter, unlike for the misalignment mechanism which produces a non-relativistic axion population. Hot dark matter is constrained to be a small part of the total dark matter, so thermal axions should not be overproduced in the Early Universe. This constrains the axion mass to fulfill $m_a \lesssim 0.2$ eV, or equivalently $g_{a\gamma} \lesssim 4 \times 10^{-11}$ GeV^{-1} [72, 75]. In addition, this thermal production of axions in the Early Universe would have an impact on the evolution of the effective number of relativistic degrees of freedom, opening up the possibility of detecting the axion by observing the CMB [76].

Beyond the QCD axion, Solar Physics has proven to be very useful in constraining also axion-like particles in general. For instance, if ALPs with masses in the range keV-MeV existed, they would be produced in the interior of the Sun, but due to their high mass they would behave non-relativistically and would then be trapped by the gravitational potential of the Sun, accumulating over cosmic times. These ALPs would then decay into photons, leaving an imprint on the X-ray emission by the Sun [77].

[12]The exact value of this axion mass constraint depends on the specific QCD axion model, as explained below equation 52.

One of the most important advantages of the constraints explained in the previous paragraph is that no initial amount of axions is required as an initial condition; the axions are produced through the interaction with photons in the lagrangian in 53. However, assuming an initial amount of axions can be very useful, and is especially convenient for constraining axion dark matter. As mentioned in the introduction, the axion (and ALPs in general) is a well-motivated candidate for dark matter since, thanks to the misalignment mechanism, it is possible to produce a non-relativistic population of axions in the Early Universe. The interaction between axion dark matter and light has been studied to a great extent in the literature; we shall discuss it later since it has been one of the main inspirations for our work.

Axion Electrodynamics

However, for that purpose we need first to understand how the axion-photon coupling modifies Maxwell's equations. From the Lagrangian in 53, the new Maxwell's equations are:

$$\begin{cases} -\partial_t^2 a + \nabla^2 a = m_a^2 a - g_{a\gamma} \vec{B} \cdot \vec{E} \\ \vec{\nabla} \cdot \vec{B} = 0 \\ \partial_t \vec{B} + \vec{\nabla} \times \vec{E} = 0 \\ \vec{\nabla} \cdot \vec{E} + g_{a\gamma} \vec{B} \cdot \vec{\nabla} a = \rho \\ \vec{\nabla} \times \vec{B} - \partial_t \vec{E} = \vec{j} + g_{a\gamma} (\vec{B} \partial_t a - \vec{E} \times \vec{\nabla} a) \end{cases} \tag{54}$$

The equations are written in terms of the electric vector field $\vec{E}$, the magnetic vector field $\vec{B}$, the charge density $\rho = j^0$ and the current density $\vec{j}$. Note that the first equation in 54 is the modified Klein-Gordon equation for the axion.

The modified Maxwell's equations have a direct impact on the polarization of traveling electromagnetic waves. From 54 it can be proved that the combination $\vec{E} + (g_{a\gamma} a/2)\vec{B}$, $\vec{B} - (g_{a\gamma} a/2)\vec{E}$ satisfy free wave equations at linear order in the coupling $g_{a\gamma}$ [78]. This means that if an electromagnetic wave is traveling through a non-constant axion profile then its polarization axes would be rotated by an angle $\beta = g_{a\gamma}(a_f - a_0)/2$, where a_0 and a_f are the values of the axion field at the final and initial spacetime position of the light wave, respectively. This idea has been used to explain, using ALPs, the birefringence angle measured in the CMB [79–81], for instance.

However, we can take a different perspective. As we mentioned before, the interaction of axions and photons can be enhanced in the presence of an external magnetic field, the so-called Primakoff effect (see Fig. 7). We know that the Universe is filled with magnetic fields, like the ones present in the interstellar and intergalactic medium [82] or the one sourced by highly magnetized neutron stars or *magnetars* [83]. If, for instance, an axion condensate like a dark matter clump encountered such an intense external magnetic field, a significant amount of axions could be converted into photons through the Primakoff effect.

In the seminal work [84] the authors developed a formalism to deal with such a situation. Let us begin with the simplest case: considering an external constant magnetic field $\vec{B}_0$ that dominates over the magnetic field of the traveling electromagnetic wave and a vacuum medium with $\rho = j = 0$, one can find from 54 the wave equation for the axion and the photon in the Lorenz Gauge:

$$\begin{cases} (\partial_t^2 - \nabla^2)A^i = -g_{a\gamma}B_0^i \partial_t a \\ (\partial_t^2 - \nabla^2 + m_a^2)a = g_{a\gamma}\vec{B}_0 \cdot \partial_t \vec{A} \ , \end{cases} \tag{55}$$

where A^i and B_0^i are the components of the electromagnetic vector potential and the external magnetic field respectively. From 55 we can see than only the component of $\vec{A}$ parallel to $\vec{B}_0$ interacts with the axion; the rest of the components remain decoupled. Let us now consider plane waves for a and A, propagating along the y axis so only spatial derivatives with respect to y are different from 0, and $\vec{B}_0$ to lie entirely in the z axis, $\vec{B}_0 = B_0\vec{e}_z$. With these assumptions the system 55 simplifies to

$$\begin{cases} (\partial_t^2 - \partial_y^2)A_x = 0 \\ (\partial_t^2 - \partial_y^2)A_z = -g_{a\gamma}B_0 \partial_t a \\ (\partial_t^2 - \partial_y^2 + m_a^2)a = g_{a\gamma}B_0 \partial_t A_z \ , \end{cases} \tag{56}$$

This system was studied in [85], where it was solved exactly: for an initial state formed only by an axion wave travelling to the right[13], such that at $A_x(t, y) = 0$, $A_z(t = 0, y = 0) = 0$ and $a(t = 0, y = 0) = a_0$, one can find that

$$\frac{|\vec{A}(t, y)|^2}{|a_0|^2} = \frac{4\omega^2 g_{a\gamma}^2 B_0^2}{m_a^4 + 4\omega^2 g_{a\gamma}^2 B_0^2} \sin^2\left(\frac{y}{2}(k_+ - k_-)\right) \tag{57}$$

where ω is the energy of the incoming axion wave, and

$$k_\pm = \sqrt{\omega^2 - \frac{1}{2}\left(m_a^2 \pm \sqrt{m_a^4 + 4\omega^2 g_{a\gamma}^2 B_0^2}\right)} \ . \tag{58}$$

The quantity in eq. 57 is called the *conversion probability* $p_{a\to\gamma}$, a concept ubiquitous in the literature. $p_{a\to\gamma} = |\vec{A}|^2/|a_0|^2$ is interpreted as the probability of one axion from the initial state converting into a photon at some point in spacetime. Similarly, $p_{a\to a} = |a|^2/|a_0|^2$ is called the *survival probability*.

The concept of the conversion probability is very useful since important observables, like the radiated power by a source, depend on $|\vec{A}|^2$. If we assume, or have some information about some initial abundance of axions, then $|\vec{A}|^2 = p_{a\to\gamma}|a_0|^2$. However, the concept of the conversion probability can be confusing and can yield some misunderstanding when the total number of particles is not conserved, as we shall discuss later on.

[13] In [85] the authors considered an incoming photon wave, but the solution for the case we are discussing is completely analogous.

Resonant axion-photon conversion

Let us now consider a more complex situation. We know that the intergalactic and interstellar media host ionized gas or plasma [86, 87]; the traveling electromagnetic waves interact with such a plasma, and this interaction can be modeled as an effective mass for the photon ω_p, which will depend on the environment properties. In this way, eqs. 56 become [88]

$$\begin{cases} (\partial_t^2 - \partial_y^2 + \omega_p^2) A_z = -g_{a\gamma} B_0 \partial_t a \\ (\partial_t^2 - \partial_y^2 + m_a^2) a = g_{a\gamma} B_0 \partial_t A_z \ , \end{cases} \tag{59}$$

where we have considered again the situation of plane waves traveling in the y direction in the presence of an external magnetic field B_0 located along the z axis. We ignore the equation for A_x since it is decoupled from the system, as discussed before. If the plasma mass ω_p is constant, this system can be again solved analytically; for the same situation considered above (initial state consisting in an axion wave of frequency ω and amplitude a_0 travelling to the right), eqs. 57 and 58 become [89]

$$\frac{|\vec{A}(t,y)|^2}{|a_0|^2} = \frac{4\omega^2 g_{a\gamma}^2 B_0^2}{(m_a^2 - \omega_p^2)^2 + 4\omega^2 g_{a\gamma}^2 B_0^2} \sin^2\left(\frac{y}{2}(k_+ - k_-)\right) \tag{60}$$

where ω is the energy of the incoming axion wave, and

$$k_\pm = \sqrt{\omega^2 - \frac{1}{2}\left(m_a^2 + \omega_p^2 \pm \sqrt{(\omega_p^2 - m_a^2)^2 + 4\omega^2 g_{a\gamma}^2 B_0^2}\right)} \ . \tag{61}$$

The most relevant consequence of this result is that if $m_a \approx \omega_p$ then the conversion probability can be as high as 1, i.e. at some points in space the whole amount of axions are converted into photons. This situation is called *resonant axion-photon conversion* and it has been one of the main ideas in the past years to overcome the smallness of the coupling $g_{a\gamma}$ in order to find relevant observational consequences of the existence of the axion and its coupling to light.

However, the presence of this resonance for constant plasma mass requires a remarkable tuning of the parameters. For this resonance to have an effect, so that the conversion probability approaches 1, we need ω_p to be close enough to m_a such that $(m_a^2 - \omega_p^2)^2 \ll 4\omega^2 g_{a\gamma}^2 B^2 \iff m_a^2 - 2\omega g_{a\gamma} B_0 \ll \omega_p^2 \ll m_a^2 + 2\omega g_{a\gamma} B_0$. If we are working with non-relativistic axions, which is justified if we are considering axions to be part of the cold dark matter in our Universe, then $\omega \sim m_a$. Additionaly, the typical values of the interstellar magnetic field is of order μG [86]. Using also the relation between $g_{a\gamma}$ and m_a through eqs. 50 and 52 (with $c_\gamma \sim 1$), then in order to have a resonant conversion the photon plasma mass ω_p needs to fulfill

$$m_a^2(1 - 10^{-26}) \lesssim \omega_p^2 \lesssim m_a^2(1 + 10^{-26}) \ . \tag{62}$$

We conclude that the plasma mass needs to be extremely fine-tuned for the resonance to take place.

However, the resonance idea can still be useful if we consider non-constant plasma densities. If the photon mass ω_p changes over some region of space (or time) then it would be covering a range of axion masses, so the fine-tuning problem is alleviated.

A very natural and well-motivated case for considering axion-photon conversion in such a situation is a neutron star. First, because they have very strong magnetic fields, of order around 10^{14} G, with which the axion-photon would be considerably enhanced, and second because the magnetic field profile around the neutron star induces a non-constant plasma density, which yields a non-constant plasma mass. This system has been of deep interest in the community [22–28], and in the next paragraphs we shall discuss their methodology to find the axion-photon conversion[14].

An important drawback of including non-constant plasma mass profiles is that the system of equations 59 cannot be solved exactly anymore. Instead, the main method to solve such system is using the WKB approximation, commonly used in Quantum Mechanics; the solution of for the photon is assumed to be of the form (we drop the z subindex for A_z from here on) $A(y,t) = A_0(y)e^{i(\chi(y)-\omega t)}$ such that $|\partial_y^2 A_0| \ll |A_0(\partial_y\chi)^2|$ (the amplitudes changes much slower than the oscillating phase), and similarly for the axion. Plugging this into 59, we can find an approximate solution of the system[15], which fulfills [25]:

$$\frac{|A(y,t)|^2}{|a_0|^2} = \frac{\omega^2 g_{a\gamma}^2}{4|k_\gamma(y)|}\left|\int_0^y \frac{B(y')}{\sqrt{|k_\gamma(y')|}} e^{ik_a y' - \int_{y'}|k_\gamma(y'')|dy''}\, dy'\right|^2 , \tag{63}$$

where $k_a = \sqrt{\omega^2 - m_a^2}$, $k_\gamma = \sqrt{\omega^2 - \omega_p(y)^2}$ and $B(y)$ accounts for the magnetic field profile around the neutron star. Here the resonance effect we discussed for the constant ω_p case appears through the *stationary phase approximation*; the integral in 63 is dominated by the region around the point where the oscillating phase is constant[16], i.e. when $k_a = k_\gamma \iff m_a = \omega_p$. Using the aforementioned stationary phase approximation, being y_0 the conversion point ($k_\gamma(y_0) = k_a$), 63 reduces to [25]

$$\frac{|A(y,t)|^2}{|a_0|^2} = \frac{\left(B(y_0)\omega g_{a\gamma} L\right)^2}{2k_a|k_\gamma(y)|} . \tag{64}$$

The quantity L is defined as $L \equiv \sqrt{\pi/|k_\gamma'(y_0)|}$ and can be understood as the width of the conversion region [24]. The result in 64 or similar versions are commonly used in the literature.

However, this methodology opens up several questions. One of the doubts that could be raised is if the WKB approximation is valid along all the region where the

[14] In such papers, the angle between the traveling direction and the magnetic field is not fixed to be $\pi/2$, as we have done in our discussion, but is left as a free parameter. However, we will keep it fixed to $\pi/2$ for the sake of simplicity.

[15] Assuming, again, a initial state formed only by axions with an amplitude a_0 and frequency ω

[16] This point will always be included in the integral domain since we are interested in the solution of the system far away from the source, where the plasma density decays.

system of equations 59 is being solved. We can split the space in two regions: In the first, closer to the star, $k_\gamma^2 < 0$; in the other, further away, $k_\gamma^2 > 0$. In the first region the conversion of axions to photons is expected to be exponentially suppressed since $\omega_p > \omega$ there. In the other region, we expect the solution to rapidly oscillate around some non-zero value, related with the quantity in 64. This requires that around the point where $k_\gamma = 0$ the WKB approximation breaks down; there is some region around such point where the amplitude of the photon field rapidly changes. This can be even more problematic if such region includes the resonant point where $k_a = k_\gamma$, since then most of the conversion from axions to photons would happen in a region where the WKB approximation could break down, which is likely to happen if $k_a \approx 0$. This is the case for cold axion dark matter, but also for the axions in the superradiant cloud which is the physical case we have considered in our thesis as we will describe in section 3.3.

There is another question that can be raised, this time related with the physical interpretation of the probability. If the parameters in 59 are constant and we consider waves traveling only in one direction, the total number of particles is conserved and the quantity $|A|^2 + |a|^2$ is constant along the traveling direction. Since the initial state is formed only by axions, then the quantities $|A|^2/|a_0|^2$, $|a|^2/|a_0|^2$ can be interpreted as probabilities as we discussed before, $p_{a\to\gamma}$ and $p_{a\to a}$ respectively, such that $p_{a\to\gamma} + p_{a\to a} = 1$. However, if some parameter in 59, like ω_p, is not constant, then $\partial_y(|A|^2 + |a|^2) \neq 0$. This issue has yielded some discussion in the literature about the interpretation of the conversion probability, and several modifications of the definition of $p_{a\to\gamma}$ can be found in different works [22, 25, 28, 90].

Relativistic approximation

A practice that is commonly found in the literature is the simplification of the system 59 assuming relativistic behaviour[17] of the axions and photon fields [22, 24, 91]. This could solve the first problem we mentioned above. To do so, $\partial_t^2 - \partial_y^2$ is rewritten as $(\partial_t + \partial_y)(\partial_t - \partial_y)$. Naively, we can assume that $\partial_t \sim \omega$, and $\partial_y \sim k$, where ω and k are the frequency (energy) and the wavenumber (momentum) of the traveling waves (particles). Therefore the operator $\partial_t^2 - \partial_y^2$ can be simplified to $2\omega(\omega - i\partial_y)$ [88]. Using this, 59 can be simplified:

$$\left[(\omega - i\partial_y)\mathbb{1} - \frac{1}{2\omega}\begin{pmatrix}\omega_p^2 & -g_{a\gamma}B_0\omega \\ -g_{a\gamma}B_0\omega & m_a^2\end{pmatrix}\right]\begin{pmatrix}A \\ a\end{pmatrix} = \begin{pmatrix}0 \\ 0\end{pmatrix} \ , \tag{65}$$

where we assumed that $A(t,y) = \tilde{A}(y)e^{i\omega t}$, $a(t,y) = \tilde{a}(y)e^{i\omega t}$ for some $\tilde{A}(y)$, $\tilde{a}(y)$. The system 65 can be solved also using a WKB approximation:

$$\frac{|A(y,t)|^2}{|a_0|^2} = \frac{g_{a\gamma}^2}{4}\left|\int_0^y B(y')e^{\frac{-i}{2\omega}(m_a^2 y' - \int_{y'}\omega_p^2(y'')dy'')}\,dy'\right|^2 \ . \tag{66}$$

[17] A more involved version of the procedure described here was done in [24] to account for non-relativistic behaviour.

The stationary phase approximation can be used again to further simplify this expression:

$$\frac{|A(y,t)|^2}{|a_0|^2} = \frac{(B(y_0)g_{a\gamma})^2}{2}\frac{\omega}{m_a}\frac{\pi}{|\omega_p'(y_0)|} = \frac{(B(y_0)g_{a\gamma}L)^2}{2}\frac{\omega}{k_a} \ . \tag{67}$$

Recall that $L \equiv \sqrt{\pi/|k_\gamma'(y_0)|}$, where y_0 is the conversion point: $\omega_p(y_0) = m_a$. The expressions in 64 and 67 differ in a factor $\omega/|k_\omega(y)|$, which is consistent with the assumption of relativistic behaviour, i.e. $k_\gamma \sim \omega$.

The Schrödinger-like system of equations in 65 does conserve the quantity $|A|^2 + |a|^2$ even if the quantities in the mixing matrix on the left-hand side of 65 are not constant. This is because 65 is a system of first-order differential equations and the aforementioned mixing matrix is symmetric. Therefore, in principle, the probability interpretation can be recovered in such case. However, the conservation of $|A|^2 + |a|^2$ is indeed an artifact of the reduction of the original system, which is second-order, to a first-order one; 66 and 67 lack the term $1/|k_\gamma(y)|$ in 63 and 64, which breaks the conservation of $|A|^2 + |a|^2$. This is why such modulating term is sometimes introduced by hand in the literature [22].

The study of these questions led us to take a different perspective. One of the goals of this thesis was to develop a methodology to solve the axion-photon conversion avoiding the problematics explained above, having more qualitative and quantitative control of the assumptions and on the region of the parameter space where such assumptions are valid.

The goal was not only to solve the system with a new perspective, but also to apply it to a different physical system: the *superradiant axion cloud*. The superradiance mechanism allows a light scalar field, like the axion, to amplify itself through the extraction of angular momentum of a Black Hole , i.e. the axion field is able to convert angular momentum into axion particle number. The basics about superradiance will be depicted in the following section.

3.3 Axion superradiance

In 1971 Penrose and Floyd described a mechanism through which a particle could increase its total energy at the expense of angular momentum of a rotating Black Hole: the *Penrose process* [92]. Such effect is possible thanks to the existence of the ergosphere, a region outside the event horizon where every lightlike world line is rotating according to an observer at infinity. To summarize, particles inside the ergoregion might have negative energy according to an observer at infinity. Then, it is possible for a particle to split in two inside the ergoregion. One of the particles would have negative energy and would fall into the Black Hole, which would lose rotational energy. The other one has more energy than the original one and can escape, gaining the energy lost by the Black Hole.

A natural question one could ask now is if a field, instead of a particle, can also take advantage of such a process. A natural way to answer such question for the axion (and, in general, for any scalar field) is to study the Klein-Gordon equation around a rotating Black Hole [93]:

$$(\Box + m_a^2)a(t,\vec{r}) = \left(\frac{1}{\sqrt{-g}}\partial_\mu(\sqrt{-g}g^{\mu\nu}\partial_\nu) + m_a^2\right)a(t,\vec{r}) = 0\ . \tag{68}$$

In 68, $g^{\mu\nu}$ is the Kerr metric describing the curved spacetime around a Black Hole. For small $\alpha \equiv GM_{\rm BH}m_a$, where G is the gravitational constant and $M_{\rm BH}$ is the Black Hole mass, equation 68 can be perturbatively solved by decomposing $a(t,\vec{r})$ in spherical harmonics Y_{lm},

$$a(t,\vec{r}) = \sum_{nlm} e^{-i\omega_{nlm}t}R_{nl}(r)Y_{lm}(\theta,\phi) \tag{69}$$

where θ and ϕ represent the polar and azimuthal angle respectively, and $n,\ l,\ m$ are the usual labels for the energy and angular momentum levels. The solution for the radial functions $R_{nl}(r)$ happen to be very similar to the analogous functions in the solutions of the Schrödinger equation for an hydrogen atom [93]. The main difference is that in the rotating Black Hole case we are dealing with $\omega_{nlm} = \omega_{nlm,R} + i\omega_{nlm,I}$, i.e. the frequencies have a non-zero imaginary part. Such imaginary part fulfills

$$\omega_{nlm,I} \propto \tilde{a}m - 2\alpha(1+\sqrt{1-\tilde{a}^2})\ , \tag{70}$$

where $0 \leq \tilde{a} \leq 1$ is the adimensional Black Hole spin parameter, $\tilde{a} = J/(GM_{\rm BH}^2)$, and J is the angular momentum of the Black Hole. This means that all the modes $n,\ l,\ m$ that fulfill

$$\alpha \lesssim \frac{\tilde{a}m}{2} \tag{71}$$

are proportional to $e^{\omega_{nlm,I}t}$, which means that they are exponentially amplified.

Equation 71 is known as the *superradiant condition*, and it is the answer to the question we raised at the beginning of this section: given a rotating Black Hole, a small perturbation of a field which mass is small enough is able to steal the rotational energy of the Black Hole to amplify itself, forming a condensate state around the Black Hole called the *superradiant cloud*. It is possible to give a clear interpretation to the superradiant condition; if we take $\tilde{a}m$ to be order 1, we can rewrite 71 as $m_a^{-1} \gtrsim 2GM_{\rm BH}$. Then, a scalar field can build a superradiant cloud around a rotating Black Hole if its Compton wavelength is bigger than the Schwarzschild radius of the Back Hole.

Note that it is crucial that the field is massive. The Penrose process can also take place for massless fields like the electromagnetic radiation. However, in such a case the stolen energy escapes the Black Hole. The presence of the mass acts as mirror, bounding the stolen energy to the Black Hole and thus building the superradiant instability.

This mechanism has been used to constrain the mass of the axions [94, 95]. If we observe some Black Hole with a certain angular momentum, we know there is a certain range of masses forbidden for the axions; the axions with such masses would be able to steal part of the rotational energy we are measuring in a timescale smaller than the age of the Universe. The mentioned forbidden region is 10^{-21} eV $< m_a < 10^{-17}$ eV and 10^{-13} eV $< m_a < 10^{-11}$ eV. This constraint is specially relevant since it is reasonably model-independent.

As we have mentioned before, in this thesis we have studied the axion-photon conversion in the superradiant cloud. This idea presents several advantages with respect to the neutron star case. First, unlike in the studies involving neutron stars and other astrophysical environments, it is not needed to assume an initial state of axions, which is normally linked with the assumption of the axion being part of the dark matter in our Universe; in our case, the axion initial state is dynamically generated by the superradiance mechanism, so we just need to assume its existence. Second, Black Holes accrete ionized matter from the interstellar medium around them, which will provide the required non-constant plasma profile mentioned in the previous section. This accreting matter generates a magnetic field around Black Holes that will trigger the conversion. This magnetic field will be many orders of magnitude smaller than the neutron star one, but this can be compensated with the huge number of axions populating the cloud; we will roll the dice many more times.

The results of this thesis regarding the axion-photon conversion, including the developement of the new mathematical approach to solve the axion-photon mixing and the observational consequences when considering Black Holes were published in [3], included in this document.

4 Results and discussion

In this section we summarize the work done in [1–3], which are included in the next part of this thesis.

4.1 Paper 1: Bubble wall dynamics at the electroweak phase transition

The main goal of this work was to develop a new method to solve the Boltzmann equation in the context of an Electroweak phase transition avoiding the use of the fluid approximation, which as argued before does not capture properly the behaviour of the out-of-equilibrium perturbation.

To do so we rewrite the Liouville kinematic operator of the Boltzmann equation as a derivative along flow paths, which are defined as the trajectories of free particles in the (z, p_z) plane in the presence of a bubble wall, which modifies the value of the mass of the particles. Doing so we do not neglect the term proportional to $\partial_{p_z}\delta f$, which is normally neglected when using the fluid approximation and the weighted method.

The main obstacle when solving the Boltzmann equation is the collision operator, which is a nine-dimensional integral that depends on the out-of-equilibrium perturbation. We used a new treatment that simplifies the computation of this operator by identifying the part of the integral that is independent of the perturbation and therefore only needs to be computed once. We called these functions *kernels*, which depend only on the choice of collisions in the plasma. In this work and the following one we only consider $2 \leftrightarrow 2$ processes.

Using these techniques, we are then able for the first time to find the full solution of the linearized Boltzmann equation by an iterative method, which is feasible because of the efficient method for computing the collision integral. By choosing an educated initial step for the iteration, convergence is achieved within a few steps.

We compare our results with the ones obtained using the previous ones relying on the fluid approximation and its modifications, and we find quantitative and qualitative differences. For this comparison, we assumed that the top quark is the only species interacting directly with the bubble wall, and we neglected the presence of the background plasma in local equilibrium.

We observe that the extension of the fluid approximation approaches our results when increasing the order of the expansion of the fluid approximation proposed in [59]. We find bigger differences with the new formalism proposed in [58], although we agree on the disappearance of any special behavior of the solution when the bubble wall velocity is at the speed of sound if the background plasma is not considered.

4.2 Paper 2: Collision Integrals for Cosmological Phase Transitions

As a natural extension of the previous one, in this work we couple the Boltzmann equation with the scalar field equation (describing the expansion of the bubble wall) and the energy-momentum conservation equations (governing the hydrodynamics of the background plasma) to find the value of the bubble wall velocity.

We also improved the methodology developed in the previous work to deal with the collision operator by identifying such collision terms depending on the out-of-equilibrium perturbation as the action of a hermitian operator. Using the spectral theorem such an operator can be decomposed into its eigenvalues and eigenvectors, which makes its evaluation even more efficient.

This improvement speeds up our method for solving the Boltzmann equation. Therefore we can solve the coupled system of the three equations with an iterative method. Given a BSM model predicting a FOEWPhT we can find the bubble wall velocity including the out-of-equilibrium perturbations in the plasma.

We applied this method to find the bubble wall velocity using the scalar singlet extension of the SM as a benchmark model, for two different values of the model parameters. Like in [1], we considered the top quark to be the only particle interacting directly with the bubble wall. We compared the results with the case in which the

out-of-equilibrium perturbations are ignored. At both benchmark points of the model, we found that out-of-equilibrium Physics has an important quantitative impact on the bubble wall velocity, reducing its value by up to 30%. Among all the parameters, the most sensitive one to the inclusion of the out-of-equilibrium friction is the bubble wall velocity, which is precisely the most relevant one for the phenomenology of the transition.

We also could confirm that there is a discontinuity in the friction against the bubble wall at the Jouguet velocity when the background plasma is taken into account. This corresponds to the velocity where the bubble wall and the shockwave in front of it are arbitrarily close. However, our results cannot be completely trusted close to this velocity, since a more delicate treatment of the hydrodynamics is required.

4.3 Paper 3: Lighten up Primordial Black Holes in the Galaxy with the QCD axion: Signals at the LOFAR Telescope

In this work we compute the luminosity resulting from the conversion to photons of the axions hosted by a superradiant instability around a Black Hole. We take into account the accretion of non-relativistic ionized matter into the Black Hole using the Bondi model of accretion, which is spherically symmetric. Such accretion provides the effective photon plasma mass, necessary to have a resonant conversion from axions to photons.

To find the luminosity we use the method of variation of parameters, highlighting the breaking of the WKB approximation around the conversion point, where the axion mass and the photon plasma mass are equal. We neglect the backreaction of the luminosity on the axion cloud, which acts as an external source. In addition to the developed method we provide the specific region of the parameter space where its assumptions hold. We find similar expressions for the luminosity as those found in previous literature.

Using this result we conclude that to have relevant luminosities the conversion point needs to be close to regions of the cloud with high density of axions. This, together with the constraints imposed by the superradiance process, requires the Black Hole to have subsolar masses, which led us to consider a population of Primordial Black Holes as part of dark matter, consistent with current bounds.

The corresponding range of axion masses lies in the radio band, so we make an analysis of the detectability of the emitted signal using LOFAR, the telescope already in operation with the highest sensitivity for frequencies just above the ionosphere screening bound of 10 MHz. We find that for a region of the parameter space, corresponding to PBH and axion with masses in the range $10^{-5} - 10^{-4}\, M_\odot$ and $4 \times 10^{-8} - 4 \times 10^{-7}$ eV, respectively, the radiation emitted through axion-photon conversion by the closest PBH can be measured by the LOFAR telescope. This range of PBH masses coincidently matches the one that would explain the ultra-short-timescale microlensing events measured by the OGLE experiment.

In addition, we find that, even if the luminosity of the system is high enough to be detected with radio telescopes, the axion-photon conversion is not efficient enough to spoil the building of the superradiant cloud, or to use up the energy in the cloud so fast that it would be hardly detectable. These comparisons justify our neglect of the backreaction on the cloud. We also determine a conservative constraint to ensure that the magnetic field of the produced electromagnetic wave is not higher than the external one, which would lead to a snowball effect and would also break the assumptions of our analysis.

5 Conclusions

We finish the first part of this thesis by commenting on the main conclusions of the research carried out and some possible lines of future research.

One of the topics studied in this thesis is the dynamics of the bubble wall during a FOEWPhT, with the specific goal of finding the bubble wall velocity. Constant velocities are achieved thanks to the action of a friction force against the bubble wall. This friction is partially sourced by the out-of-equilibrium plasma and it represents the most challenging obstacle in studying the dynamics of the wall. Then, one goal of this project was to evaluate the impact of such out-of-equilibrium physics on the results.

First, we took a step forward in the methodology for finding the out-of-equilibrium perturbations by solving, for the first time, the full solution of the linearized Boltzmann equation. We proved that previous approaches were based on unrealistic assumptions and that a more general method, such as ours, was needed.

We used these results to solve the Boltzmann equation to find the bubble wall velocity, adding to the analysis the scalar field equation describing the bubble wall and the plasma hydrodynamics. We developed in this way a method to find the bubble wall velocity for any given model. We checked that indeed out-of-equilibrium effects have an important quantitative impact on the computation of the bubble wall velocity, so it is necessary to include them to have reliable predictions. We also confirmed that there is a discontinuity in the friction at the Jouguet velocity if and only if the background plasma is included in the system.

The work done in [17], by the same authors of [1, 2] and not included in this thesis, is a continuation of the research explained here. In that work we improved the method to solve the Boltzmann equation in two ways. First, we added all the non-linear terms involving the perturbation, which in our formalism can be done in a very natural way. Second, we exploited the fact that the hermitian operator representing the collision operator introduced in [2] is rotationally invariant, which means that it block-diagonalizes in a spherical harmonics basis and so further improves the efficiency of the method.

We recomputed the value of the bubble wall velocity with these modifications and also included in the analysis the W/Z bosons as out-of-equilibrium species in addition to the top quark, for the same benchmark points as in [2]. In both cases the impact on

the wall velocity of the non-linear terms in the out-of-equilibrium perturbations was negligible, suggesting that the linearized Boltzmann equation is a good approximation. On the other hand, adding the out-of-equilibrium W/Z bosons reduces the bubble speed by $\sim 10-30\%$. The most important contribution to the friction by these bosons comes from the soft modes. This constitutes the most important source of theoretical uncertainty in our results, since collective phenomena in the plasma (which are not captured by the Boltzmann equation) dominate the behaviour of soft bosons.

Improving the description of the boson soft modes in our method is an interesting future prospect of our work, as our results suggest that they could have an important impact on the value of the bubble wall velocity. Besides this, a very natural continuation of our analysis is to scan regions of the parameter space of different BSM models, instead of doing it for specific benchmark points. This would allow us to find which of these regions could be probed by future gravitational wave interferometers, or which regions could explain the amount of matter-antimatter observed in our Universe.

The goal of the second part of this thesis was to compute the electromagnetic signal from a QCD axion superradiant cloud around a rotating Black Hole through the axion-photon resonant conversion. This resonant conversion was possible thanks to the accretion of ionized plasma towards the Black Hole, which produces an external magnetic field and a profile for the effective mass of the photon.

To find the luminosity of this system, we built a new method that avoids some of the problems associated with the formalism used to study similar systems, such as the transformation of axion-dark matter clouds around neutron stars. Our formalism gives an analytical expression of the luminosity, and provides information about the region of parameter space in which its assumptions are valid.

Using this method, we found that within our galaxy only PBHs with subsolar masses can have relevant luminosities. For PBH with masses in the range $10^{-5}-10^{-4}\,M_{\odot}$ and axion with masses of $4\times10^{-8}-4\times10^{-7}$ eV, the luminosity emitted by the system could be detected by the LOFAR telescope. This range of PBH masses is the same as that used to explain some microlensing events measured by the OGLE experiment.

The work done regarding this topic motivates different future lines of research. For instance, in our work we considered only the light coming from one single PBH, the closest one. However, we could extend our analysis considering the stochastic signal produced by cosmological populations of PBHs.

There are also several ways in which the modeling of the astrophysical environment around the Black Hole could be improved. In our analysis, we restricted the parameter space to regions where the plasma electrons behave non-relativistically around the conversion point, so it would be interesting to go beyond this case and include relativistic effects. Besides this, the Bondi model we used in our work assumes a spherically symmetric process of accretion. It would be important to improve this by using models that account for the angular momentum of the Black Hole.

We also restricted our work to avoid the case where the axion-photon conversion produces large magnetic fields, which would lead to a snowball effect. Our treatment

would not be valid if such instability takes place, but the luminosities in this case could be much larger than those we predicted.

References

[1] S. De Curtis, L. Delle Rose, A. Guiggiani, A. Gil Muyor and G. Panico, *Bubble wall dynamics at the electroweak phase transition*, *Journal of High Energy Physics* **2022** (2022) .

[2] S. De Curtis, L. Delle Rose, A. Guiggiani, A. Gil Muyor and G. Panico, *Collision integrals for cosmological phase transitions*, *Journal of High Energy Physics* **2023** (2023) .

[3] R. Z. Ferreira and A. Gil Muyor, *Lighten up Primordial Black Holes in the Galaxy with the QCD axion: Signals at the LOFAR Telescope*, 2404.12437.

[4] S. P. Martin, *A Supersymmetry Primer*, *Advanced Series on Directions in High Energy Physics* (1998) 1–98.

[5] M. Drewes, *The Phenomenology of Right Handed Neutrinos*, *International Journal of Modern Physics E* **22** (2013) 1330019.

[6] J. Ellis, M. Lewicki, M. Merchand, J. M. No and M. Zych, *The scalar singlet extension of the Standard Model: gravitational waves versus baryogenesis*, *Journal of High Energy Physics* **2023** (2023) .

[7] G. C. Dorsch, S. J. Huber and J. M. No, *A strong electroweak phase transition in the 2HDM after LHC8*, *Journal of High Energy Physics* **2013** (2013) .

[8] G. Bernardi, E. Brost, D. Denisov, G. Landsberg, M. Aleksa, D. d'Enterria et al., *The Future Circular Collider: a Summary for the US 2021 Snowmass Process*, 2022.

[9] C. Caprini, M. Chala, G. C. Dorsch, M. Hindmarsh, S. J. Huber, T. Konstandin et al., *Detecting gravitational waves from cosmological phase transitions with LISA: an update*, *Journal of Cosmology and Astroparticle Physics* **2020** (2020) 024–024.

[10] P. Auclair, D. Bacon, T. Baker, T. Barreiro, N. Bartolo, E. Belgacem et al., *Cosmology with the Laser Interferometer Space Antenna*, 2022.

[11] M. Maggiore, C. V. D. Broeck, N. Bartolo, E. Belgacem, D. Bertacca, M. A. Bizouard et al., *Science case for the Einstein telescope*, *Journal of Cosmology and Astroparticle Physics* **2020** (2020) 050–050.

[12] A. Weltman, P. Bull, S. Camera, K. Kelley, H. Padmanabhan, J. Pritchard et al., *Fundamental physics with the Square Kilometre Array*, *Publications of the Astronomical Society of Australia* **37** (2020) .

[13] K. Abazajian, A. Abdulghafour, G. E. Addison, P. Adshead, Z. Ahmed, M. Ajello et al., *Snowmass 2021 CMB-S4 White Paper*, 2022.

[14] D. E. Morrissey and M. J. Ramsey-Musolf, *Electroweak baryogenesis*, *New Journal of Physics* **14** (2012) 125003.

[15] S. De Curtis, L. Delle Rose, A. Guiggiani, A. Gil Muyor and G. Panico, *Dynamics of bubble walls at the electroweak phase transition*, *EPJ Web Conf.* **270** (2022) 00035 [2209.06509].

[16] S. De Curtis, L. Delle Rose, A. Guiggiani, A. Gil Muyor and G. Panico, *Bubble wall dynamics at the electroweak scale*, *PoS* **ICHEP2022** (2022) 080.

[17] S. De Curtis, L. Delle Rose, A. Guiggiani, A. Gil Muyor and G. Panico, *Non-linearities in cosmological bubble wall dynamics*, *JHEP* **05** (2024) 009 [2401.13522].

[18] R. D. Peccei and H. R. Quinn, CP *Conservation in the Presence of Pseudoparticles*, *Phys. Rev. Lett.* **38** (1977) 1440.

[19] D. J. Marsh, *Axion cosmology*, *Physics Reports* **643** (2016) 1–79.

[20] E. Aprile, K. Abe, F. Agostini, S. Ahmed Maouloud, L. Althueser, B. Andrieu et al., *Search for new physics in electronic recoil data from xenonnt*, *Physical Review Letters* **129** (2022) .

[21] C. Boutan, B. H. LaRoque, E. Lentz, N. S. Oblath, M. S. Taubman, J. Tedeschi et al., *Axion Dark Matter eXperiment: Run 1A Analysis Details*, 2023.

[22] A. Hook, Y. Kahn, B. R. Safdi and Z. Sun, *Radio Signals from Axion Dark Matter Conversion in Neutron Star Magnetospheres*, *Phys. Rev. Lett.* **121** (2018) 241102.

[23] B. R. Safdi, Z. Sun and A. Y. Chen, *Detecting axion dark matter with radio lines from neutron star populations*, *Physical Review D* **99** (2019) .

[24] R. A. Battye, B. Garbrecht, J. I. McDonald, F. Pace and S. Srinivasan, *Dark matter axion detection in the radio/mm-waveband*, *Phys. Rev. D* **102** (2020) 023504 [1910.11907].

[25] M. Leroy, M. Chianese, T. D. Edwards and C. Weniger, *Radio signal of axion-photon conversion in neutron stars: A ray tracing analysis*, *Physical Review D* **101** (2020) .

[26] S. J. Witte, D. Noordhuis, T. D. P. Edwards and C. Weniger, *Axion-photon conversion in neutron star magnetospheres: The role of the plasma in the Goldreich-Julian model*, *Phys. Rev. D* **104** (2021) 103030 [2104.07670].

[27] A. J. Millar, S. Baum, M. Lawson and M. C. D. Marsh, *Axion-photon conversion in strongly magnetised plasmas*, *JCAP* **11** (2021) 013 [2107.07399].

[28] J. W. Foster, S. J. Witte, M. Lawson, T. Linden, V. Gajjar, C. Weniger et al., *Extraterrestrial Axion Search with the Breakthrough Listen Galactic Center Survey*, *Phys. Rev. Lett.* **129** (2022) 251102 [2202.08274].

[29] H. Niikura, M. Takada, S. Yokoyama, T. Sumi and S. Masaki, *Constraints on Earth-mass primordial black holes from OGLE 5-year microlensing events*, *Phys. Rev. D* **99** (2019) 083503 [1901.07120].

[30] Y. Nambu and G. Jona-Lasinio, *Dynamical Model of Elementary Particles Based on an Analogy with Superconductivity. I*, *Phys. Rev.* **122** (1961) 345.

[31] F. Englert and R. Brout, *Broken Symmetry and the Mass of Gauge Vector Mesons*, *Phys. Rev. Lett.* **13** (1964) 321.

[32] P. W. Higgs, *Broken Symmetries and the Masses of Gauge Bosons*, *Phys. Rev. Lett.* **13** (1964) 508.

[33] G. S. Guralnik, C. R. Hagen and T. W. B. Kibble, *Global Conservation Laws and Massless Particles*, *Phys. Rev. Lett.* **13** (1964) 585.

[34] S. Elitzur, *Impossibility of spontaneously breaking local symmetries*, *Phys. Rev. D* **12** (1975) 3978.

[35] J. Fröhlich, G. Morchio and F. Strocchi, *Higgs phenomenon without symmetry breaking order parameter*, *Nuclear Physics B* **190** (1981) 553.

[36] M. E. Peskin and D. V. Schroeder, *An introduction to quantum field theory*. Westview, 1995.

[37] M. Quiros, *Finite temperature field theory and phase transitions*, 1999.

[38] M. Hindmarsh, M. Lüben, J. Lumma and M. Pauly, *Phase transitions in the early universe*, *SciPost Physics Lecture Notes* (2021) .

[39] F. Bigazzi, A. Caddeo, T. Canneti and A. L. Cotrone, *Bubble wall velocity at strong coupling*, *Journal of High Energy Physics* **2021** (2021) .

[40] G. D. Moore and T. Prokopec, *How fast can the wall move? A study of the electroweak phase transition dynamics*, *Physical Review D* **52** (1995) 7182–7204.

[41] S. Coleman, *Fate of the false vacuum: Semiclassical theory*, *Phys. Rev. D* **15** (1977) 2929.

[42] C. G. Callan and S. Coleman, *Fate of the false vacuum. II. First quantum corrections*, *Phys. Rev. D* **16** (1977) 1762.

[43] A. Linde, *Fate of the false vacuum at finite temperature: Theory and applications*, *Physics Letters B* **100** (1981) 37.

[44] J. Kripfganz, A. Laser and M. G. Schmidt, *Critical bubbles and fluctuations at the electroweak phase transition*, *Nuclear Physics B* **433** (1995) 467–497.

[45] A. Guiggiani, *Bubble dynamics at the electroweak scale*, 2024.

[46] D. Cutting, M. Hindmarsh and D. J. Weir, *Gravitational waves from vacuum first-order phase transitions: From the envelope to the lattice*, *Physical Review D* **97** (2018) .

[47] D. Cutting, E. G. Escartin, M. Hindmarsh and D. J. Weir, *Gravitational waves from vacuum first-order phase transitions. II. From thin to thick walls*, *Physical Review D* **103** (2021) .

[48] R. Jinno, T. Konstandin, H. Rubira and I. Stomberg, *Higgsless simulations of cosmological phase transitions and gravitational waves*, *Journal of Cosmology and Astroparticle Physics* **2023** (2023) 011.

[49] F. Giese, T. Konstandin and J. v. de Vis, *Model-independent energy budget of cosmological first-order phase transitions—A sound argument to go beyond the bag model*, *Journal of Cosmology and Astroparticle Physics* **2020** (2020) 057–057.

[50] C. Gowling and M. Hindmarsh, *Observational prospects for phase transitions at LISA: Fisher matrix analysis*, *Journal of Cosmology and Astroparticle Physics* **2021** (2021) 039.

[51] L. Canetti, M. Drewes and M. Shaposhnikov, *Matter and antimatter in the universe*, *New Journal of Physics* **14** (2012) 095012.

[52] A. D. Sakharov, *Violation of CP invariance, C asymmetry, and baryon asymmetry of the universe*, *Soviet Physics Uspekhi* **34** (1991) 392.

[53] J. M. Cline, *Baryogenesis*, `hep-ph/0609145`.

[54] A. Friedlander, I. Banta, J. M. Cline and D. Tucker-Smith, *Wall speed and shape in singlet-assisted strong electroweak phase transitions*, *Physical Review D* **103** (2021) .

[55] P. Arnold, G. D. Moore and L. G. Yaffe, *Transport coefficients in high temperature gauge theories (I): leading-log results*, *Journal of High Energy Physics* **2000** (2000) 001–001.

[56] P. Arnold, G. D. Moore and L. G. Yaffe, *Transport coefficients in high temperature gauge theories (II): beyond leading log*, *Journal of High Energy Physics* **2003** (2003) 051–051.

[57] G. Moore and T. Prokopec, *Bubble Wall Velocity in a First Order Electroweak Phase Transition*, *Physical Review Letters* **75** (1995) 777–780.

[58] B. Laurent and J. M. Cline, *Fluid equations for fast-moving electroweak bubble walls*, *Physical Review D* **102** (2020) .

[59] G. C. Dorsch, S. J. Huber and T. Konstandin, *On the wall velocity dependence of electroweak baryogenesis*, *Journal of Cosmology and Astroparticle Physics* **2021** (2021) 020.

[60] B. Laurent and J. M. Cline, *First principles determination of bubble wall velocity*, *Physical Review D* **106** (2022) .

[61] J. M. Cline and K. Kainulainen, *Electroweak baryogenesis at high bubble wall velocities*, *Physical Review D* **101** (2020) .

[62] G. C. Dorsch, S. J. Huber and T. Konstandin, *A sonic boom in bubble wall friction*, *Journal of Cosmology and Astroparticle Physics* **2022** (2022) 010.

[63] J. R. Espinosa, T. Konstandin, J. M. No and G. Servant, *Energy budget of cosmological first-order phase transitions*, *Journal of Cosmology and Astroparticle Physics* **2010** (2010) 028–028.

[64] A. Hook, *TASI Lectures on the Strong CP Problem and Axions*, 1812.02669.

[65] C. Vafa and E. Witten, *Parity Conservation in Quantum Chromodynamics*, *Phys. Rev. Lett.* **53** (1984) 535.

[66] L. Di Luzio, M. Giannotti, E. Nardi and L. Visinelli, *The landscape of QCD axion models*, *Physics Reports* **870** (2020) 1–117.

[67] F. Bigazzi, A. Caddeo, A. L. Cotrone, P. Di Vecchia and A. Marzolla, *The holographic QCD axion*, *Journal of High Energy Physics* **2019** (2019) .

[68] G. G. di Cortona, E. Hardy, J. P. Vega and G. Villadoro, *The QCD axion, precisely*, *Journal of High Energy Physics* **2016** (2016) .

[69] A. Ringwald, *Axions and Axion-Like Particles*, 2014.

[70] F. Arias-Aragón, F. D'Eramo, R. Z. Ferreira, L. Merlo and A. Notari, *Production of thermal axions across the electroweak phase transition*, *Journal of Cosmology and Astroparticle Physics* **2021** (2021) 090.

[71] P. Agrawal, J. Fan, M. Reece and L.-T. Wang, *Experimental targets for photon couplings of the qcd axion*, *Journal of High Energy Physics* **2018** (2018) .

[72] G. Raffelt and A. Caputo, *Astrophysical Axion Bounds: The 2024 Edition*, in *Proceedings of 1st General Meeting and 1st Training School of the COST Action COSMIC WSIPers — PoS(COSMICWISPers)*, COSMICWISPers, Sissa Medialab, Mar., 2024, DOI.

[73] N. Vinyoles, A. Serenelli, F. Villante, S. Basu, J. Redondo and J. Isern, *New axion and hidden photon constraints from a solar data global fit*, *Journal of Cosmology and Astroparticle Physics* **2015** (2015) 015–015.

[74] D. Cadamuro, *Cosmological limits on axions and axion-like particles*, 2012.

[75] A. Notari, F. Rompineve and G. Villadoro, *Improved hot dark matter bound on the QCD axion*, 2022.

[76] R. Z. Ferreira and A. Notari, *Observable Windows for the QCD Axion Through the Number of Relativistic Species*, *Physical Review Letters* **120** (2018) .

[77] C. Beaufort, M. Bastero-Gil, T. Luce and D. Santos, *New solar X-ray constraints on keV Axion-Like Particles*, 2023.

[78] E. Komatsu, *New physics from the polarized light of the cosmic microwave background*, *Nature Reviews Physics* **4** (2022) 452–469.

[79] T. Fujita, K. Murai, H. Nakatsuka and S. Tsujikawa, *Detection of isotropic cosmic birefringence and its implications for axionlike particles including dark energy*, *Physical Review D* **103** (2021) .

[80] K. Murai, F. Naokawa, T. Namikawa and E. Komatsu, *Isotropic cosmic birefringence from early dark energy*, *Physical Review D* **107** (2023) .

[81] R. Z. Ferreira, S. Gasparotto, T. Hiramatsu, I. Obata and O. Pujolas, *Axionic defects in the CMB: birefringence and gravitational waves*, 2024.

[82] J. Han, *Observing interstellar and intergalactic magnetic fields*, *Annual Review of Astronomy and Astrophysics* **55** (2017) 111.

[83] P. Esposito, N. Rea and G. L. Israel, *Magnetars: A Short Review and Some Sparse Considerations*. Springer Berlin Heidelberg, Oct., 2020, 10.1007/978-3-662-62110-3_3.

[84] G. Raffelt and L. Stodolsky, *Mixing of the photon with low-mass particles*, *Phys. Rev. D* **37** (1988) 1237.

[85] C. Csáki, N. Kaloper and J. Terning, *Dimming Supernovae without Cosmic Acceleration*, *Physical Review Letters* **88** (2002) .

[86] K. M. Ferrière, *The interstellar environment of our galaxy*, *Reviews of Modern Physics* **73** (2001) 1031–1066.

[87] B. T. Draine, *Physics of the interstellar and intergalactic medium*. Princeton University Press, 2010.

[88] M. C. D. Marsh, J. H. Matthews, C. Reynolds and P. Carenza, *The Fourier formalism for relativistic axion-photon conversion, with astrophysical applications*, 2107.08040.

[89] F. P. Huang, K. Kadota, T. Sekiguchi and H. Tashiro, *Radio telescope search for the resonant conversion of cold dark matter axions from the magnetized astrophysical sources*, *Physical Review D* **97** (2018) .

[90] A. J. Millar, G. G. Raffelt, J. Redondo and F. D. Steffen, *Dielectric haloscopes to search for axion dark matter: theoretical foundations*, *J. Cosmol. Astropart. Phys.* **2017** (2017) 061–061.

[91] C. Deffayet, D. Harari, J.-P. Uzan and M. Zaldarriaga, *Dimming of supernovae by photon pseudoscalar conversion and the intergalactic plasma*, *Phys. Rev. D* **66** (2002) 043517 [hep-ph/0112118].

[92] R. Penrose and R. M. Floyd, *Extraction of Rotational Energy from a Black Hole*, *Nat. Phys. Sci.* **229** (1971) 177.

[93] R. Brito, V. Cardoso and P. Pani, *Superradiance, New Frontiers in Black Hole Physics*. Springer International Publishing, 2020, 10.1007/978-3-030-46622-0.

[94] C. Ünal, F. Pacucci and A. Loeb, *Properties of ultralight bosons from heavy quasar spins via superradiance*, *Journal of Cosmology and Astroparticle Physics* **2021** (2021) 007.

[95] A. Arvanitaki, M. Baryakhtar and X. Huang, *Discovering the QCD axion with black holes and gravitational waves*, *Phys. Rev. D* **91** (2015) 084011.

Part II
Papers

Paper 1: Bubble wall dynamics at the electroweak phase transition

JHEP

Published for SISSA by Springer

Received: January 28, 2022
Accepted: March 8, 2022
Published: March 24, 2022

Bubble wall dynamics at the electroweak phase transition

Stefania De Curtis,[a] **Luigi Delle Rose,**[b] **Andrea Guiggiani,**[a] **Ángel Gil Muyor**[b] **and Giuliano Panico**[a]

[a] *INFN Sezione di Firenze and Dipartimento di Fisica e Astronomia, Università di Firenze, Via G. Sansone 1, I-50019 Sesto Fiorentino, Italy*

[b] *IFAE and BIST, Universitat Autònoma de Barcelona, 08193 Bellaterra, Barcelona, Spain*

E-mail: stefania.decurtis@fi.infn.it, ldellerose@ifae.es, andrea.guiggiani@unifi.it, agil@ifae.es, giuliano.panico@unifi.it

Abstract: First order phase transitions could play a major role in the early universe, providing important phenomenological consequences, such as the production of gravitational waves and the generation of baryon asymmetry. An important aspect that determines the properties of the phase transition is the dynamics of the true-vacuum bubbles, which is controlled by the density perturbations in the hot plasma. We study this aspect presenting, for the first time, the full solution of the linearized Boltzmann equation for the top quark species coupled to the Higgs field during a first-order electroweak phase transition. Our approach, differently from the traditional one based on the fluid approximation, does not rely on any ansatz and can fully capture the density perturbations in the plasma. We find that our results significantly differ from the ones obtained in the fluid approximation (including its extensions and modifications), both at the qualitative and quantitative level. In particular sizable differences are found for the friction acting on the bubble wall.

Keywords: Cosmology of Theories BSM, Early Universe Particle Physics, Phase Transitions in the Early Universe

ArXiv ePrint: 2201.08220

https://doi.org/10.1007/JHEP03(2022)163

JHEP03(2022)163

Contents

JHEP03(2022)163

1 Introduction

First order phase transitions (PhTs) in the early Universe proceed through the nucleation of bubbles of a stable phase within a metastable background. Afterwards bubbles expand in the hot plasma and coalesce, filling the whole space. This sequence of processes is characterised by a huge amount of energy stored in the gradients of the scalar field controlling the transition, in sound waves and turbulence in the plasma, all of them sourcing a stochastic background of gravitational waves.

The recent observation of gravitational waves has renewed a vivid interest in the study of the dynamics of such transitions. Indeed, the sensitivity regions of future experiments, such as the European interferometer LISA [1, 2], the Japanese project DECIGO [3, 4] and the Chinese Taiji [5, 6] and TianQin [7] proposals, will probe a range of the expected peak frequencies of PhTs at the electroweak (EW) scale. These interferometers will provide us with a new tool that can support collider experiments in the quest for the physics beyond the Standard Model (BSM), in particular for theories potentially affecting the dynamics of the EW symmetry breaking.

Furthermore, a stochastic gravitational wave background is not the only cosmological relic left after the completion of a PhT. A matter-antimatter asymmetry, dark matter remnants, primordial black holes, magnetic fields and other topological defects can also be produced. A quantitative determination of these quantities obviously requires an accurate

modelling of the PhT dynamics. This is controlled, among few other parameters, by the propagation velocity of the bubble wall.

In the steady state regime, the speed of the wall is a result of the balance of the internal pressure, due to the potential difference between the two phases, and the external friction exerted by the plasma particles impinging on the wall. In fact, the motion of a bubble drives the plasma out of equilibrium inducing a backreaction that slows down its propagation. Despite its relevance and the huge amount of literature on the topic, see for instance [8–40] for an incomplete list, this is one of the parameters on which we have less theoretical control.

The first computation of the bubble speed in the SM can be found in the seminal work of Moore and Prokopec [8, 9] where the authors explicitly determined the friction induced by the plasma on the wall from a microphysics calculation, namely by evaluating all the relevant interactions between the plasma particles and the bubble. This requires the determination of the deviations from the equilibrium distributions of the different species in the plasma through the solution of the corresponding Boltzmann equations.

Other phenomenological approaches have also been explored which rely, instead, on a parameterization of the friction in terms of a viscosity parameter [32–40].

The formalism introduced in refs. [8, 9], that we will denote as the "old formalism", necessarily requires the use of an ansatz for the distribution functions. This is needed to parametrize their momentum dependence and, then, to compute the local collision integral of the Boltzmann equation. In ref. [9] the fluid approximation was employed assuming that the deviation from the equilibrium distributions is entirely described by only three perturbations for each species in the plasma: the chemical potential, the temperature and the velocity fluctuations. The perturbations are then extracted by taking moments of the Boltzmann equation with suitable weights. In practice, the integro-differential Boltzmann equation is converted into a much simpler system of ordinary differential equations. By construction, the fluid approximation is equivalent to a first order expansion in the momenta of the deviation from the equilibrium distribution functions.

A peculiar feature of the fluid approximation is that the Liouville operator of the Boltzmann equation develops a zero eigenvalue at the speed of sound c_s and, for larger velocities, all the perturbations trail the source term. This implies that any non-equilibrium dynamics is suppressed in front of the bubble wall [12] with significant consequences especially for non-local EW baryogenesis which would result to be extremely inefficient for bubble walls faster than c_s.

This has been the common lore for many years. But recently in refs. [15, 16] it has been argued that the singularity is only an artifact of the first order truncation in momenta and of the particular set of weights chosen to extract the perturbations. Indeed, different choices of weights can shift the position of the singularity, suggesting that the speed of sound should not be a critical value for the particle diffusion as described by the fluid equations. In ref. [16] this problem was overcome by introducing a "new formalism", as dubbed by the authors, which relies on a different parameterization of the non-equilibrium distributions (specifically for the velocity perturbation), different weights and a factorization ansatz [41]. As a result, the new formalism wipes off the discontinuity at the speed of sound while still providing, for small velocities, quantitatively similar results to the fluid approximation.

JHEP03(2022)163

The same issue has also been recently revisited in ref. [30] for the computation of the baryon asymmetry and in ref. [31] for the computation of the friction on the bubble wall, two problems that share many similarities. In these works the fluid approximation has been generalized by including higher orders in the small momenta expansion and the absence of the singularity for the perturbations of the heavy species has been corroborated. Besides the issue of the singularity, large differences in the friction arise, with respect to the old formalism, when higher orders are included. This confirms that the use of the fluid approximation, other than being not fully justified, is not particularly reliable, neither qualitatively nor quantitatively. A major consequence is that EW-baryogenesis is indeed achievable for supersonic bubbles opening up the parameter space of many BSM models, in which the observed baryon asymmetry can be reproduced while enhancing, at the same time, the strength of the stochastic gravitational wave background.

Even though the absence of the singularity for the heavy massive species could already be inferred in ref. [9], the speed of sound in the plasma still played a peculiar role in the old formalism as it provides a peak in the integrated friction for $v \simeq c_s$.[1] The same peak (possibly accompanied by others, one for each vanishing eigenvalue of the Liouville operator) remains even if higher orders in the momenta expansion are included. As we will clarify with our analysis, such behavior is absent from the actual solution, confirming that the speed of sound is not a critical threshold of the friction for massive species.[2]

The approaches discussed above are clearly affected by ambiguities. First of all, they all rely on an ansatz for the shape of non-equilibrium distribution functions which, both in the new and old formalisms (extended or not), is unavoidable in order to compute the collision integrals. Moreover, the choice of the basis and of the weights is not unique and different ansatzes have important qualitative and quantitative impacts on the resulting distribution functions. As such, a full solution of the Boltzmann equation that does not impose any specific momentum dependence is necessary to provide reliable quantitative predictions for both the non-equilibrium distribution functions and the friction exerted on the bubble wall, and to clarify the issue of the presence of a singularity. In fact, by feeding these new results into the equation of motion of the Higgs field, one will be able to carry out a precise computation of the wall speed and of the actual profile of the domain wall (DW). This is a necessary step towards a quantitative and reliable method to asses the potential of a given BSM extension to yield interesting predictions for the relics mentioned above. This is the goal of the present work.

In this paper we will present, for the first time, a fully quantitative solution of the Boltzmann equation. Since the absence of an ansatz prevents the direct computation of the collision integral, in order to extract the solution we will adopt an iterative method. In

[1] This is true for a wide range of parameters of the model, in particular if the wall thickness is not too large and the interaction strength among the plasma particles is not too strong. If these conditions are not valid, a smooth behavior can be present, as found in ref. [31].

[2] For all the massless background species, as pointed out in ref. [9] and confirmed in ref. [31] through hydrodynamic considerations [31, 33, 42–44], a discontinuity of the temperature and fluid velocity at the bubble front for bubble velocities close to the speed of sound could be present. This discontinuity turns into a singularity of the background perturbations at c_s in the linearized Boltzmann equation.

JHEP03(2022)163

particular, as it will be detailed below, the collision integral can be split into two parts, one proportional to the solution itself and another effectively treated as a source term. At each iteration, the latter is evaluated using the solution obtained at the previous step. With a clever choice of the starting solution, convergence can be reached within a very small number of steps.

For the purpose of presenting the methodology and to quantitatively asses the differences among the aforementioned formalisms, we will consider the EWPhT and we will focus on the study of top quark species, the one with the strongest coupling, among the SM particles, to the Higgs profile and, as such, the one that provides the largest contribution to the friction. We leave for a future work the inclusion of the electroweak gauge bosons and of the background species.

The paper is organized as follows: in section 2 we describe our method while in section 3 we present and discuss the numerical results. In section 4 we give our conclusions and discuss future directions. All the technicalities related to the computation of the collision integrals are discussed in appendix A.

2 The Boltzmann equation

As discussed in the Introduction, our goal is to determine the solution of the Botzmann equation for the distribution function of the plasma in the presence of an expanding bubble of true vacuum. Once the bubble reaches a radius much larger than the thickness of its wall, to a good approximation we can adopt the planar limit, considering a flat DW with a velocity parallel to its normal vector.

Assuming that (for long enough time) a steady state is reached, it is convenient to write the Boltzmann equation in the wall frame (i.e. the frame in which the DW is at rest) in which the solutions are stationary. Orienting the z axis along the velocity of the DW, the equation for the distribution function f of a particle species in the plasma is

$$\mathcal{L}[f] \equiv \left(\frac{p_z}{E} \partial_z - \frac{(m^2(z))'}{2E} \partial_{p_z} \right) f = -\mathcal{C}[f] \,, \tag{2.1}$$

where $m(z)$ is the mass of the particle, which in general depends on the position z, and $(m^2)' \equiv dm^2/dz$. The term $\mathcal{C}$ appearing in the right hand side of the equation is the collision integral, describing local microscopic interactions among the plasma particles, while $\mathcal{L}$ is the Liouville operator.

The collision term ensures that far from the DW, where the forces acting on the system basically vanish, each particle species approaches local thermal equilibrium. In the presence of a background fluid with a large number of degrees of freedom (in our case given by gluons and light quarks, which are not much affected by the Higgs phase transition), we can assume that the local thermal equilibrium is described by the standard Fermi or Bose-Einstein distributions for a fluid moving with velocity v along the z axis,[3] namely

$$f_v = \frac{1}{e^{\beta\gamma(E - v p_z)} \pm 1} \,, \tag{2.2}$$

with $\beta = 1/T$ and $\gamma = 1/\sqrt{1 - v^2}$.

[3] This corresponds to choose the DW to move with velocity $-v$ along the z direction in the plasma frame.

JHEP03(2022)163

Deviations with respect to the local equilibrium distribution are present mostly close to the DW and are expected to vanish for $z \to \pm\infty$. For small perturbations, the distribution function can be written as $f = f_v + \delta f$ and the Boltzmann equation can be linearized in δf:

$$\left(\frac{p_z}{E}\partial_z - \frac{(m(z)^2)'}{2E}\partial_{p_z}\right)\delta f + \overline{\mathcal{C}}[\delta f] = \frac{(m(z)^2)'}{2E}\partial_{p_z} f_v = \beta\gamma v \frac{(m(z)^2)'}{2E} f_v' \,, \tag{2.3}$$

where we defined

$$f_v' \equiv -\frac{e^{\beta\gamma(E - v p_z)}}{(e^{\beta\gamma(E-vp_z)} \pm 1)^2} \,, \tag{2.4}$$

and $\overline{\mathcal{C}}[\delta f]$ denotes the collision integral linearized in δf. Notice that the only source term in the linearized Boltzmann equation comes from the Liouville operator $\mathcal{L}$ applied to the local equilibrium distribution. The collision integral, on the contrary, vanishes when computed on f_v, $\mathcal{C}[f_v] = 0$. Sizable values for the source term are therefore present only close to the DW, where the non-trivial Higgs profile generates a non-negligible z dependence in $m(z)$. Away from the DW, the Higgs profile is instead almost constant, thus giving $(m^2)' \simeq 0$ and suppressing the source term. This behavior is in agreement with the naive expectation that deviations from local thermal equilibrium are only present close to the DW and should decrease to zero away from it.

2.1 Flow paths and the Liouville operator

As a first step towards finding a solution of the Boltzmann equation, we need to rewrite the Liouville differential operator in a simpler form.[4] It is straightforward to check that, along the paths on which both the transverse momentum[5] $p_\perp$ and the quantity $p_z^2 + m^2(z)$ are constant, the differential operator simply reduces to a total derivative with respect to z:

$$\mathcal{L} = \left(\frac{p_z}{E}\partial_z - \frac{(m^2(z))'}{2E}\partial_{p_z}\right) \quad \to \quad \frac{p_z}{E}\frac{d}{dz} \,. \tag{2.5}$$

The physical interpretation of the paths is quite intuitive. They correspond to the trajectories of the particles in the $(p_\perp, p_z, z)$ phase space in the collisionless limit. In this limit the energy of the particles and their momentum parallel to the DW are conserved (due to time invariance and translation invariance along the DW), therefore the trajectories of the particles are given by

$$\begin{cases} E = \sqrt{p_\perp^2 + p_z^2 + m^2(z)} = \text{const} \\ p_\perp = \text{const} \end{cases} \quad \Rightarrow \quad p_z^2 + m(z)^2 = \text{const} \,. \tag{2.6}$$

The condition $p_z^2 + m^2(z) = \text{const}$ gives rise to different classes of *flow paths*. Since the mass of the particle species receives a contribution from the Higgs VEV, we expect it to smoothly increase going from the symmetric phase outside the bubble to the symmetry-broken one inside it. In particular, if we are interested in particles whose mass comes

[4] The strategy we use to rewrite the Boltzmann equation is the well-known "method of characteristics" for first-order partial differential equations.

[5] That is the component of the momentum parallel to the DW.

JHEP03(2022)163

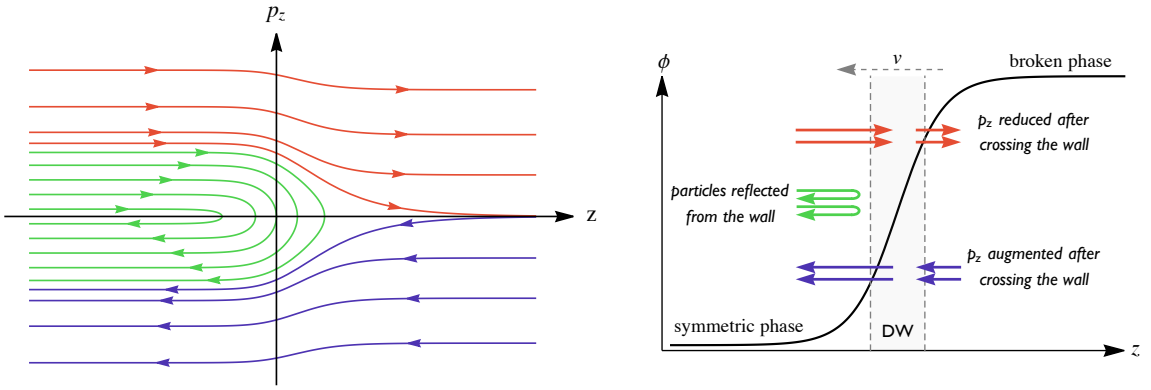

Figure 1. Left panel: paths with fixed energy and transverse momentum in the $z-p_z$ phase space for the choice $m(z) \propto 1+\tanh(z/L)$. The red, green and purple colors denote sets of contours with different behavior. The arrows show the flow of a particle within the phase space. Right panel: schematic representation of the behavior of the particles across the DW.

entirely from EW symmetry breaking (as it happens for the top quark and for the W and Z bosons), we can assume that $m(z) \to 0$ for $z \to -\infty$, while it approaches a constant value $m(z) \to m_0 > 0$ for $z \to +\infty$. In this case three types of flow paths are present:

i) for $p_z(-\infty) \geq m_0$ the path goes from $z = -\infty$ to $z = +\infty$ and has always $p_z > 0$,

ii) for $-m_0 < p_z(-\infty) < m_0$ the path goes from $z = -\infty$ to the point $\bar{z}$ in which $p_z(\bar{z}) = 0$ (i.e. the point that solves the equation $m(\bar{z}) = p_z(-\infty)$) and then goes back to $z = -\infty$,

iii) for $p_z(-\infty) \leq -m_0$ the path goes from $z = +\infty$ to $z = -\infty$ and has always $p_z < 0$.

The three classes of curves are shown schematically in figure 1 for the choice $m(z) \propto 1+\tanh(z/L)$, with L denoting the wall thickness. The paths of type i, ii and iii correspond to the red, green and purple curves respectively.[6]

Exploiting the flow paths we can straightforwardly solve any differential equation of the form

$$\mathcal{L}[\delta f] - \frac{1}{E}\mathcal{Q}\,\delta f = \frac{p_z}{E}\mathcal{S}\,, \tag{2.7}$$

where $\mathcal{Q}$ and $\mathcal{S}$ are generic functions of E, p_z and z, and the factors $1/E$ and p_z/E have been chosen for convenience. Rewriting the above equation along the flow paths we find

$$\left(\frac{d}{dz} - \frac{\mathcal{Q}}{p_z}\right)\delta f = \mathcal{S}\,, \tag{2.8}$$

whose general solution is

$$\delta f = \left[B(p_\perp, p_z^2 + m(z)^2) + \int_{\bar{z}}^{z} e^{-\mathcal{W}(z')}\mathcal{S}\,dz'\right] e^{\mathcal{W}(z)}\,, \tag{2.9}$$

[6]We stress that the approximation, typically used in the literature, in which the $(m^2)'/(2E)\partial_{p_z}\delta f$ term is neglected in the Boltzmann equation could lead to an inaccurate result in our approach. Neglecting that term, in fact, modifies the flow paths making all of them straight lines with fixed p_z. This completely changes the shape of the curves in the region $|p_z| \leq m_0$, thus potentially giving a very different solution of the equation.

JHEP03(2022)163

where $\mathcal{W}$ is given by

$$\mathcal{W}(z) = \int^{z} \frac{\mathcal{Q}}{p_z} dz' \,, \tag{2.10}$$

and all the integrals are evaluated along the flow paths. Notice that the lower integration boundary in the definition of $\mathcal{W}$ can be freely chosen (for each flow path) without affecting the result in eq. (2.9).

The function $B(p_\perp, p_z^2 + m(z)^2)$, which is constant along the flow paths, is arbitrary and can be fixed by enforcing the required boundary conditions. Let us focus separately on the three classes of flow paths.

i) The first type of paths describes particles that travel in the positive z direction, and eventually enter into the bubble. It is natural to choose the boundary conditions in such way that δf vanishes at $z \to -\infty$, that is well before the particle hits the DW. This can be enforced by choosing

$$\delta f = \left[\int_{-\infty}^{z} e^{-\mathcal{W}} \, \mathcal{S} \, dz' \right] e^{\mathcal{W}(z)} \,. \tag{2.11}$$

ii) The second type of paths describes particles that initially travel in the positive z direction, hit the DW and are reflected. It is natural to choose the boundary conditions similarly to what we did for the previous type of paths. Therefore we have

$$\delta f = \left[\int_{-\infty_\uparrow}^{z} e^{-\mathcal{W}} \, \mathcal{S} \, dz' \right] e^{\mathcal{W}(z)} \,, \tag{2.12}$$

where the up arrow in the lower integration boundary indicates that the integration is performed starting from $z \to -\infty$ in the half path with $p_z > 0$.

iii) The third type of paths describes particles that travel in the negative z direction, and eventually exit from the bubble. We can choose the boundary conditions in such way that δf vanishes at $z \to +\infty$, that is well before the particles exit from the bubble. This can be obtained by choosing

$$\delta f = -\left[\int_{z}^{+\infty} e^{-\mathcal{W}} \, \mathcal{S} \, dz' \right] e^{\mathcal{W}(z)} \,. \tag{2.13}$$

The consistency of all these solutions requires $\mathcal{Q} < 0$. We verified numerically that this condition is satisfied for the equations we are considering.

The form of the solution clearly shows the role of the term $(\mathcal{Q}/E)\delta f$ in driving the system towards the local thermal equilibrium, i.e. in decreasing the value of δf. In fact, due to the exponential factors, the impact of the source term $\mathcal{S}$ is exponentially suppressed with the distance. The decay length is of order $\ell \sim p_z/\mathcal{Q}$ and, as expected, decreases for larger values of the collision term.

JHEP03(2022)163

2.2 Finding a solution for the Boltzmann equation

Although the full Boltzmann equation is not of the form of eq. (2.7), we can use the latter to implement an approximation by steps. The basic idea is to split the collision integral $\overline{\mathcal{C}}[\delta f]$ in two pieces: a term analogous to $(\mathcal{Q}/E)\delta f$ in eq. (2.7), and a second term that is included in the source term $\mathcal{S}$ and is used to correct the solution through iterations.

Let us now analyze in details the collision integral. For simplicity we consider the collision term for the $2 \to 2$ processes of a single particle species, but the general case can be treated in an analogous way. The collision integral is given by

$$\mathcal{C}[f] = \sum_i \frac{1}{4N_p E_p} \int \frac{d^3\mathbf{k}\, d^3\mathbf{p}'\, d^3\mathbf{k}'}{(2\pi)^5 2E_k 2E_{p'} 2E_{k'}} |\mathcal{M}_i|^2 \delta^4(p + k - p' - k') \mathcal{P}[f]\,, \tag{2.14}$$

with

$$\mathcal{P}[f] = f(p)f(k)(1 \pm f(p'))(1 \pm f(k')) - f(p')f(k')(1 \pm f(p))(1 \pm f(k))\,, \tag{2.15}$$

where the sum is performed over all the relevant scattering processes, whose squared scattering amplitude is $|\mathcal{M}_i|^2$. In the above formula N_p is the number of degrees of freedom of the incoming particle with momentum p, k is the momentum of the second incoming particle, while p' and k' are the momenta of the outgoing particles. The $\pm$ signs are $+$ for bosons and $-$ for fermions.

From the above expression we can easily derive the collision integral for the linearized Boltzmann equation. As a consequence of the conservation of the total 4-momentum in the collision processes we have that for the local equilibrium distribution $\mathcal{C}[f_v] = 0$. Moreover the linear terms in δf can be expressed as

$$\overline{\mathcal{P}} = f_v(p)f_v(k)(1 \pm f_v(p'))(1 \pm f_v(k')) \sum \frac{\mp \delta f}{f'_v}\,, \tag{2.16}$$

where the $-(+)$ sign in the sum applies to incoming (outgoing) particles.

The $\overline{\mathcal{C}}[\delta f]$ collision integral can therefore be split in two parts. One of them depends only on $\delta f(p)$ and is given by

$$\frac{-f_v(p)}{f'_v(p)} \delta f(p) \sum_i \frac{1}{4N_p E_p} \int \frac{d^3\mathbf{k} d^3\mathbf{p}' d^3\mathbf{k}'}{(2\pi)^5 2E_k 2E_{p'} 2E_{k'}} |\mathcal{M}_i|^2 \delta^4(p+k-p'-k') f_v(k)(1 \pm f_v(p'))(1 \pm f_v(k'))\,. \tag{2.17}$$

This expression is clearly analogous to the term $(\mathcal{Q}/E)\delta f$ in eq. (2.7). The second part of the collision integral includes the terms in which δf depends on k, p' or k' and thus appears under the integral sign. We collectively denote these terms by $\langle \delta f \rangle$. The numerical determination of the various contributions to the collision integral can be drastically simplified through a clever choice of integration variables. The explicit procedure is explained in appendix A.

In order to numerically solve the Boltzmann equation, a possible strategy is to formally rewrite it as eq. (2.7) by including $\langle \delta f \rangle$ in the source term $\mathcal{S}$. The solution can then be found by iteration, inserting into the equation the value of $\langle \delta f \rangle$ obtained by using the solution at the previous step.

JHEP03(2022)163

3 Numerical analysis

In this section we apply the iterative method explained above to numerically solve the Boltzmann equation. For simplicity we focus on a single species in the plasma, the top quark, which is the state with largest coupling to the Higgs and is thus expected to provide one of the most relevant effects controlling the DW dynamics. The analysis of the top quark distribution should be sufficient to provide a robust assessment of the plasma dynamics and to obtain an indication of how much the weighted method used in the literature to solve the Boltzmann equation is qualitatively and quantitatively accurate. We leave for future work the inclusion of the contributions from the W and Z bosons, which are expected to be roughly of the same size as the top quark ones.

The iterative approach explained in the previous section could be straightforwardly applied to determine the solution of the Boltzmann equation. However, in order to improve the convergence of the iterative steps, a slight modified procedure proves more convenient. Since the separation of the collision integral into a contribution to $(\mathcal{Q}/E)\delta f$ and a contribution to $\mathcal{S}$ is to a large extent arbitrary, we can devise a splitting that helps in reducing as much as possible the source term.

3.1 Annihilation only

Focusing on the top quark case, it can be shown that the main contribution to the collision integral comes from the annihilation process $t\bar{t} \to gg$, whereas the scattering of tops on gluons and light quarks gives smaller contributions. In our numerical analysis we will therefore consider at first only the contribution from annihilation, including scattering effects afterwards.

In the annihilation case, the linear terms in the perturbation δf appear in the following combination (see eq. (2.16))

$$\overline{\mathcal{P}} = f_v(p) f_v(k)(1 + f_v^g(p'))(1 + f_v^g(k')) \left(-\frac{\delta f(p)}{f_v'(p)} - \frac{\delta f(k)}{f_v'(k)} \right) , \tag{3.1}$$

where f_v^g denotes the equilibrium distribution for the background gluons (which is approximately unperturbed since the number of degrees of freedom in the background species is large). In the above formula the $\delta f(p)$ and $\delta f(k)$ terms play an analogous role, but their effects become distinct in the collision integral since an integration over k is performed. It is nevertheless evident that the impact of the $\delta f(k)$ term in the Boltzmann equation is not particularly suppressed, as can be understood averaging the equation by integration over p, in which case the $\delta f(p)$ and $\delta f(k)$ become exactly equal. This line of reasoning suggests that treating the $\delta f(k)$ contribution as source term, while including the $\delta f(p)$ term in $(\mathcal{Q}/p_z)\delta f$ might lead to slow convergence. To overcome this difficulty we will use a slightly modified procedure. We rewrite $\overline{\mathcal{P}}$ as

$$\overline{\mathcal{P}} = f_v(p) f_v(k)(1 + f_v^g(p'))(1 + f_v^g(k')) \left[-2\frac{\delta f(p)}{f_v'(p)} + \left(\frac{\delta f(p)}{f_v'(p)} - \frac{\delta f(k)}{f_v'(k)} \right) \right] , \tag{3.2}$$

JHEP03(2022)163

and we interpret the first contribution as $(\mathcal{Q}/p_z)\delta f$, while the second one (the one in round parentheses) is treated as a source. In this way the contribution to the source is partially canceled and faster convergence is achieved.[7]

To determine the numerical solution of the Boltzmann equation we used a dedicated C++ code, validating the results with Mathematica [45]. The solution was computed on a three-dimensional grid in the variables z, $p_\perp$ and p_z restricted to the intervals $z/L \in [-7, 7]$,[8] $p_\perp/T \in [0, 15]$, and $p_z/T \in [-15, +15]$. The solution was computed on a grid with $50 \times 300 \times 100$ points, which was further refined in the region $p_\perp/T < 1$ and $|p_z| \sim m_0$, where the solution showed a fast-varying behavior. Convergence of the solution (at the $\sim 0.1\%$ level) was achieved within three iterative steps for all values of the wall velocity. We modeled the bubble wall assuming that the Higgs profile has the following functional dependence on z [46]:

$$\phi(z) = \frac{\phi_0}{2}[1 + \tanh(z/L)]\,, \tag{3.3}$$

where $L = 5/T$ is the thickness of the bubble wall and $\phi_0 = 150$ GeV is the Higgs VEV in the broken phase. We fixed the phase transition temperature to $T = 100$ GeV. This choice of parameters, as we will see, determines the presence of friction peaks in the old formalism solution. It is thus well suited for differentiating the various formalisms and highlights the differences among them.

An important quantity that can be derived from the numerical solution is the friction acting on the domain wall, which corresponds to the expression [9]

$$F(z) = \frac{dm^2}{dz} N \int \frac{d^3\mathbf{p}}{(2\pi)^3 2E} \delta f(p)\,, \tag{3.4}$$

where N denotes the number of degrees of freedom ($N = 12$ for the top/antitop quark system). In the left panel of figure 2 we show the friction integrated over z as a function of the wall velocity (solid black line). The total friction shows a smooth behavior with a (nearly) linear growth as a function of the wall velocity.

In the same plot we compare our result with the ones obtained with the weighted methods. In particular the green lines correspond to the total friction computed in the old formalism (OF) of ref. [9], taking also into account higher-order terms in the fluid approximation [30]. The old formalism results at order 1, 2 and 3 are given by the dotted, dashed and solid lines respectively. The solid red line, instead, is obtained using the new formalism (NF) of ref. [16].

Our result for small and intermediate velocities, $v \lesssim 0.5$ is in fair numerical agreement with the old formalism ones, which show a minor dependence on the order used for the computation. At higher velocities, instead, the old formalism develops some peaks related to the speed of sound in the plasma and to any other zero eigenvalue of the Liouville operator. The number of peaks and their shape crucially depend on the approximation

[7] We also checked that, in the weighted approach to the solution of the Boltzmann equation, doubling the contribution of $\delta f(p)$ and neglecting $\delta f(k)$ gives a fair approximation of the exact result.

[8] The vanishing boundary conditions on the solution were imposed at the boundaries of the considered region. We verified that this choice does not introduce a significant distortion of the solution.

JHEP03(2022)163

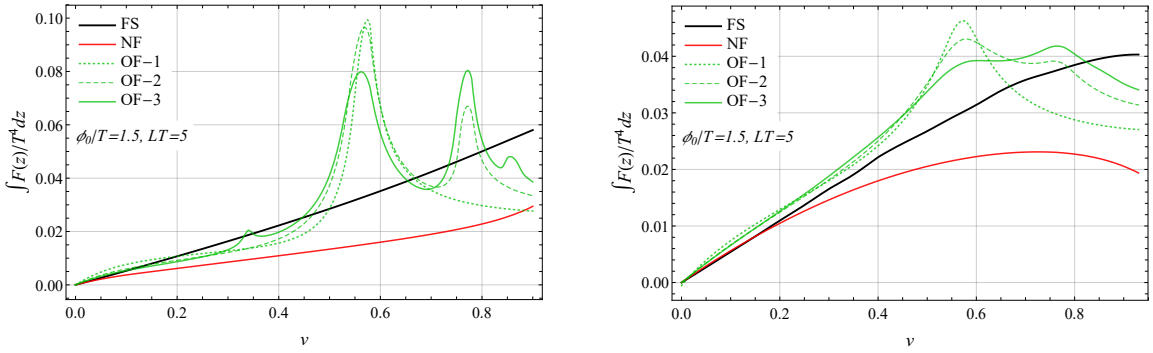

Figure 2. Friction acting on the bubble wall as a function of the velocity. In the left plot only the top annihilation channel has been taken into account, while in the right one both annihilation and scattering are considered. The black solid line corresponds to the solution of the full Boltzmann equation (FS, our result), the dotted, dashed and solid green lines are obtained with the old formalism (OF) at order 1, 2 and 3 respectively [9, 30], while the red line corresponds to the new formalism (NF) [16].

order, denoting an intrinsic instability of the old formalism method.[9] Our results for the full solution of the Boltzmann equation show that the peaks are an artifact of the old formalism approach and that no strong effect is present in the top contributions for velocities close to the sound speed one.

On the other hand, the new formalism correctly predicts a smooth behavior for the total friction for all domain wall velocities. A roughly linear dependence on v is obtained up to $v \simeq 0.8$, while for larger values a faster growth is found, in contrast with the behavior of the full solution (FS) result. The quantitative agreement with the full solution is good only for very low velocities, $v \lesssim 0.1$, while order 50% differences can be seen for higher velocities.

For a more refined comparison of the results we show in figure 3 the behavior of the friction $F(z)$ as a function of the position. The plots clearly show that the overall shape of the friction is very similar in all approaches, the main difference being the height of the peak. This property is not unexpected, since the size of the perturbation δf is controlled by the source term in the Boltzmann equation, whose z dependence is given by dm^2/dz. One can easily check that the shape of all the curves in the plots roughly agree with the function $d\phi^2(z)/dz$.

A more detailed comparison of δf as a function of z, $p_\perp$ and p_z shows drastic differences among all the approaches. Although the overall size of δf is comparable in all formalisms (being controlled by the source term), the various solutions significantly differ even at the qualitative level in most of the kinematic regions. We conclude from this comparison that the fluid approximation is not reliable if we include in the Boltzmann equation only the top annihilation channel. We will see in the following that, introducing the top scattering processes, a better agreement is found.

[9] Notice that the total friction shows a continuous behavior across the sound speed thresholds, whereas in ref. [9] a divergence was found. This difference was expected, since the discontinuity found in ref. [9] is induced by the background contributions, which are not included in our analysis.

JHEP03(2022)163

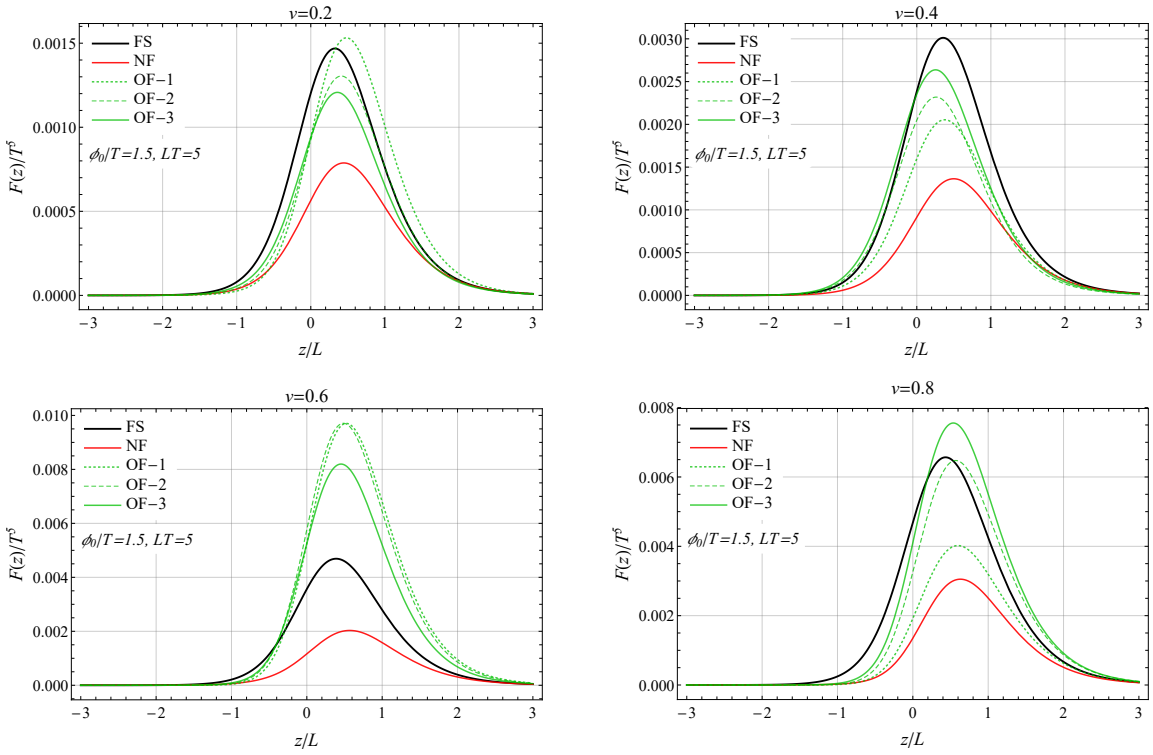

Figure 3. Friction as a function of the position z when only top annihilation processes are taken into account. The plots correspond to the wall velocities $v = 0.2, 0.4, 0.6, 0.8$.

3.2 Full solution

We now consider the Boltzmann equation for the top quark distribution, including in the collision term also the main top scattering processes, namely the ones onto gluons $tg \to tg$ and onto light quarks $tq \to tq$. We found convenient to include these additional contributions treating them as source terms in the iterative steps.

To determine the numerical solution we used a grid analogous to the one described in the annihilation-only case. The convergence of the iterative procedure is somewhat slower when top scattering processes are taken into account. For $v \leq 0.6$ we used the solution of the annihilation-only case as starting ansatz and we performed six iterative steps to reach a good convergence. For higher velocities the annihilation-only solution is not a convenient choice for the first iterative step, thus we started from the full solution determined for a lower value of v. Also in this case six iterations were sufficient to achieve convergence.

We found that the scattering processes significantly modify the solution of the Boltzmann equation, especially for large values of the domain wall velocity ($v \gtrsim 0.5$). The impact on the total friction acting on the domain wall is shown in the right panel of figure 2. Analogously to the annihilation-only case, an almost linear dependence on the wall velocity is present for small and intermediate v values, but a flattening is present at higher velocities. Quantitatively, the scattering processes induce only minor corrections to the total friction for $v \lesssim 0.6$, while a decrease of order 25% is found for $v \sim 0.8$.

JHEP03(2022)163

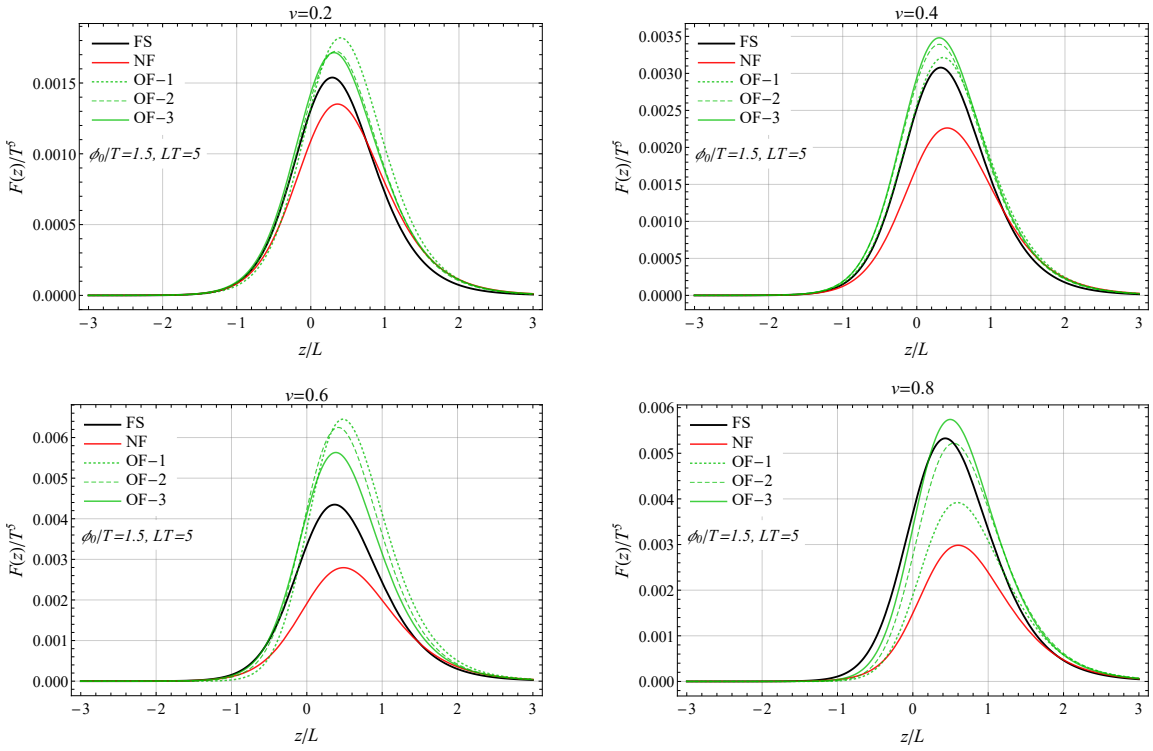

Figure 4. Friction as a function of the position z when top annihilation and scattering processes are taken into account. The plots correspond to the wall velocities $v = 0.2, 0.4, 0.6, 0.8$.

The impact of the scattering processes on the solution obtained through the weighted methods is, on the contrary, much more pronounced. The old formalism approach (green lines in figure 2) including only the lowest-order perturbations predicts a strong peak for $v \simeq 0.55$. The peak however gets substantially reduced once higher-order perturbations are included in the expansion, with a milder additional peak forming for $v \simeq 0.75$. We expect that including additional higher-order perturbations could smoothen the curve, giving a qualitative behavior similar to the one we get with the full solution, with a linear behavior for $v \lesssim 0.6$. At the quantitative level, however, the old formalism solution differs from the one we found by order $10 - 25\%$.

The result obtained through the new formalism (red line in figure 2) is also substantially modified by the scattering contributions. In particular the increase in the friction for $v \gtrsim 0.8$ is removed and a maximum followed by a mild decrease is now found for $v \gtrsim 0.6$. The new formalism prediction is now in good quantitative agreement with our result for $v \lesssim 0.2$, while differences up to order 50% are found for larger velocities.

The friction as a function of the position z for some benchmark wall velocities is shown in figure 4. Analogously to what we found for the total friction, the results we obtain with our method are only mildly modified by the scattering contributions. In particular the shape of the friction remains almost unchanged with only minor modifications in the overall normalization. Similar considerations apply for the shape of the z dependence of the friction in the old and new formalism. In this case, however, significant changes in the overall normalization are found, as expected from the above discussion on the total friction.

JHEP03(2022)163

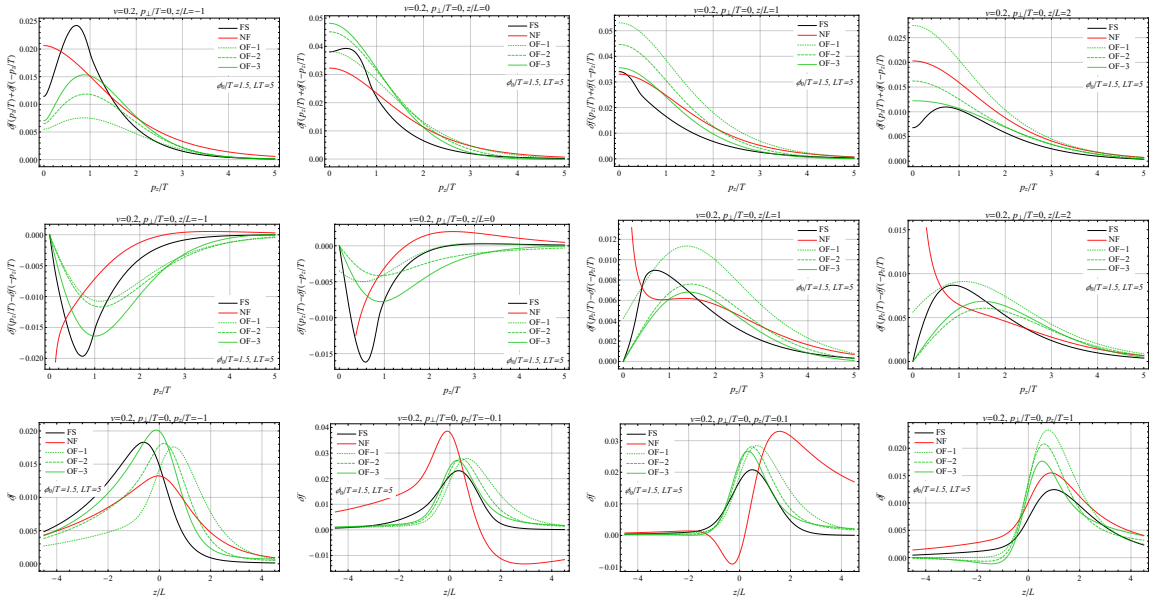

Figure 5. Perturbation δf for $v = 0.2$ and $p_\perp = 0$. The plots on the first (second) row show the even (odd) part of δf as a function of p_z for $z/L = -1, 0, 1, 2$. The third row shows plots of δf as a function of z for $p_z/T = -1, -0.1, 0.1, 1$.

Finally we show in figure 5 the perturbation δf for the benchmark velocity $v = 0.2$. The results for different velocities are qualitatively analogous, the main difference being an overall rescaling with a limited change in shape. The plots show the full solution of the Boltzmann equation we got in our analysis, along with the results obtained applying the old and new weighted approaches. Notice that the new formalism does not fully determine the velocity perturbation, whose impact can only be computed averaging over the momentum through a factorization ansatz [41]. To plot the solution in the new formalism we chose to identify the distribution perturbation with

$$\delta f = -f_v' \left[\mu(z) + \beta\gamma(E - v p_z)\delta\tau\right] + f_v \frac{E}{p_z} u \,, \tag{3.5}$$

following eq. (B5) of ref. [16]. This identification tends to produce a divergent behavior for small p_z, which however has no impact on the determination of the friction since it is odd in p_z.

In the first (second) row of the figure we show the dependence of the even (odd) part of δf on the momentum along the z axis, p_z. The plots are obtained fixing $p_\perp = 0$, but similar results are found for $p_\perp/T \lesssim 2$ (for larger $p_\perp$ the solution is significantly suppressed and its impact on the domain wall dynamics is subleading). The plots in the first row show that, at the qualitative level, the old and new formalisms fairly reproduce the overall shape of the even part of the solution, although a somewhat different behavior is found for small p_z ($|p_z/T| \lesssim 0.5$). This difference is most probably due to the fact that in the weighted approach the

$$-\frac{(m(z)^2)'}{2E}\partial_{p_z}\delta f \tag{3.6}$$

JHEP03(2022)163

term is neglected. This term, although subleading in most of the kinematic space, dominates close to $p_z = 0$, where the $(p_z/E)\partial_z$ term vanishes. In spite of the fair qualitative agreement, large quantitative differences are present between the full solution and the ones obtained with the weighted approaches.

The agreement of the various formalisms in the determination of the odd part of δf proves quite poor. In particular, marked differences are found for $z \lesssim 0$, in which case the high-p_z behavior of the solution is not captured by the old formalism, even including higher-order corrections. A mildly better agreement is found for $z/L \gtrsim 1$. The new formalism tends to reproduce the correct shape for $p_z/T \gtrsim 1$, but presents large differences for small p_z. It must be noticed that the odd part of δf does not contribute to the friction, thus the large differences found among the various solutions do not show up in the determination of $F(z)$.

On the third row of figure 5 we show δf as a function of z for $p_\perp = 0$ and for the benchmark values $p_z/T = -1, -0.1, 0.1, 1$. The old formalism reproduces the overall qualitative behavior of the solution. Higher-order terms tend to improve the agreement, although failing to fully reproduce the full solution, especially at the quantitative level. The new formalism is in qualitative agreement with the full solution for $|p_z/T| \gtrsim 1$, while completely fails to reproduce the correct shape for small p_z.

4 Conclusions and outlook

In this paper we presented for the first time the fully quantitative solution of the Boltzmann equation that describes particle diffusion in the presence of a moving domain wall. Contrary to the existing approaches, we did not rely on any ansatz nor we imposed any momentum dependence on the non-equlibrium distribution functions. This clearly represents a necessary step towards a reliable understanding of the bubble wall dynamics. Using the friction obtained with the numerical method developed in this work, one can solve the equation of motion of the Higgs profile (or of any other scalar field driving a first order PhT) and extract the velocity of the domain wall as well as the features of its shape, such as the wall thickness. These parameters crucially impact on the prospects of any BSM theory to predict interesting cosmological signals, such as a gravitational wave background and the amount of matter-antimatter asymmetry.

We critically compared our results with the ones obtained using the formalisms developed so far in the literature, namely the fluid approximation originally developed in ref. [9], its extended version [30, 31] (we dubbed both approaches 'old formalism', following ref. [16]), and the "new formalism" [16].

To establish our approach, we focused on a slightly simplified set-up in which only the top quark contribution to the DW dynamics is taken into account. Other species can however be included in a straightforward way. We computed numerically the distribution function for the top species and we obtained the friction F that the plasma exerts on the DW. The latter quantity is shown in figure 4 as a function of the position z for the three different setups, namely: the old formalism (OF), the new one (NF) and our full solution (FS). The spatial dependence of the friction is quite similar in the three cases because

JHEP03(2022)163

the overall shape is mainly determined by the source term in the Boltzmann equation, namely $dm^2(z)/dz$. There is however a significant disagreement at the quantitative level, as can be seen in the right panel of figure 2, where the integrated friction is plotted as a function of the DW speed v. For small velocities $v \lesssim 0.2$ a good agreement between the new formalism prediction and the full solution is found, while the old formalism (both original and extended) shows minor differences, of order 10%. The agreement significantly worsens at larger velocities. In this case the new formalism predicts a significantly smaller total friction, reaching a maximum much earlier than the full solution. The old formalism, on the other hand shows a different qualitative behavior, with a series of peaks related to the zero eigenvalues of the Liouville operator. These features, which strongly depend on the order at which one fluid approximation is truncated, do not seem physical and are not present in the full solution, which shows a completely smooth shape (linear behavior for $v \lesssim 0.7$ and a flattening for larger velocities).

In figure 5 we also compare the distribution perturbation δf for the various approaches. Although in some kinematic regions a qualitative agreement can be seen, the differences among all approaches are quite strong. In particular the new formalism shows large differences in the odd part (with respect to p_z) of the perturbation. This difference does not show up in the friction result, since only the even part contributes to $F(z)$.

We add that, as an intermediate step in our procedure, we considered the set-up in which only the annihilation channel for the top quarks is included in the collision integral, excluding the scattering processes. The friction for the full solution proves remarkably similar to the one in the complete set-up (see the left panel of figure 2), apart from the fact that the maximum is reached for larger DW velocities. The old and new formalisms, on the other hand, show drastically different behavior. In particular the old formalism predicts sharp peaks connected to the sound speed. The inclusion of higher orders in the fluid approximation does not seem to achieve convergence in a reliable way.

As we mentioned, for the purpose of presenting the methodology and setting up the stage for a determination of the velocity of the bubble wall, in the present paper we only considered the top quark contribution to the DW dynamics. The inclusion of the electroweak gauge bosons and of the background species is clearly important to obtain quantitatively reliable predictions. We leave the investigation of this aspect for future work.

We also exploited another minor simplification in the computation of the collision integrals, ignoring the space dependence of the collisional kernels (see appendix A), which appears through the top mass in the integrated equilibrium distribution functions. This approximation is also used in the old and new formalisms, and is expected to induce only minor corrections to the results. Within our approach the full space dependence could be taken into account, at the cost of increasing the computation time.

Acknowledgments

We thank J. Kozaczuk and B. Laurent for useful discussions. L.D.R. has been supported by a fellowship from “la Caixa” Foundation (ID 100010434) and from the European Union’s Horizon 2020 research and innovation programme under the Marie Sklodowska-Curie Ac-

JHEP03(2022)163

tion grant agreement No 847648. S.D.C. and G.P. were supported in part by the MIUR under contract 2017FMJFMW (PRIN2017). Á.G.M. has been supported by the Secretariat for Universities and Research of the Ministry of Business and Knowledge of the Government of Catalonia and the European Social Fund and La Caixa through the Becas Postdoctorado Junior Leader (LCF/BQ/PI20/11760032).

A Evaluation of the collision integrals

A.1 The term proportional to $\delta f(p)$

We focus, at first, on the term of the collisional integral proportional to $\delta f(p)$, which, for a single matrix element, reads

$$\mathcal{J}[\delta f]=\frac{-\delta f(p)}{4N_pE_p}\frac{f_v(p)}{f'_v(p)}\int\frac{d^3\mathbf{k}d^3\mathbf{p}'d^3\mathbf{k}'}{(2\pi)^5 2E_k 2E_{p'}2E_{k'}}|\mathcal{M}|^2\delta^4(p+k-p'-k')f_v(k)(1\pm f_v(p'))(1\pm f_v(k')). \tag{A.1}$$

To evaluate the integral it is convenient to change variables through a boost, going to the plasma frame, in which the Boltzmann distribution is the standard equilibrium one f_v. We denote by a bar the momenta in the plasma frame, namely

$$\bar{p}_0=\gamma(E_p-vp_z)\,,\quad \bar{p}_z=\gamma(p_z-vE_p)\,,\quad \bar{p}_\perp=p_\perp\,, \tag{A.2}$$

and analogously for k, p' and k'. We thus get (notice that the integration measure $d^3\mathbf{p}/E_p$ is invariant under boost)

$$\begin{aligned}\overline{\mathcal{J}}[\delta f] = &\frac{-\delta f(p(\bar{p}))}{4N_p\gamma(E_{\bar{p}}+v\bar{p}_z)}\frac{f_0(\bar{p})}{f'_0(\bar{p})} \\ &\times\int\frac{d^3\bar{\mathbf{k}}\,d^3\bar{\mathbf{p}}'\,d^3\bar{\mathbf{k}}'}{(2\pi)^5 2E_{\bar{k}}\,2E_{\bar{p}'}\,2E_{\bar{k}'}}|\mathcal{M}|^2\delta^4(\bar{p}+\bar{k}-\bar{p}'-\bar{k}')\,f_0(\bar{k})(1\pm f_0(\bar{p}'))(1\pm f_0(\bar{k}'))\,.\end{aligned} \tag{A.3}$$

In order to evaluate the integrals, we follow the approach of ref. [9], including only leading log contributions. In this approximation we can also neglect the masses of the particles involved in the scattering. This approximation significantly simplifies the numerical evaluation, since it removes any explicit dependence on the z coordinate in the integrals. Closer inspection of the integral appearing in eq. (A.3) shows that it is invariant under rotation of the three-momentum components of $\bar{p}$, thus it is just a function of $E_{\bar{p}}$.[10]

The evaluation of the integral can be simplified by exploiting the delta function and the symmetries of the integrand. In this way one can perform analytically five of the nine integrals. An efficient parametrization for performing the integration is presented in ref. [47].

In the leading log approximation, only t-channel and u-channel scattering amplitudes are relevant (see table 1). So we can focus on these two types of contributions and neglect s-channel processes (and interference terms).

[10] Rotation invariance is an immediate consequence of the fact that the Boltzmann distribution f_0 depends only on the energy of the particle, while $|\mathcal{M}|^2$ is a function of the kinematic invariants (i.e. the Mandelstam variables).

JHEP03(2022)163

process	$\lvert\mathcal{M}\rvert^2$
$t\bar{t} \to gg$	$\frac{128}{3} g_s^4 \left[\frac{ut}{(t-m_q^2)^2} + \frac{ut}{(u-m_q^2)^2} \right]$
$tg \to tg$	$-\frac{128}{3} g_s^4 \frac{su}{(u-m_q^2)^2} + 96 g_s^4 \frac{s^2+u^2}{(t-m_g^2)^2}$
$tq \to tq$	$160 g_s^4 \frac{s^2+u^2}{(t-m_g^2)^2}$

Table 1. Amplitudes for the scattering processes relevant for the top quark in the leading log approximation. In the $tq \to tq$ process we summed over all massless quarks and antiquarks.

t-channel parametrization. We start by considering amplitudes coming from t-channel diagrams. The integration over $d^3\bar{\mathbf{k}}'$ can be easily performed exploiting the δ-function. The remaining integrals can be handled through a change of variables. As in ref. [47], we introduce the three-momentum $\mathbf{q} \equiv \bar{\mathbf{p}}' - \bar{\mathbf{p}} = \bar{\mathbf{k}} - \bar{\mathbf{k}}'$. Rotational invariance allows us to trivially integrate on the orientation of $\mathbf{q}$. Fixing $\mathbf{q}$ to be along a z' axis, we can express the orientation of the $\bar{\mathbf{p}}$ and $\bar{\mathbf{k}}$ momenta in terms of the polar angles $\theta_{\bar{p}q}$ and $\theta_{\bar{k}q}$ and the azimuthal angle ϕ between the $\bar{\mathbf{p}}$-$\mathbf{q}$ and the $\bar{\mathbf{k}}$-$\mathbf{q}$ plane.

The remaining delta function can be handled by introducing an additional variable ω linked to the t Mandelstam variable as $t \equiv \omega^2 - q^2$, where $q \equiv |\mathbf{q}|$. In this way the integrations on the angles $\theta_{\bar{k}q}$ and $\theta_{\bar{p}q}$ can be performed analytically and one is left with the final expression for the integral on the second line of eq. (A.3):

$$\mathcal{K} = \frac{1}{8(2\pi)^4 E_{\bar{p}}} \int_{-E_{\bar{p}}}^{+\infty} d\omega \int_{|\omega|}^{\omega+2E_{\bar{p}}} dq \int_{\frac{q+\omega}{2}}^{+\infty} dE_{\bar{k}} \int_0^{2\pi} d\phi \, |\mathcal{M}|^2 f_0(\bar{k})(1 \pm f_0(\bar{p}'))(1 \pm f_0(\bar{k}')) \,. \tag{A.4}$$

As alternative parametrization, which can help in the numerical integration and in studying the behavior of the integral, one can define

$$\chi_\pm \equiv q \pm \omega \,, \tag{A.5}$$

in terms of which

$$\int_{-E_{\bar{p}}}^{+\infty} d\omega \int_{|\omega|}^{\omega+2E_{\bar{p}}} dq \int_{\frac{q+\omega}{2}}^{+\infty} dE_{\bar{k}} \quad \to \quad \frac{1}{2} \int_0^{+\infty} d\chi_+ \int_0^{2E_{\bar{p}}} d\chi_- \int_{\chi_+/2}^{\infty} dE_{\bar{k}} \,. \tag{A.6}$$

The $\chi_\pm$ parametrization can be also useful to leave as last integration the one on $E_{\bar{k}}$:

$$\frac{1}{2} \int_0^{+\infty} d\chi_+ \int_0^{2E_{\bar{p}}} d\chi_- \int_{\chi_+/2}^{\infty} dE_{\bar{k}} \quad \to \quad \frac{1}{2} \int_0^{\infty} dE_{\bar{k}} \int_0^{2E_{\bar{k}}} d\chi_+ \int_0^{2E_{\bar{p}}} d\chi_- \,. \tag{A.7}$$

This choice of integration order clearly shows the symmetric role of $E_{\bar{p}}$ and $E_{\bar{k}}$ in the collisional integral.

JHEP03(2022)163

The expressions for the s and u Mandelstam variables as a function of ω, q and $E_{\bar{k}}$ are given by

$$s = -\frac{t}{2q^2}\left\{\left[(2E_{\bar{p}}+\omega)(2E_{\bar{k}}-\omega)+q^2\right]-\cos\phi\sqrt{(4E_{\bar{p}}(E_{\bar{p}}+\omega)+t)(4E_{\bar{k}}(E_{\bar{k}}-\omega)+t)}\right\}, \quad (A.8)$$

$$t = \omega^2-q^2, \quad (A.9)$$

$$u = -t-s, \quad (A.10)$$

while the relative angles between the three-momenta are given in ref. [47] (see appendix A.2, eqs. (A21a)-(A21e)), among which

$$\cos\theta_{pq} = \frac{\omega}{q}+\frac{t}{2E_{\bar{p}}q}\,, \qquad \cos\theta_{kq} = \frac{\omega}{q}-\frac{t}{2E_{\bar{k}}q}\,. \quad (A.11)$$

u-channel parametrization. Analogous formulae can be found for the u-channel parametrization, by exchanging $\bar{\mathbf{p}}'$ and $\bar{\mathbf{k}}'$ in the t-channel parametrization. In this way the integral becomes

$$\mathcal{K} = \frac{1}{8(2\pi)^4E_{\bar{p}}}\int_{-E_{\bar{p}}}^{+\infty}d\omega\int_{|\omega|}^{\omega+2E_{\bar{p}}}dq\int_{\frac{q+\omega}{2}}^{+\infty}dE_{\bar{k}}\int_0^{2\pi}d\phi\,|\mathcal{M}|^2f_0(\bar{k})(1\pm f_0(\bar{p}'))(1\pm f_0(\bar{k}'))\,, \quad (A.12)$$

with $\mathbf{q}\equiv\bar{\mathbf{k}}'-\bar{\mathbf{p}}=\bar{\mathbf{k}}-\bar{\mathbf{p}}'$ and

$$\omega = E_{\bar{k}'}-E_{\bar{p}} = E_{\bar{k}}-E_{\bar{p}'}\,. \quad (A.13)$$

The expressions for the s and u Mandelstam variables are given by

$$s = -\frac{u}{2q^2}\left\{\left[(2E_{\bar{p}}+\omega)(2E_{\bar{k}}-\omega)+q^2\right]-\cos\phi\sqrt{(4E_{\bar{p}}(E_{\bar{p}}+\omega)+u)(4E_{\bar{k}}(E_{\bar{k}}-\omega)+u)}\right\}, \quad (A.14)$$

$$u = \omega^2-q^2, \quad (A.15)$$

$$t = -u-s, \quad (A.16)$$

while

$$\cos\theta_{pq} = \frac{\omega}{q}+\frac{u}{2E_{\bar{p}}q}\,, \qquad \cos\theta_{kq} = \frac{\omega}{q}-\frac{u}{2E_{\bar{k}}q}\,. \quad (A.17)$$

Structure of the contribution. From the above formulae we can easily infer the global structure of the collisional term proportional to $\delta f(p)$. The quantity (we consider the t-channel parametrization for definiteness)

$$\mathcal{K} = \frac{1}{8(2\pi)^4E_{\bar{p}}}\int_{-E_{\bar{p}}}^{+\infty}d\omega\int_{|\omega|}^{\omega+2E_{\bar{p}}}dq\int_{\frac{q+\omega}{2}}^{+\infty}dE_{\bar{k}}\int_0^{2\pi}d\phi\,|\mathcal{M}|^2f_0(\bar{k})(1\pm f_0(\bar{p}'))(1\pm f_0(\bar{k}'))\,, \quad (A.18)$$

only depends on $E_{\bar{p}}$, as we already anticipated. Therefore we get

$$\overline{\mathcal{J}}[\delta f] = -\frac{1}{4N_p}\frac{\delta f(p(\bar{p}))}{\gamma(E_{\bar{p}}+v\bar{p}_z)}\frac{f_0(\bar{p})}{f_0'(\bar{p})}\mathcal{K}[E_{\bar{p}}]\,. \quad (A.19)$$

JHEP03(2022)163

We can now go back to the wall frame, obtaining

$$\mathcal{J}[\delta f] = -\frac{1}{4N_p}\frac{\delta f(p)}{E_p}\frac{f_v(p)}{f'_v(p)}\mathcal{K}[\gamma(E_p - vp_z)] = \frac{1}{4N_p}\frac{\delta f(p)}{E_p}\left(1 \pm e^{-\beta\gamma(E_p - vp_z)}\right)\mathcal{K}[\gamma(E_p - vp_z)]\,. \tag{A.20}$$

Notice that the massless-limit approximation introduced a small 'mismatch' in this expression, since we chose $f_v(p)$ in the prefactors to have the full mass dependence (from the definition of E_p). In the approach to the solution via the use of weights, instead, f_v is treated in the massless limit for all the factors in the collisional integrals. This problem could be solved by also considering the massive form for all the f_v factors inside the collisional integral. This however is computationally more demanding, since it introduces an explicit z dependence in the integrand, so that the kernel should be evaluated also as a function of z.[11]

The numerical analysis shows a behavior

$$\mathcal{K}(E_{\bar{p}}) \sim \log E_{\bar{p}} + \text{const} \tag{A.21}$$

which, as expected, has a logarithmic divergence for mass and thermal mass going to zero. We can thus infer the rough behavior (at least for small v)

$$\mathcal{J}[\delta f] \sim \delta f(p)\frac{\log E_p + \text{const}}{E_p}\,. \tag{A.22}$$

A.2 The terms $\langle \delta f \rangle$

The second ingredient we need in order to compute the collision integrals is the determination of the terms $\langle \delta f \rangle$ in which the perturbation appears under the integral sign. The generic structure of the term that depends on $\delta f(k)$ is

$$\langle \delta f(k) \rangle = \frac{-f_v(p)}{4N_p E_p}\int \frac{d^3\mathbf{k}d^3\mathbf{p}'d^3\mathbf{k}'}{(2\pi)^5 2E_k 2E_{p'} 2E_{k'}}|\mathcal{M}|^2\delta^4(p+k-p'-k')f_v(k)(1\pm f_v(p'))(1\pm f_v(k'))\frac{\delta f(k)}{f'_v(k)}, \tag{A.23}$$

and analogous expressions are valid for the $\delta f(p')$ and $\delta f(k')$ contributions.

The above integral can in principle be evaluated using the same manipulations we described in section A.1. However, the integrand, due to the $\delta f(k)$ factor, is not rotationally invariant, and an additional integration over the direction of $\mathbf{k}$ with respect to the z axis remains. The final result is (also in this section we treat all the particles as massless)

$$\langle \delta f(k) \rangle = -\frac{1}{32N_p}\frac{f_0(p)}{(2\pi)^5 E_p}\mathcal{I}[p_\perp, p_z, z]\,, \tag{A.24}$$

where $\mathcal{I}$, written as a function of the p momentum in the plasma frame, reads

$$\mathcal{I} = \int_{-\bar{E}_p}^{+\infty} d\omega \int_{|\omega|}^{\omega+2E_{\bar{p}}} dq \int_{\frac{q+\omega}{2}}^{+\infty} dE_{\bar{k}} \int_0^{2\pi} d\phi \int_0^{2\pi} d\phi_k |\mathcal{M}|^2 f_0(\bar{k})(1 \pm f_0(\bar{p}'))(1 \pm f_0(\bar{k}'))\frac{\delta f(\bar{k})}{f'_0(\bar{k})}\,, \tag{A.25}$$

[11] Notice that a full treatment would also need a redefinition of the matrix element $|\mathcal{M}|^2$ and of the integration boundaries.

JHEP03(2022)163

in which ϕ_k denotes the angle between the vector $\mathbf{k}$ and the plane where $\mathbf{p}$ and $\hat{z}$, the direction along which the wall moves, lie. The integral $\mathcal{I}$ depends on the three variables $p_\perp$, p_z and z, and requires five numerical integrations. Therefore its evaluation on a fine grid, as required in our numerical approach, is quite cumbersome.

An alternative procedure to manipulate the integral can be used to reduce the number of numerical integrations. This can be done by performing the integration over $\mathbf{p}'$ and $\mathbf{k}'$ in eq. (A.23) and leaving the integral over $\mathbf{k}$ as a last step. In this way the expression for $\langle \delta f(k) \rangle$ can be brought to the form

$$\langle \delta f(k) \rangle = -\frac{f_v(p)}{4N_p E_p} \int \frac{d^3\mathbf{k}}{2E_k} \mathcal{K}_1 \, f_v(k) \frac{\delta f(k)}{f_v'(k)} \,, \tag{A.26}$$

where

$$\mathcal{K}_1 = \frac{1}{(2\pi)^5} \int \frac{d^3\mathbf{k}' \, d^3\mathbf{p}}{2E_{p'} \, 2E_{k'}} |\mathcal{M}|^2 (1 \pm f_v(p'))(1 \pm f_v(k')) \delta^4(p + k - p' - k') \,. \tag{A.27}$$

Since $\mathcal{K}_1$ is a Lorentz scalar, it will be a function of the only Lorentz scalars that can be obtained from the four vectors p^μ, k^μ and the plasma velocity u^μ, namely, $u^\mu p_\mu$, $u^\mu k_\mu$ and $p^\mu k_\mu$. These quantities are related, respectively, to the energies $E_{\bar{p}}$ and $E_{\bar{k}}$ of the incoming particles in the plasma reference frame and to the angle $\theta_{\bar{p}\bar{k}}$ between the momenta $\bar{p}$ and $\bar{k}$. Putting everything together we find

$$\langle \delta f(k) \rangle = -\frac{f_v(p)}{4N_p E_p} \int \frac{d^3\bar{\mathbf{k}}}{2E_{\bar{k}}} \mathcal{K}_1(E_{\bar{p}}, E_{\bar{k}}, \theta_{\bar{p}\bar{k}}) \, f_0(\bar{k}) \frac{\delta f(k_\perp, \gamma(\bar{k}_z + v E_{\bar{k}}), z)}{(-f_0'(\bar{k}))} \,. \tag{A.28}$$

which can be rewritten as

$$\langle \delta f(k) \rangle = -\frac{f_v(p)}{4N_p E_p} \frac{1}{2} \int_0^\infty E_{\bar{k}} dE_{\bar{k}} \int_{-1}^1 d\cos\theta_{\bar{p}\bar{k}} \mathcal{K}_1(E_{\bar{p}}, E_{\bar{k}}, \theta_{\bar{p}\bar{k}}) \int_0^{2\pi} d\phi_{\bar{k}} f_0(\bar{k}) \frac{\delta f(k_\perp, \gamma(\bar{k}_z + v E_{\bar{k}}), z)}{(-f_0'(\bar{k}))} \,. \tag{A.29}$$

The collision integral for the scattering processes includes an additional set contributions in which $\delta f(p')$ or $\delta f(k')$ appears. In analogy to the previous case, for the $\delta f(p')$ terms, we can first perform the integrals over $\mathbf{k}$ and $\mathbf{k}'$, obtaining the following expression

$$\langle \delta f(p') \rangle = \frac{-f_v(p)}{4N_p E_p} \int \frac{d^3\mathbf{p}'}{2E_{p'}} \mathcal{K}_2(E_p, E_{p'}, \theta_{pp'})(1 \pm f_v(p')) \frac{\delta f(p')}{f_v'(p')} \,, \tag{A.30}$$

which can also be rewritten as

$$\begin{aligned} \langle \delta f(p') \rangle = \frac{-f_v(p)}{4N_p E_p} \frac{1}{2} \int_0^\infty E_{\bar{p}'} \, dE_{\bar{p}'} \int_{-1}^1 d\cos\theta_{\bar{p}\bar{p}'} \mathcal{K}_2(E_{\bar{p}}, E_{\bar{p}'}, \theta_{\bar{p}\bar{p}'}) \\ \times \int_0^{2\pi} d\phi_{\bar{p}'} (1 \pm f_0(\bar{p}')) \frac{\delta f(p'_\perp, \gamma(\bar{p}'_z + v E_{\bar{p}'}), z)}{(-f_0'(\bar{p}'))} \,. \end{aligned} \tag{A.31}$$

The contributions from $\delta f(k')$ can be treated in an analogous way.

JHEP03(2022)163

A.2.1 Evaluation of the $\mathcal{K}_1$ kernel

The evaluation of the kernel $\mathcal{K}_1$ can be performed as in ref. [48]. As a first step we boost in the plasma reference frame, and we perform the integration over $\mathbf{k}'$ exploiting the Dirac delta:

$$\mathcal{K}_1 = \frac{1}{(2\pi)^5}\int \frac{d^3\mathbf{p}'}{2E_{p'}}\frac{1}{2E_{k'}}|\mathcal{M}|^2(1\pm f_0(u^\mu p'_\mu))(1\pm f_0(u^\mu k'_\mu))\delta(E_p+E_k-E_{p'}-E_{k'})\,. \quad \text{(A.32)}$$

Notice that in the above expression we expressed the energies $E_{p'}$ and $E_{k'}$ in the Lorentz-invariant form $u^\mu p'_\mu$ and $u^\mu k'_\mu$. As we will see, this is useful to keep track of the changes of reference frame.

As a second step, we boost again in the center of mass frame, where the Dirac delta can be written as

$$\delta(E_p+E_k-E_{p'}-E_{k'}) = \delta(\sqrt{s}-2E_{p'}) = \frac{1}{2}\delta\left(\frac{1}{2}\sqrt{s}-E_{p'}\right)\,, \quad \text{(A.33)}$$

with $s=(p+k)^2$ the usual Mandelstam variable. The integration over $\mathbf{p}'$ can be performed by rewriting $d^3\mathbf{p}' = E_{p'}^2\, dE_{p'}\, d\cos\theta\, d\phi$, where θ is the angle between $\mathbf{p}'$ and $\mathbf{p}$ in the center-of-mass (COM) frame of the scattering process:

$$\mathcal{K}_1 = \frac{1}{(2\pi)^5}\frac{1}{8}\int_{-1}^{1} d\cos\theta \int_0^{2\pi} d\phi |\mathcal{M}|^2(1\pm f_0(u^\mu p'_\mu))(1\pm f_0(u^\mu k'_\mu))\,. \quad \text{(A.34)}$$

As a last step we need to compute $u^\mu p'_\mu$ and $u^\mu k'_\mu$ in the COM frame. We conveniently choose the orientation of the COM frame axes such that $u^y=0$ leading to

$$u^\mu p'_\mu = u^0\frac{\sqrt{s}}{2} - u^x\frac{\sqrt{s}}{2}\sin\theta\cos\phi - u^z\frac{\sqrt{s}}{2}\cos\theta \quad \text{(A.35)}$$

We then introduce the four-vectors P^μ and Q^μ defined as

$$P^\mu = p^\mu + k^\mu\,, \qquad Q^\mu = p^\mu - k^\mu\,. \quad \text{(A.36)}$$

In the COM frame we find that

$$P^\mu = \begin{pmatrix}\sqrt{s}\\ 0\end{pmatrix}\,, \qquad Q^\mu = \begin{pmatrix}0\\ \mathbf{Q}\end{pmatrix}\,. \quad \text{(A.37)}$$

We can get a further simplification by choosing the frame such that $\mathbf{Q}$ lies along the z axis. Since, in the massless case, $|\mathbf{P}|=|\mathbf{Q}|=\sqrt{s}$, the vectors $P^\mu/\sqrt{s}$ and $Q^\mu/\sqrt{s}$ coincide with the versors along the first and fourth Minkowski directions.

The u^0 and u^z components can be easily computed in terms of the momenta of the particles in the plasma frame :

$$u^0 = \frac{u^\mu P_\mu}{\sqrt{s}} = \frac{E_{\bar{p}}+E_{\bar{k}}}{\sqrt{s}} \qquad u^z = -\frac{u^\mu Q_\mu}{\sqrt{s}} = -\frac{(E_{\bar{p}}-E_{\bar{k}})}{\sqrt{s}}\,. \quad \text{(A.38)}$$

JHEP03(2022)163

The u^x component can be determined from the condition $u^\mu u_\mu = 1$:

$$\begin{aligned} u^x &= \sqrt{u_0^2 - u_z^2 - 1} = \frac{1}{\sqrt{s}}\sqrt{(E_{\bar{p}} + E_{\bar{k}})^2 - (E_{\bar{p}} - E_{\bar{k}})^2 - s} \\ &= \frac{1}{\sqrt{s}}\sqrt{4E_{\bar{p}}E_{\bar{k}} - s} = \frac{1}{\sqrt{s}}\sqrt{2E_{\bar{p}}E_{\bar{k}}(1+\cos\theta_{\bar{p}\bar{k}})}\,. \end{aligned} \tag{A.39}$$

Putting everything together we find that $u^\mu p'_\mu$ is given by

$$\begin{aligned} u^\mu p'_\mu &= u^0\frac{\sqrt{s}}{2} - u^x\frac{\sqrt{s}}{2}\sin\theta\cos\phi - u^z\frac{\sqrt{s}}{2}\cos\theta \\ &= \frac{E_{\bar{p}} + E_{\bar{k}}}{2} - \frac{1}{2}\sqrt{2E_{\bar{p}}E_{\bar{k}}(1+\cos\theta_{\bar{p}\bar{k}})}\sin\theta\cos\phi + \frac{(E_{\bar{p}} - E_{\bar{k}})}{2}\cos\theta \\ &= \frac{1}{2}\left(E_{\bar{p}}(1+\cos\theta) + E_{\bar{k}}(1-\cos\theta) - \sqrt{2E_{\bar{p}}E_{\bar{k}}(1+\cos\theta_{\bar{p}\bar{k}})}\sin\theta\cos\phi\right)\,. \end{aligned} \tag{A.40}$$

Similarly we find

$$u^\mu k'_\mu = \frac{1}{2}\left(E_{\bar{p}}(1-\cos\theta) + E_{\bar{k}}(1+\cos\theta) + \sqrt{2E_{\bar{p}}E_{\bar{k}}(1+\cos\theta_{\bar{p}\bar{k}})}\sin\theta\cos\phi\right)\,. \tag{A.41}$$

Finally, the Mandelstam variables are given by

$$t = -\frac{s}{2}(1-\cos\theta) \qquad s = 2E_{\bar{p}}E_{\bar{k}}(1-\cos\theta_{\bar{p}\bar{k}})\,. \tag{A.42}$$

A.2.2 Evaluation of the $\mathcal{K}_2$ kernel

We now discuss the evaluation of the $\mathcal{K}_2$ kernel:

$$\mathcal{K}_2 = \frac{1}{(2\pi)^5}\int \frac{d^3\mathbf{k}\,d^3\mathbf{k}'}{2E_k\,2E_{k'}}|\mathcal{M}|^2 f_0(u^\mu k_\mu)(1 \pm f_0(u^\mu k'_\mu))\delta^4(p+k-p'-k') \tag{A.43}$$

Also in this case we follow ref. [48]. We introduce the four-vectors

$$\begin{aligned} K^\mu &= k^\mu + k'^\mu \\ P^\mu &= p^\mu + p'^\mu \\ Q'^\mu &= k^\mu - k'^\mu \\ Q^\mu &= p^\mu - p'^\mu \end{aligned}\,. \tag{A.44}$$

Recalling that

$$\frac{d^3\mathbf{k}\,d^3\mathbf{k}'}{2E_k\,2E_{k'}} = d^4k\,d^4k'\,\theta(E_k)\theta(E_{k'})\delta(k^2)\delta(k'^2)\,, \tag{A.45}$$

we can use as integration variables K and Q' finding

$$\frac{d^3\mathbf{k}\,d^3\mathbf{k}'}{2E_k\,2E_{k'}} = \frac{1}{4}d^4K\,d^4Q'\,\theta(K_0)\theta(K^2)\delta(K^2+Q'^2)\delta(K^\mu Q'_\mu)\,. \tag{A.46}$$

Since $\delta^4(p+k-p'-k') = \delta^4(Q+Q')$, we can integrate over Q' obtaining

$$\mathcal{K}_2 = \frac{1}{(2\pi)^5}\int \frac{1}{4}d^4K\theta(K_0)\delta(K^2+Q^2)\delta(K^\mu Q_\mu)|\mathcal{M}|^2 f_0(u^\mu k_\mu)(1 \pm f_0(u^\mu k'_\mu)) \tag{A.47}$$

JHEP03(2022)163

In the massless case

$$Q^2 = -P^2 = t\,, \tag{A.48}$$

hence

$$\delta(K^2 + Q^2) = \delta(K^2 + t)\,. \tag{A.49}$$

Using the identity

$$d^4K\,\theta(K^0)\delta(K^2 + t) = \frac{d^3\mathbf{K}}{2\sqrt{\mathbf{K}^2 - t}}\,, \tag{A.50}$$

we can rewrite $\mathcal{K}_2$ as

$$\mathcal{K}_2 = \frac{1}{8(2\pi)^5}\int \frac{d^3\mathbf{K}}{\sqrt{\mathbf{K}^2 - t}}\delta(K^\mu Q_\mu)|\mathcal{M}|^2 f_0(u^\mu k_\mu)(1 \pm f_0(u^\mu k'_\mu))\,. \tag{A.51}$$

We can now rewrite this formula in the COM frame, in which $P^\mu = (\sqrt{-t}, 0, 0, 0)$ and $Q^\mu = (0, 0, 0, \sqrt{-t})$. Introducing polar coordinates for $\mathbf{K}$, with polar angles θ and ϕ, one gets

$$\delta(K^\mu Q'_\mu) = \delta(|\mathbf{K}|\sqrt{-t}\cos\theta) = \frac{1}{|\mathbf{K}|\sqrt{-t}}\delta(\cos\theta)\,, \tag{A.52}$$

which allows to trivially perform the integration over $\cos\theta$, leading to

$$\mathcal{K}_2 = \frac{1}{8(2\pi)^5}\int \frac{|\mathbf{K}|\,d|\mathbf{K}|\,d\phi}{\sqrt{\mathbf{K}^2 - t}\sqrt{-t}}|\mathcal{M}|^2 f_0(u^\mu k_\mu)(1 \pm f_0(u^\mu k'_\mu))\,. \tag{A.53}$$

As a last step, we need to determine the expressions for the u^μ components. Focusing on $u^\mu k_\mu$ we find

$$u^\mu k_\mu = \frac{u^\mu}{2}(K_\mu + Q'_\mu) = \frac{u^\mu}{2}(K_\mu - Q_\mu) = \frac{1}{2}\left(u^0\sqrt{\mathbf{K}^2 - t} - u^x|\mathbf{K}|\cos\phi + u^z\sqrt{-t}\right)\,. \tag{A.54}$$

Where we chose the orientation of the COM frame in such way that $u^y = 0$. In an analogous way we find

$$u^\mu k'_\mu = \frac{u^\mu}{2}(K_\mu - Q'_\mu) = \frac{u^\mu}{2}(K_\mu + Q_\mu) = \frac{1}{2}\left(u^0\sqrt{\mathbf{K}^2 - t} - u^x|\mathbf{K}|\cos\phi - u^z\sqrt{-t}\right)\,. \tag{A.55}$$

Exploiting the fact that $P^\mu/\sqrt{-t}$ and $Q^\mu/\sqrt{-t}$ coincide with the versors in the time and z directions, we can write

$$\begin{aligned} u^0 &= \frac{u^\mu P_\mu}{\sqrt{-t}} = \frac{E_{\bar{p}} + E_{\bar{p}'}}{\sqrt{-t}}\,, \\ u^z &= -\frac{u^\mu Q_\mu}{\sqrt{-t}} = -\frac{E_{\bar{p}} - E_{\bar{p}'}}{\sqrt{-t}}\,. \end{aligned} \tag{A.56}$$

Finally, from $u^\mu u_\mu = 1$, one gets

$$u^x = \sqrt{\frac{(E_{\bar{p}} + E_{\bar{p}'})^2}{-t} - \frac{(E_{\bar{p}} - E_{\bar{p}'})^2}{-t} - 1} = \frac{1}{\sqrt{-t}}\sqrt{2E_{\bar{p}}E_{\bar{p}'}(1 + \cos\theta_{\bar{p}\bar{p}'})}\,. \tag{A.57}$$

JHEP03(2022)163

In order to make the numerical evaluation of the kernel more stable, we used the following coordinate change $|\mathbf{K}| = \sqrt{-t}\tan\theta$, and then we defined $1/\cos\theta = x$. The expression for $\mathcal{K}_2$ becomes

$$\mathcal{K}_2 = \frac{1}{8(2\pi)^5}\int_1^\infty \int_0^{2\pi} dx\, d\phi\, |\mathcal{M}|^2 f_0(u^\mu k_\mu)(1 \pm f_0(u^\mu k'_\mu)) \tag{A.58}$$

with

$$\begin{aligned}
u^\mu k_\mu &= \frac{1}{2}\left((E_{\bar{p}} + E_{\bar{p}'})x - \sqrt{x^2-1}\sqrt{2E_{\bar{p}}E_{\bar{p}'}(1+\cos\theta_{\bar{p}\bar{p}'})}\cos\phi + (E_{\bar{p}} - E_{\bar{p}'})\right)\,, \\
u^\mu k_\mu &= \frac{1}{2}\left((E_{\bar{p}} + E_{\bar{p}'})x - \sqrt{x^2-1}\sqrt{2E_{\bar{p}}E_{\bar{p}'}(1+\cos\theta_{\bar{p}\bar{p}'})}\cos\phi - (E_{\bar{p}} - E_{\bar{p}'})\right)\,, \\
s &= \frac{-t}{2}(x+1)\,, \\
u &= \frac{t}{2}(x-1)\,.
\end{aligned} \tag{A.59}$$

References

[1] C. Caprini et al., *Science with the space-based interferometer eLISA. Part II. Gravitational waves from cosmological phase transitions*, *JCAP* **04** (2016) 001 [arXiv:1512.06239] [INSPIRE].

[2] C. Caprini et al., *Detecting gravitational waves from cosmological phase transitions with LISA: an update*, *JCAP* **03** (2020) 024 [arXiv:1910.13125] [INSPIRE].

[3] S. Kawamura et al., *The Japanese space gravitational wave antenna DECIGO*, *Class. Quant. Grav.* **23** (2006) S125 [INSPIRE].

[4] S. Kawamura et al., *The Japanese space gravitational wave antenna: DECIGO*, *Class. Quant. Grav.* **28** (2011) 094011 [INSPIRE].

[5] W.-R. Hu and Y.-L. Wu, *The Taiji program in space for gravitational wave physics and the nature of gravity*, *Natl. Sci. Rev.* **4** (2017) 685 [INSPIRE].

[6] W.-H. Ruan, Z.-K. Guo, R.-G. Cai and Y.-Z. Zhang, *Taiji program: gravitational-wave sources*, *Int. J. Mod. Phys. A* **35** (2020) 2050075 [arXiv:1807.09495] [INSPIRE].

[7] TianQin collaboration, *TianQin: a space-borne gravitational wave detector*, *Class. Quant. Grav.* **33** (2016) 035010 [arXiv:1512.02076] [INSPIRE].

[8] G.D. Moore and T. Prokopec, *Bubble wall velocity in a first order electroweak phase transition*, *Phys. Rev. Lett.* **75** (1995) 777 [hep-ph/9503296] [INSPIRE].

[9] G.D. Moore and T. Prokopec, *How fast can the wall move? A study of the electroweak phase transition dynamics*, *Phys. Rev. D* **52** (1995) 7182 [hep-ph/9506475] [INSPIRE].

[10] P. John and M.G. Schmidt, *Do stops slow down electroweak bubble walls?*, *Nucl. Phys. B* **598** (2001) 291 [*Erratum ibid.* **648** (2003) 449] [hep-ph/0002050] [INSPIRE].

JHEP03(2022)163

[11] G.D. Moore, *Electroweak bubble wall friction: analytic results*, *JHEP* **03** (2000) 006 [hep-ph/0001274] [INSPIRE].

[12] T. Konstandin, G. Nardini and I. Rues, *From Boltzmann equations to steady wall velocities*, *JCAP* **09** (2014) 028 [arXiv:1407.3132] [INSPIRE].

[13] J. Kozaczuk, *Bubble expansion and the viability of singlet-driven electroweak baryogenesis*, *JHEP* **10** (2015) 135 [arXiv:1506.04741] [INSPIRE].

[14] D. Bödeker and G.D. Moore, *Electroweak bubble wall speed limit*, *JCAP* **05** (2017) 025 [arXiv:1703.08215] [INSPIRE].

[15] J.M. Cline and K. Kainulainen, *Electroweak baryogenesis at high bubble wall velocities*, *Phys. Rev. D* **101** (2020) 063525 [arXiv:2001.00568] [INSPIRE].

[16] B. Laurent and J.M. Cline, *Fluid equations for fast-moving electroweak bubble walls*, *Phys. Rev. D* **102** (2020) 063516 [arXiv:2007.10935] [INSPIRE].

[17] M. Barroso Mancha, T. Prokopec and B. Swiezewska, *Field-theoretic derivation of bubble-wall force*, *JHEP* **01** (2021) 070 [arXiv:2005.10875] [INSPIRE].

[18] S. Höche, J. Kozaczuk, A.J. Long, J. Turner and Y. Wang, *Towards an all-orders calculation of the electroweak bubble wall velocity*, *JCAP* **03** (2021) 009 [arXiv:2007.10343] [INSPIRE].

[19] A. Azatov and M. Vanvlasselaer, *Bubble wall velocity: heavy physics effects*, *JCAP* **01** (2021) 058 [arXiv:2010.02590] [INSPIRE].

[20] S. Balaji, M. Spannowsky and C. Tamarit, *Cosmological bubble friction in local equilibrium*, *JCAP* **03** (2021) 051 [arXiv:2010.08013] [INSPIRE].

[21] R.-G. Cai and S.-J. Wang, *Effective picture of bubble expansion*, *JCAP* **03** (2021) 096 [arXiv:2011.11451] [INSPIRE].

[22] X. Wang, F.P. Huang and X. Zhang, *Bubble wall velocity beyond leading-log approximation in electroweak phase transition*, arXiv:2011.12903 [INSPIRE].

[23] A. Friedlander, I. Banta, J.M. Cline and D. Tucker-Smith, *Wall speed and shape in singlet-assisted strong electroweak phase transitions*, *Phys. Rev. D* **103** (2021) 055020 [arXiv:2009.14295] [INSPIRE].

[24] J.M. Cline, A. Friedlander, D.-M. He, K. Kainulainen, B. Laurent and D. Tucker-Smith, *Baryogenesis and gravity waves from a UV-completed electroweak phase transition*, *Phys. Rev. D* **103** (2021) 123529 [arXiv:2102.12490] [INSPIRE].

[25] J.M. Cline and B. Laurent, *Electroweak baryogenesis from light fermion sources: a critical study*, *Phys. Rev. D* **104** (2021) 083507 [arXiv:2108.04249] [INSPIRE].

[26] F. Bigazzi, A. Caddeo, T. Canneti and A.L. Cotrone, *Bubble wall velocity at strong coupling*, *JHEP* **08** (2021) 090 [arXiv:2104.12817] [INSPIRE].

[27] W.-Y. Ai, B. Garbrecht and C. Tamarit, *Bubble wall velocities in local equilibrium*, *JCAP* **03** (2022) 015 [arXiv:2109.13710] [INSPIRE].

[28] M. Lewicki, M. Merchand and M. Zych, *Electroweak bubble wall expansion: gravitational waves and baryogenesis in Standard Model-like thermal plasma*, *JHEP* **02** (2022) 017 [arXiv:2111.02393] [INSPIRE].

[29] Y. Gouttenoire, R. Jinno and F. Sala, *Friction pressure on relativistic bubble walls*, arXiv:2112.07686 [INSPIRE].

JHEP03(2022)163

[30] G.C. Dorsch, S.J. Huber and T. Konstandin, *On the wall velocity dependence of electroweak baryogenesis*, *JCAP* **08** (2021) 020 [arXiv:2106.06547] [INSPIRE].

[31] G.C. Dorsch, S.J. Huber and T. Konstandin, *A sonic boom in bubble wall friction*, arXiv:2112.12548 [INSPIRE].

[32] A. Megevand and A.D. Sanchez, *Velocity of electroweak bubble walls*, *Nucl. Phys. B* **825** (2010) 151 [arXiv:0908.3663] [INSPIRE].

[33] J.R. Espinosa, T. Konstandin, J.M. No and G. Servant, *Energy budget of cosmological first-order phase transitions*, *JCAP* **06** (2010) 028 [arXiv:1004.4187] [INSPIRE].

[34] L. Leitao and A. Megevand, *Spherical and non-spherical bubbles in cosmological phase transitions*, *Nucl. Phys. B* **844** (2011) 450 [arXiv:1010.2134] [INSPIRE].

[35] A. Mégevand, *Friction forces on phase transition fronts*, *JCAP* **07** (2013) 045 [arXiv:1303.4233] [INSPIRE].

[36] S.J. Huber and M. Sopena, *An efficient approach to electroweak bubble velocities*, arXiv:1302.1044 [INSPIRE].

[37] A. Megevand and F.A. Membiela, *Stability of cosmological deflagration fronts*, *Phys. Rev. D* **89** (2014) 103507 [arXiv:1311.2453] [INSPIRE].

[38] L. Leitao and A. Megevand, *Hydrodynamics of phase transition fronts and the speed of sound in the plasma*, *Nucl. Phys. B* **891** (2015) 159 [arXiv:1410.3875] [INSPIRE].

[39] A. Megevand and F.A. Membiela, *Stability of cosmological detonation fronts*, *Phys. Rev. D* **89** (2014) 103503 [arXiv:1402.5791] [INSPIRE].

[40] A. Megevand, F.A. Membiela and A.D. Sanchez, *Lower bound on the electroweak wall velocity from hydrodynamic instability*, *JCAP* **03** (2015) 051 [arXiv:1412.8064] [INSPIRE].

[41] J.M. Cline, M. Joyce and K. Kainulainen, *Supersymmetric electroweak baryogenesis*, *JHEP* **07** (2000) 018 [hep-ph/0006119] [INSPIRE].

[42] M. Laine, *Bubble growth as a detonation*, *Phys. Rev. D* **49** (1994) 3847 [hep-ph/9309242] [INSPIRE].

[43] J. Ignatius, K. Kajantie, H. Kurki-Suonio and M. Laine, *The growth of bubbles in cosmological phase transitions*, *Phys. Rev. D* **49** (1994) 3854 [astro-ph/9309059] [INSPIRE].

[44] H. Kurki-Suonio and M. Laine, *Supersonic deflagrations in cosmological phase transitions*, *Phys. Rev. D* **51** (1995) 5431 [hep-ph/9501216] [INSPIRE].

[45] Wolfram Research Inc., *Mathematica*, version 13.0.0, https://www.wolfram.com/mathematica/, U.S.A. (2021).

[46] J.M. Cline and K. Kainulainen, *Electroweak baryogenesis at high bubble wall velocities*, *Phys. Rev. D* **101** (2020) 063525 [arXiv:2001.00568] [INSPIRE].

[47] P.B. Arnold, G.D. Moore and L.G. Yaffe, *Transport coefficients in high temperature gauge theories. Part II. Beyond leading log*, *JHEP* **05** (2003) 051 [hep-ph/0302165] [INSPIRE].

[48] S.R. De Groot, W.A. Van Leeuwen and C.G. Van Weert, *Relativistic kinetic theory. Principles and applications*, Elsevier, The Netherlands (1980).

JHEP03(2022)163

Paper 2: Collision integrals for cosmological phase transitions

JHEP

Published for SISSA by Springer

Received: March 20, 2023
Revised: May 3, 2023
Accepted: May 8, 2023
Published: May 25, 2023

Collision integrals for cosmological phase transitions

Stefania De Curtis,[a] **Luigi Delle Rose,**[b] **Andrea Guiggiani,**[a] **Ángel Gil Muyor**[c] **and Giuliano Panico**[a]

[a] *INFN Sezione di Firenze and Dipartimento di Fisica e Astronomia, Università di Firenze, Via G. Sansone 1, I-50019 Sesto Fiorentino, Italy*

[b] *Dipartimento di Fisica, Università della Calabria, I-8703 Arcavacata di Rende, Cosenza, Italy*

[c] *IFAE and BIST, Universitat Autònoma de Barcelona, 08193 Bellaterra, Barcelona, Spain*

E-mail: stefania.decurtis@fi.infn.it, luigi.dellerose@unical.it, andrea.guiggiani@unifi.it, agil@ifae.es, giuliano.panico@unifi.it

Abstract: The dynamics of the true-vacuum bubbles nucleated during a first-order phase transition is affected by the distribution functions of the particle species in the plasma, driven out-of-equilibrium by the travelling domain wall. An accurate modelling of this phenomenon is relevant for a quantitative description of phase transitions in the early universe and for the determination of the corresponding cosmic relics, such as, among the others, the stochastic background of gravitational waves. We address this problem by developing a new spectral method devised for a fast and reliable computation of the collision integral in the Boltzmann equations. In a scalar singlet extension of the Standard Model chosen as a benchmark scenario, we test our algorithm, determining the bubble speed and profile, and we assess the impact of the out-of-equilibrium dynamics.

Keywords: Cosmology of Theories BSM, Early Universe Particle Physics, Phase Transitions in the Early Universe

ArXiv ePrint: 2303.05846

https://doi.org/10.1007/JHEP05(2023)194

JHEP05(2023)194

Contents

JHEP05(2023)194

1 Introduction

First order phase transitions (PhTs) in the early Universe can lead to striking cosmological signatures including, for example, a stochastic background of gravitational waves or a significant departure from equilibrium required by scenarios of electroweak (EW) baryogenesis to generate the observed matter-antimatter asymmetry. Future gravitational wave interferometers, such as LISA [1, 2], DECIGO [3, 4], Taiji [5, 6] and TianQuin [7], have the potential to detect the aforementioned background and thus to shed light on the nature of the EWPhT, providing a new boost in the quest for the physics beyond the Standard Model (BSM).

In order to accurately describe the power spectrum of the gravitational waves and to reconstruct from that the properties of the early Universe at the time of the transition, we need a precise description of the bubble dynamics. Indeed, during a first-order PhT, bubbles of the stable phase nucleate and expand through space interacting with the surrounding plasma. One of the most relevant parameters describing this dynamics is the speed of the domain wall (DW) in the steady state regime. This affects both the magnitude and the shape of the gravitational wave spectrum and, most probably, it will be the parameter determined with the best accuracy by the future generation of interferometers [8].

The first computation of the bubble speed dates back to refs. [9–14]. In those works the friction exerted on the DW by the particles of the plasma was computed from their out-of-equilibrium distribution functions, which are obtained, in turn, as solutions to the corresponding Boltzmann equations. These results were fed to the equation of motion of the DW which was then used to extract the bubble speed and the bubble width.

The challenging part of the computation resides in the Boltzmann equation and, in particular, in the collision integral that describes the interactions among the particles in the plasma. This term represents the bottleneck of these kind of computations since it makes the Boltzmann equation a complicated integro-differential problem. The strategy exploited in ref. [14] to address this issue was based on the fluid approximation which corresponds to a first order momentum expansion of the out-of-equilibrium distributions. Within this approach, these are parametrized by three space-dependent perturbations: the chemical potential, the temperature and the velocity fluctuations. By taking moments of the Boltzmann equation with suitably chosen weight factors, the fluid approximation allows one to turn the integro-differential equation into a simpler system of ordinary differential equations.

Since this formalism strongly relies on the choice of the weight basis and on a specific ansatz for the momentum dependence of the distribution functions, it is intrinsically affected by some degree of arbitrariness. Moreover, a first order truncation may not be sufficient to capture all the relevant features of the out-of-equilibrium distributions. Indeed, subsequent works [15–17] have shown that the fluid approximation is not particularly reliable, neither quantitatively nor qualitatively.

With the successes of precision cosmology and the new opportunities offered by the gravitational wave interferometry, the necessity of a solid description of the bubble dynamics in a first order PhT is more than pressing. In this respect, a huge effort has been done recently to conceive more reliable approximation methods and to develop a deeper theoretical understanding. Several attempts have been carried out to ameliorate the existing results. For instance, the fluid approximation has been extended in refs. [16, 18] with the inclusion of higher orders in the small momentum expansion; a less constrained momentum dependence has been exploited in refs. [15, 19] by using a factorization ansatz. In ref. [20] an improved and faster algorithm has been proposed which exploits a decomposition of the out-of-equilibrium distributions on a basis of Chebyshev polynomials.
For the sake of completeness, we also mention that other approaches, based on phenomenological modelling of the friction through a viscosity parameter, have also been explored [21–29].

In refs. [17, 30, 31] we made a step forward in the development of an accurate method to determine the out-of-equilibrium distributions without imposing any specific momentum dependence. We presented, for the first time, a fully quantitative solution to the Boltzmann equation designed to compute the collision integrals through an iterative algorithm without the use of any ansatz. This methodology can be applied to evaluate the friction on the bubble wall and the terminal speed of the latter, but it can be used also to describe the non-equilibrium properties of the distribution functions that are relevant for the determination of the matter-antimatter asymmetry in models of baryogenesis. The algorithm discussed in ref. [17] allows one to compute the deviations from equilibrium of the particles in the plasma, as function of their momenta, induced by the presence of a travelling DW. The system is mainly characterized by the bubble speed v_w, the wall width L_w and the non-zero vacuum expectation value v of the scalar driving the PhT. These parameters are taken as input of the iterative procedure.

JHEP05(2023)194

While the proposed algorithm for the solution of the Boltzmann equation can reach convergence within a small number of steps, it can quickly become computationally expensive when it is embedded in the full algorithm that scans over the space of v_w, L_w and v. This algorithm is used to identify the values of the parameters that simultaneously solve the Boltzmann equation and the equation of motion of the DW. The procedure would be even more time-demanding if one explores the parameter space of new physics models in the search for optimal points providing observable signals of gravitational waves as well as, for instance, the correct amount of the baryon asymmetry.

Analogously to previous works, the bottleneck of our iterative algorithm is the computation of the collision integral. Although some algebraic manipulations were used to reduce the dimensionality of the integral, the large number of integrations, together with the singular behavior of the integration kernels, strongly limited the computational speed, even on a cluster. In the present work we significantly improve on our previous results by providing a more efficient method for the computation of the collision integral. We exploit a spectral decomposition of the collision operator in terms of its eigenfunctions, effectively reducing a complex and time-consuming nine-dimensional integration in a much faster matrix multiplication. Moreover, the eigenfunctions are computed only once and can be reused during all the scanning procedure of an entire model.

For the purpose of presenting our new methodology, we consider the case of a first order EWPhT driven by two scalar fields. This scenario can be realized by enlarging the SM particle spectrum with a singlet scalar field coupled to the SM sector only through a quartic portal interaction. For the computation of the friction we focus on the contribution of the top quark species which has the largest coupling, among all the SM particles, to the Higgs field. All the other particles are assumed to be in local equilibrium and considered as background. The inclusion of the out-of-equilibrium distributions of other species in the computation of the friction, such as the massive EW gauge bosons, is straightforward and it will be addressed in a future work.

The paper is organized as follows. In section 2 we review the Boltzmann equation and we introduce the necessary notation while in section 3 we present the new spectral decomposition method. In section 4 we discuss the hydrodynamic equations for the temperature and velocity profiles and in section 5 we discuss the numerical results. The conclusions are drawn in section 6. Appendix A summarizes some technical details on the solutions to the hydrodynamic equations.

2 The Boltzmann equation

Our main goal is to compute the terminal velocity of the DW that surrounds the true-vacuum bubbles. This parameter is the result of a balance of the internal pressure, proportional to the potential energy difference between the two vacua, and the friction provided by particles in the plasma impinging on the DW. Usually, for the computation of the terminal velocity the relevant configurations are those in which the radius of the wall is much larger than its thickness. In such a case, as we will do in the following, we can adopt the

JHEP05(2023)194

planar limit, orient the z-axis along the propagating direction of the DW and assume that a steady state is reached.

The friction acting on the bubble wall is determined by the deviations of the distribution function from equilibrium, δf, and in the steady state and planar limit it is given by

$$F(z) = \sum_i \frac{N_i}{2} \frac{dm_i^2}{dz} \int \frac{d^3\mathbf{p}}{(2\pi)^3 E_p} \delta f_i \,, \tag{2.1}$$

where the sum runs over all the particle species in the plasma, m_i is the mass of the i-th particle, N_i its degrees of freedom and δf_i the corresponding perturbation.

The perturbations around equilibrium are computed by solving the Boltzmann equation for the distribution function of the plasma in the presence of an expanding bubble of true vacuum. It is convenient to write the Boltzmann equation in the wall reference frame, where the solution is stationary. The equation for the distribution function f of a particle species in the plasma is

$$\mathcal{L}[f] \equiv \left(\frac{p_z}{E} \partial_z - \frac{(m^2(z))'}{2E} \partial_{p_z} \right) f = -\mathcal{C}[f] \,, \tag{2.2}$$

where $\mathcal{L}$ is the Liouville operator, $\mathcal{C}$ is the collision operator, $m(z)$ is the mass of the particle and its derivative is performed along the z direction. As we mentioned before, in this work we consider the top quark to be the only species out-of-equilibrium, since it is the one with the strongest interaction with the Higgs field. We assume that the light degrees of freedom of the plasma, namely all the SM degrees of freedom but the top, are in local equilibrium and we treat them as background fluids described by the standard Fermi-Dirac or Bose-Einstein distributions.

For a perfect fluid, in the wall reference frame the distribution function is

$$f_v = \frac{1}{e^{\beta(z)\gamma_p(z)(E - v_p(z)p_z)} \pm 1} \,, \tag{2.3}$$

where $\beta = T^{-1}$, γ_p is the Lorentz gamma factor, and $v_p(z)$ is the velocity profile of the plasma measured in the wall reference frame. In local equilibrium, macroscopic quantities in general depend on the position z.

Since we consider small perturbations around equilibrium, we can linearize the Boltzmann equation in δf, namely $f = f_v + \delta f$. As we showed in ref. [17] the linearized Boltzmann equation can be cast in the general form

$$\mathcal{L}[\delta f] - \frac{\mathcal{Q}}{E} \delta f = \frac{p_z}{E} \mathcal{S} + \langle \delta f \rangle \,, \tag{2.4}$$

where the source term $\mathcal{S}$ originates from the action of the Liouville operator on f_v, while the bracket $\langle \delta f \rangle$ and $\mathcal{Q}$ arise from the linearized collision operator.

By considering $2 \leftrightarrow 2$ scattering processes, the collision operator takes the following form

$$\mathcal{C}[f] = \sum_i \frac{1}{4 N_p E} \int \frac{d^3\mathbf{k} d^3\mathbf{p}' d^3\mathbf{k}'}{(2\pi)^5 2E_k 2E_{p'} 2E_{k'}} |\mathcal{M}_i|^2 \delta^4(p + k - p' - k') \mathcal{P}[f] \,, \tag{2.5}$$

JHEP05(2023)194

with the sum performed over all the relevant processes with amplitude $\mathcal{M}_i$ and the population factor is given by

$$\mathcal{P}[f] = f(p)f(k)(1 \pm f(p'))(1 \pm f(k')) - f(p')f(k')(1 \pm f(p))(1 \pm f(k))\,. \tag{2.6}$$

In eq. (2.5), N_p represents the degrees of freedom of the incoming particle with momentum p, k is the momentum of the second incoming particle, while p' and k' are the momenta of the particles in the final state. The $+$ sign is for bosons, while the $-$ sign is for fermions. After the linearization in δf the collision operator is given by

$$\bar{\mathcal{C}}[f] \equiv -\frac{\mathcal{Q}}{E}\frac{f_v}{f'_v}\delta f(p) - \langle \delta f \rangle = \sum_i \frac{1}{4N_p E}\int \frac{d^3\mathbf{k}d^3\mathbf{p}'d^3\mathbf{k}'}{(2\pi)^5 2E_k 2E_{p'} 2E_{k'}}|\mathcal{M}_i|^2\delta^4(p+k-p'-k')\bar{\mathcal{P}}[f]\,, \tag{2.7}$$

with

$$\bar{\mathcal{P}}[f] = f_v(p)f_v(k)(1 \pm f_v(p'))(1 \pm f_v(k'))\sum \mp \frac{\delta f}{f'_v}\,, \tag{2.8}$$

where the $\mp$ in the sum is for incoming and outgoing particles, respectively. As done in ref. [17], we can distinguish two contributions coming from the linearized collision operator: the first one, which depends only on $\delta f(p)$ so that the perturbation factorizes out of the integral, is described by the term $\mathcal{Q}/E\,\delta f$ in eq. (2.4); the second one, denoted by the bracket $\langle \delta f \rangle$, includes the contributions where δf appears under the integral sign.

3 Spectral decomposition of the collision operator

The most computationally cumbersome term in the Boltzmann equation is the bracket $\langle \delta f \rangle$, which corresponds to a nine dimensional integral involving the unknown δf. One possible strategy to deal with this term is to perform, first, all the integrations that do not involve the unknown perturbation δf, as explained in ref. [32]. The main advantage of this method is that such integrals depend only on the processes under consideration and have to be computed only once.

Applying such procedure and assuming the particles to be massless inside the collision integral, the bracket term takes the following form [17]

$$\begin{aligned}\langle \delta f \rangle = -\frac{f_v(p)}{E_p}\Bigg(\int \frac{d^3\bar{\mathbf{k}}}{|\bar{\mathbf{k}}|}\Big[& f_0(\beta(z)|\bar{\mathbf{k}}|)\,\mathcal{K}_a(\beta(z)|\bar{\mathbf{p}}|, \beta(z)|\bar{\mathbf{k}}|, \theta_{\bar{p}\bar{k}}) \\ & - (1 - f_0(\beta(z)|\bar{\mathbf{k}}|))\,\mathcal{K}_s(\beta(z)|\bar{\mathbf{p}}|, \beta(z)|\bar{\mathbf{k}}|, \theta_{\bar{p}\bar{k}})\Big]\frac{\delta f(k_\perp, k_z, z)}{f'_0(\beta(z)|\bar{\mathbf{k}}|)}\Bigg)\,,\end{aligned} \tag{3.1}$$

where barred momenta are computed in the local plasma reference frame, f_0 denotes the standard (Fermi-Dirac or Bose-Einstein) distribution functions, and $\theta_{\bar{p}\bar{k}}$ is the relative angle in the local plasma reference frame between the particles with momentum p and k. The momenta $k_\perp$ and k_z, defined in the wall reference frame, can be expressed as functions of the local plasma momenta through a boost along the z-axis, namely $k_z = \gamma_p(z)(E_{\bar{k}} + v_p(z)\bar{k}_z)$,

JHEP05(2023)194

process	$\lvert\mathcal{M}\rvert^2$
$t\bar{t} \to gg$	$\frac{128}{3} g_s^4 \left[\frac{ut}{(t-m_q^2)^2} + \frac{ut}{(u-m_q^2)^2} \right]$
$tg \to tg$	$-\frac{128}{3} g_s^4 \frac{su}{(u-m_q^2)^2} + 96 g_s^4 \frac{s^2+u^2}{(t-m_g^2)^2}$
$tq \to tq$	$160 g_s^4 \frac{s^2+u^2}{(t-m_g^2)^2}$

Table 1. Amplitudes for the scattering processes relevant for the top quark in the leading log approximation [17]. In the $tq \to tq$ process we summed over all massless quarks and antiquarks.

$k_\perp = \bar{k}_\perp$. The functions $\mathcal{K}_a$ and $\mathcal{K}_s$ are the annihilation and scattering kernels (we refer to ref. [17] for the details)

$$\begin{aligned} \mathcal{K}_a &= \frac{1}{8N_p(2\pi)^5} \int \frac{d^3\mathbf{k}' d^3\mathbf{p}'}{2E_{p'} 2E_{k'}} |\mathcal{M}_a|^2 (1 \pm f_v(p'))(1 \pm f_v(k'))\delta^4(p+k-p'-k') \\ \mathcal{K}_s &= \frac{1}{8N_p(2\pi)^5} \int \frac{d^3\mathbf{k} d^3\mathbf{k}'}{2E_k 2E_{k'}} |\mathcal{M}_s|^2 f_v(k)(1 \pm f_v(k'))\delta^4(p+k-p'-k') \end{aligned} \tag{3.2}$$

where the matrix elements are reported in table 1.

For a planar wall, the perturbation δf depends only on the components of the momentum, k_z and $k_\perp$, parallel and perpendicular to the propagating direction of the DW. As a consequence, eq. (3.1) can be further simplified exploiting the fact that the perturbation δf is invariant under rotations around the z axis. Using spherical coordinates $\{|\bar{\mathbf{k}}|, \theta_{\bar{k}}, \phi_{\bar{k}}\}$, where $\theta_{\bar{k}}$ is the polar angle between $\bar{\mathbf{k}}$ and the z direction computed in the local plasma reference frame, it is possible to perform the integration over the azimuthal angle $\phi_{\bar{k}}$ because δf does not depend on it. By also using the property

$$(1 \pm f_0(p)) = e^p f_0(p)\,, \tag{3.3}$$

we obtain

$$\langle \delta f \rangle = -\frac{f_v(p)}{E_p} \int |\bar{\mathbf{k}}| d|\bar{\mathbf{k}}| d\cos\theta_{\bar{k}} f_0(\beta(z)|\bar{\mathbf{k}}|) \widetilde{\mathcal{K}}(\beta(z)|\bar{\mathbf{p}}|, \cos\theta_{\bar{p}}, \beta(z)|\bar{\mathbf{k}}|, \cos\theta_{\bar{k}}) \frac{\delta f(k_\perp, k_z, z)}{f_0'(\beta(z)|\bar{\mathbf{k}}|)}\,, \tag{3.4}$$

where $\widetilde{\mathcal{K}}$ is the result of the integration of the kernels over the azimuthal angle.

Since the z dependence in the kernel comes only from the temperature profile, i.e. from the $\beta(z)$ factors, we can obtain a position independent expression through the local change of variables

$$\beta(z)k \to k \qquad \beta(z)p \to p\,. \tag{3.5}$$

In this way, the z dependence inside the integral is encapsulated only in the perturbation δf and we finally arrive to

$$\begin{aligned} \langle \delta f \rangle &= -\frac{f_v(p/\beta(z))}{\beta(z)E_p} \int |\bar{\mathbf{k}}| d|\bar{\mathbf{k}}| d\cos\theta_{\bar{k}} f_0(|\bar{\mathbf{k}}|) \widetilde{\mathcal{K}}(|\bar{\mathbf{p}}|, \cos\theta_{\bar{p}}, |\bar{\mathbf{k}}|, \cos\theta_{\bar{k}}) \frac{\delta f(k_\perp/\beta(z), k_z/\beta(z), z)}{f_0'(|\bar{\mathbf{k}}|)} \\ &\equiv -\frac{f_v(p/\beta(z))}{\beta(z)E_p} \int \mathcal{D}\bar{k}\, \widetilde{\mathcal{K}}_{\bar{p},\bar{k}} \frac{\delta f(k_\perp/\beta(z), k_z/\beta(z), z)}{f_0'(|\bar{\mathbf{k}}|)}\,, \end{aligned} \tag{3.6}$$

JHEP05(2023)194

where we introduced the notation $\mathcal{D}\bar{k} \equiv f_0(|\bar{\mathbf{k}}|)|\bar{\mathbf{k}}|d|\bar{\mathbf{k}}|d\cos\theta_{\bar{k}}$ and $\widetilde{\mathcal{K}}_{\bar{p},\bar{k}} \equiv \widetilde{\mathcal{K}}(|\bar{\mathbf{p}}|, \cos\theta_{\bar{p}}, |\bar{\mathbf{k}}|, \cos\theta_{\bar{k}})$.

The $\langle \delta f \rangle$ term can be reinterpreted as the action of a Hermitian operator on the perturbation. For this purpose we define the operator

$$\mathcal{O}[g] \equiv \int \mathcal{D}\bar{k}\, \widetilde{\mathcal{K}}_{\bar{p},\bar{k}}\, g(|\bar{\mathbf{k}}|, \cos\theta_{\bar{k}})\,. \tag{3.7}$$

Due to particle exchange symmetry, the kernel function $\widetilde{\mathcal{K}}$ is symmetric under the exchange $p \leftrightarrow k$, namely $\widetilde{\mathcal{K}}_{\bar{p},\bar{k}} = \widetilde{\mathcal{K}}_{\bar{k},\bar{p}}$. As a consequence, the operator $\mathcal{O}$ is Hermitian with respect to the scalar product

$$(f, g) = \int \mathcal{D}\bar{k}\, f(|\bar{\mathbf{k}}|, \cos\theta_{\bar{k}})\, g(|\bar{\mathbf{k}}|, \cos\theta_{\bar{k}})\,. \tag{3.8}$$

This conclusion is clearly also valid for other choices of the scalar product. The one we use, as we will see in the following, is motivated by the fact that it significantly simplifies the evaluation of the collision integral.

Thanks to its Hermiticity, the operator $\mathcal{O}$ can be diagonalized with an orthonormal basis of eigenfunctions

$$\mathcal{O}[\psi_l] = \int \mathcal{D}\bar{k}\, \widetilde{\mathcal{K}}_{\bar{p},\bar{k}}\, \psi_l(|\bar{\mathbf{k}}|, \cos\theta_{\bar{k}}) = \lambda_l\, \psi_l(|\bar{\mathbf{k}}|, \cos\theta_{\bar{k}})\,, \tag{3.9}$$

and the kernel $\widetilde{\mathcal{K}}$ can be rewritten as [33]

$$\widetilde{\mathcal{K}}_{\bar{p},\bar{k}} = \sum_l \lambda_l\, \psi_l(|\bar{\mathbf{p}}|, \cos\theta_{\bar{p}})\, \psi_l(|\bar{\mathbf{k}}|, \cos\theta_{\bar{k}})\,. \tag{3.10}$$

Using this decomposition we can drastically simplify the computation of the bracket $\langle \delta f \rangle$. Indeed, once the eigenvectors are determined, the remaining two integrals involved in the computation become trivial due to the orthogonality property. The final expression for the bracket is then

$$\langle \delta f \rangle = -\frac{f_v(p/\beta(z))}{\beta(z) E_p} \sum_l \lambda_l\, \phi_l(z)\, \psi_l(|\bar{\mathbf{p}}|, \cos\theta_{\bar{p}}), \tag{3.11}$$

where $\phi_l(z)$ is the projection of the perturbation on the eigenstate basis, namely

$$\phi_l(z) = \int \mathcal{D}\bar{k}\, \psi_l(|\bar{\mathbf{k}}|, \cos\theta_{\bar{k}}) \frac{\delta f(k_\perp/\beta(z), k_z/\beta(z), z)}{f_0'(|\bar{\mathbf{k}}|)}\,. \tag{3.12}$$

As we will see in the next section, the main advantage of this decomposition method is the huge improvement in the timing performances in the computation of the bracket term.

3.1 Numerical implementation

To implement numerically the spectral decomposition of the kernel, we need to choose a suitable basis of functions on which the perturbations can be expanded. A simple choice, which we use for our numerical analysis, is to discretize the $\{|\bar{\mathbf{p}}|, \cos\theta_{\bar{p}}\}$ space on a regular

JHEP05(2023)194

finite lattice. The functional space is then obtained from the discretized version through a suitable interpolation.

Using a rectangular lattice with M and N points in the $|\bar{\mathbf{p}}|$ and $\cos\theta_{\bar{p}}$ directions respectively, the operator $\mathcal{O}$ is represented by an $(MN) \times (MN)$ Hermitian matrix $\mathcal{U}$, which can be diagonalized to obtain the spectral decomposition. We computed the matrix elements of $\mathcal{U}$ on an orthonormal basis of functions $\{e_{mn}\}$ that vanish everywhere on the grid but on the point $(|\bar{\mathbf{p}}|_m, \cos\theta_{\bar{p}_n})$.

Some subtleties must be taken into account in the discretization process. The measure we adopted for the scalar product, $\mathcal{D}\bar{k}$, contains a factor $|\bar{\mathbf{k}}|$, which vanishes for $|\bar{\mathbf{k}}| = 0$. This means that if a zeroth-order (i.e. a piecewise constant) approximation of the basis functions and of the integration measure is used, the elements e_{mn} corresponding to $|\bar{\mathbf{p}}|_m = 0$ become singular. This is not a significant problem, since also the kernel $\widetilde{\mathcal{K}}_{\bar{p},\bar{k}}$ vanishes for $|\bar{\mathbf{p}}| = 0$ or $|\bar{\mathbf{k}}| = 0$. Therefore the singular basis functions can be neglected in the spectral decomposition of the kernel and in the computation of the collision integral.

One of the non-trivial features of the kernel, which is hard to reproduce, is the presence of a peak located at $|\bar{\mathbf{p}}| = |\bar{\mathbf{k}}|$ and $\cos\theta_{\bar{p}} = \cos\theta_{\bar{k}}$, whose height diverges for $\cos\theta_{\bar{p}} = \cos\theta_{\bar{k}} = \pm 1$. Such a peak originates from the forward scattering of the incoming particles. We regularized such behaviour by setting an upper cut on the value of the kernel in $\cos\theta_{\bar{p},\bar{k}} = \pm 1$. We checked that this approximation improves the numerical stability of the computation and has a negligible impact on the final result.

In our implementation we used a linearly-increasing spacing (i.e. a quadratic distribution) for the points along the $|\bar{\mathbf{p}}|$ direction and a uniform spacing for the points along $\cos\theta_{\bar{p}}$. The non-uniform spacing in the momentum direction is motivated by the fact that it allows us to obtain a finer spacing at small momentum, where the kernel structure shows more complex features. This choice also helps in obtaining a more uniform reconstruction of the peak structure, whose width scales as $|\bar{\mathbf{p}}|$.

For our numerical analysis we chose a grid with $M = 100$ (with the restriction $|\bar{\mathbf{p}}|/T \leq 20$) and $N = 51$ points, and we excluded the points with $|\bar{p}| = 0$. In this way the $\mathcal{U}$ matrix has dimension 5100. We show in figure 1 the relative size of the kernel eigenvalues in decreasing absolute value. The plot shows that, after a relatively fast decrease, the size of the eigenvalues tends to decrease slowly, so that a large fraction of them has a size $\gtrsim 10^{-4}|\lambda_0|$. As a consequence, in order to reconstruct the kernel with an overall accuracy of order $1 - 2\%$, almost all eigenvectors must be taken into account. Including in the sum only the largest 4000 eigenvalues, the typical reconstruction error is $2 - 5\%$, while with 3000 eigenvalues it grows to $5 - 10\%$.

We mention that significantly larger relative reconstruction errors are present in regions where the kernel is highly suppressed (such as for configurations in which p is small while k is large, or vice versa), or, especially for large momenta, around the peak. These regions, however have a limited impact on the computation of the collision integral, as confirmed by the numerical analysis reported in section 5.

By adopting the basis of eigenfunctions $\{\psi_l\}$ to decompose the perturbation, the computational time of the brackets is highly reduced. Compared to the timing performance of the method presented in ref. [17] the decomposition method outlined in this section is two

JHEP05(2023)194

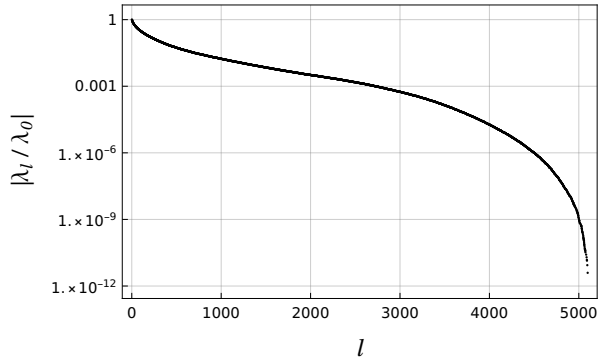

Figure 1. Relative size of the eigenvalues of the kernel matrix $\mathcal{U}$ with $M = 100$ and $N = 51$. A large fraction of them (the first ~ 3500 eigenvalues) has a size $\gtrsim 10^{-4}|\lambda_0|$.

orders of magnitude faster. Such numerical improvement allows one to solve the Boltzmann equation in less than one hour on a desktop computer.

We finally mention a possible improvement of the decomposition method. Due to rotational invariance of the kernel, the operator $\mathcal{O}$ is diagonal in the basis of the Legendre polynomials $P_l(\cos\theta_{\bar{p}})$. Using such basis, one could, in principle, reduce the number of eigenvectors needed to get a good reconstruction of the kernel and, at the same time, increase the numerical stability. Although in the present work we used the basis $\{\psi_l\}$, we numerically check these eigenfunctions are indeed proportional to the Legendre polynomials.[1]

4 Hydrodynamic equations for the background

In this section we focus on the characterization of the plasma that interacts with the DW. As we stated before, we consider the plasma to be a mixture of two different fluids: the top quark fluid, and the massless background, which contains all the species with negligible couplings to the DW. The out-of-equilibrium deviations of the latter are suppressed by the large number of degrees of freedom and can be neglected in a first approximation. In ref. [17] we regarded the background as a thermal bath with temperature and velocity that do not depend on the position. In the present work we relax this approximation and we consider the massless species to be only in local equilibrium. In such a case, the background plasma is described by equilibrium distribution functions with position-dependent temperature and velocity.

The simplest approach to determine the temperature and velocity profiles for the plasma relies on a linearization procedure but it has the major drawback to break down for $v_w = c_s$, where c_s is the speed of sound in the plasma [14, 18]. To fully take into account the non-linearities and thus to avoid the singularity at c_s, one can exploit a set of hydrodynamic equations [20] that are obtained from the conservation of the energy-momentum tensor of the system. We will briefly summarize this approach in the following.

[1] Small numerical discrepancies for $l > 5$ are present in the regions where $\cos\theta_{\bar{p},\bar{k}} = \pm 1$. These are clearly due to the cut that we introduced to regularize the corresponding regions.

JHEP05(2023)194

The energy-momentum tensor can be conveniently split into three components: the one due to the scalar fields ϕ_i participating in the PhT ($T^{\mu\nu}_{\phi}$), the local-equilibrium contributions of all the species in the plasma ($T^{\mu\nu}_{pl}$), and the out-of-equilibrium deviations of the massive species ($T^{\mu\nu}_{\text{out}}$), namely

$$T^{\mu\nu} = T^{\mu\nu}_{\phi} + T^{\mu\nu}_{pl} + T^{\mu\nu}_{\text{out}} \,. \tag{4.1}$$

In the reference frame of the DW, the conservation of the energy-momentum tensor leads to the following equations

$$\begin{aligned} T^{30} &= w(\phi_i, T)\gamma_p^2 v_p + T^{30}_{\text{out}} = c_1 \,, \\ T^{33} &= \frac{1}{2}(\partial_z \phi_i)^2 - V(\phi_i, T) + w\gamma_p^2 v_p^2 + T^{33}_{\text{out}} = c_2 \,, \end{aligned} \tag{4.2}$$

where $V(\phi_i, T)$ is the finite-temperature effective potential, while $w(\phi_i, T)$ is the enthalpy defined as

$$w(\phi_i, T) = T\frac{\partial V(\phi_i, T)}{\partial T} \,. \tag{4.3}$$

The two constants c_1 and c_2 can be determined from the boundary values of v_p and T far in front or far behind the DW.

Equations (4.2) can be recast in the following form

$$\begin{aligned} v_p &= \frac{-w(\phi_i, T) + \sqrt{4(c_1 - T^{30}_{\text{out}})^2 + w^2}}{2(c_1 - T^{30}_{\text{out}})} \,, \\ &\frac{1}{2}(\partial_z \phi_i)^2 - V(\phi_i, T) - \frac{1}{2}w(\phi_i, T) + \frac{1}{2}\sqrt{4(c_1 - T^{30}_{\text{out}})^2 + w(\phi_i, T)^2} - (c_2 - T^{33}_{\text{out}}) = 0 \,, \end{aligned} \tag{4.4}$$

and their solutions yield the velocity and temperature profiles. These equations can be straightforwardly solved with a simple root-finding numerical algorithm.

Finally, the boundary values of the temperature, the plasma velocity and the field VEVs far in front and far behind the DW, which we denote with a $+$ and $-$ subscript respectively, can be determined as described in ref. [22]. The fields VEVs can be easily found by minimizing the potential, namely,

$$\frac{\partial V(\phi_{i\pm}, T_{\pm})}{\partial \phi_i} = 0 \,, \tag{4.5}$$

while the computation of $T_{\pm}$ and $v_{p\pm}$, that depend on the DW velocity v_w, is much more involved and is briefly outlined in the appendix (we refer to refs. [20, 22] for further details).

5 Numerical analysis

To validate the method described in section 3 we compared it with the one we developed in our previous work [17]. In particular we compared the relevant quantities that enter in the computation of the DW terminal speed, namely the out-of-equilibrium corrections to the stress-energy tensor T^{30}_{out}, T^{33}_{out}, and the friction $F(z)$.

We choose as a benchmark scenario the Z_2-symmetric singlet extension of the SM. This choice is motivated by the fact that the presence of a new scalar field s affects the

JHEP05(2023)194

thermal history of the Universe and can give rise to a first-order EWPhT. The extra scalar, singlet under the SM gauge group, also allows for a two-step PhT, in which case the EW symmetry breaking is preceded by a Z_2-symmetry breaking in the extra sector (see for instance refs. [34, 35] and references therein).

The tree-level potential of the model is

$$V_{\text{tree}}(h,s) = \frac{\lambda_h}{4}\left(h^2 - v_0^2\right)^2 + \frac{\lambda_s}{4}\left(s^2 - w_0^2\right)^2 + \frac{\lambda_{hs}}{4}h^2 s^2\,, \tag{5.1}$$

where v_0 is the Higgs VEV at the EW minimum, λ_h is the Higgs self coupling while λ_s, w_0 and λ_{hs} describe the singlet self-coupling, its VEV when the EW symmetry is exact and the portal coupling with the Higgs, respectively. The parameter w_0 can be traded for the physical mass of the singlet using the relation

$$m_s^2 = -\lambda_s w_0^2 + \frac{1}{2}\lambda_{hs} v_0^2\,. \tag{5.2}$$

The finite-temperature effective potential of the model takes into account, besides the tree-level term, the one-loop corrections at zero temperature V_1, the counterterms that regularize the UV divergences V_{CT} (we adopted the $\overline{\text{MS}}$ renormalization scheme) and the thermal corrections V_T (see ref. [36] for the details):

$$V(h,s,T) = V_{\text{tree}}(h,s) + V_1(h,s) + V_{CT}(h,s) + V_T(h,s,T)\,. \tag{5.3}$$

Once the model parameters are chosen, the temperature and velocity profiles of the background plasma are computed by using the conservation laws of the stress-energy tensor. In addition, by solving the coupled system of the Boltzmann equation and the equations of motion of the scalar fields, one can determine the terminal speed of the DW.

In figure 2 we plot $F(z)$, $T^{33}_{\text{out}}(z)$, $T^{30}_{\text{out}}(z)$ as functions of the ratio z/L_h, for two benchmark points reported in table 2 and characterized by $v_w = 0.388$, $L_h T_n = 9.69$, $h_-/T_n = 1.16$ for the benchmark BP1 and by $v_w = 0.473$, $L_h T_n = 5.15$, $h_-/T_n = 2.25$ for BP2. As we will see in the following section, such values correspond to the terminal ones obtained for a scalar potential with parameters $m_s = 103.8\,\text{GeV}$, $\lambda_{hs} = 0.72$ and $\lambda_s = 1$ for BP1 and $m_s = 80.0\,\text{GeV}$, $\lambda_{hs} = 0.76$ and $\lambda_s = 1$ for BP2. The plots clearly show that the new method correctly reproduces the friction and the out-of-equilibrium corrections to the stress-energy tensor in the whole range of z. Although at the qualitative level an excellent agreement is found, some small quantitative differences are present. In particular, differences of order 1% are present in the region corresponding to the peak ($z \sim 1$), while order 10% discrepancies can be present in the tails, both inside and outside the bubble. The impact of the tails in the determination of the total friction and of the DW dynamics is however very limited, since their contribution is highly suppressed, as can be seen from the first panel in the two rows of figure 2.[2]

[2]For some choices of the model parameters, the convergence of the solution in the region $p_z < 0$ and $z \ll 0$ may present some numerical instabilities due to our approximation of the kernel. In this region, however, the perturbations are highly suppressed and give only a marginal contribution to the friction. Moreover possible numerical instability only appear after a number of iterative steps much larger than the ones needed to reach convergence in the relevant part of the perturbations, so they can be easily kept under control in the determination of the DW velocity.

JHEP05(2023)194

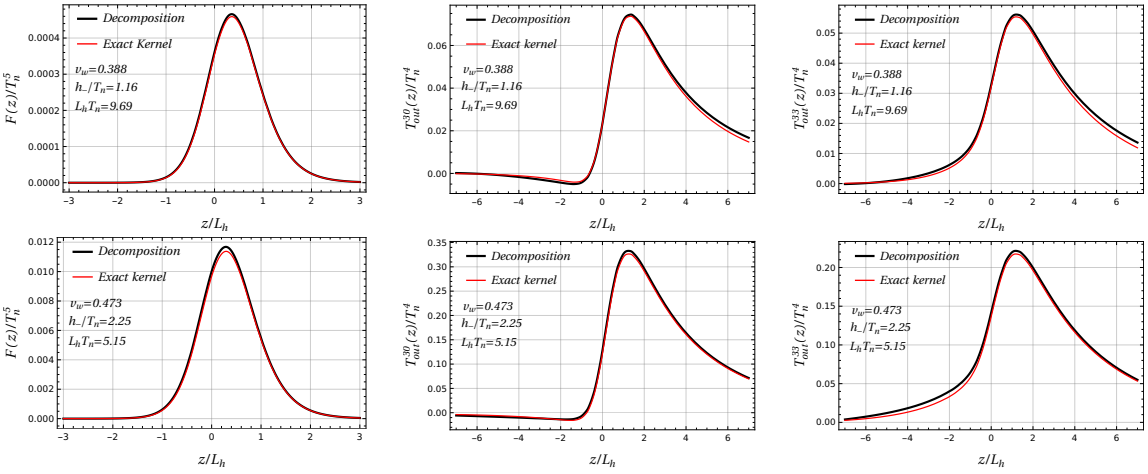

Figure 2. Comparison of the friction (left panel), $T^{30}_{\rm out}$ (central panel) and $T^{33}_{\rm out}$ (right panel) as functions of z/L_h, computed using the procedure presented in ref. [17] (red solid line) and the decomposition method (black solid line), for the benchmark point BP1 (upper row) and BP2 (lower row). The parameters defining the two benchmarks are reported in table 2.

These results thus indicate that the proposed method is robust and can be safely used to reliably study the DW dynamics.

5.1 Solution to the scalar field equations of motion

The DW terminal speed is the result of a balance between the internal pressure of the wall and the friction. To determine it, one has to solve the equation of motion of the two scalar fields together with the Boltzmann equation that determines the out-of-equilibrium perturbations and, through eq. (2.1), the friction.

In the wall reference frame the equations of motion of the Higgs and scalar singlet fields are

$$\begin{aligned} E_h &\equiv -\partial_z^2 h + \frac{\partial V(h,s,T)}{\partial h} + F(z)/h' = 0\,, \\ E_s &\equiv -\partial_z^2 s + \frac{\partial V(h,s,T)}{\partial s} = 0\,. \end{aligned} \tag{5.4}$$

The solution to the above system of equations yields the exact profiles of the Higgs and singlet fields. For most applications, however, it is not necessary to solve for the exact field profiles. A good approximate solution is given by a tanh ansatz, namely

$$\begin{aligned} h(z) &= \frac{h_-}{2}\left(1+\tanh\left(\frac{z}{L_h}\right)\right) \\ s(z) &= \frac{s_+}{2}\left(1-\tanh\left(\frac{z}{L_s}+\delta_s\right)\right) \end{aligned} \tag{5.5}$$

where L_h and L_s are the wall thicknesses of the Higgs and the scalar singlet, respectively, while the parameter δ_s describes the displacement between the Higgs and the singlet field walls. The values of the VEVs of the Higgs field inside the DW, h_-, and the singlet in

JHEP05(2023)194

front of the DW, s_+, are computed by minimizing the finite-temperature effective potential, namely

$$\frac{\partial V(h_-, 0, T_-)}{\partial h} = 0\,, \qquad \frac{\partial V(0, s_+, T_+)}{\partial s} = 0\,. \tag{5.6}$$

Clearly, it is possible to consider more general field profiles, but the ansatz in eq. (5.5) is sufficient to reproduce the relevant features of the DW dynamics [20, 35].

The standard strategy to determine v_w, L_h, L_s and δ_s is to compute momenta of E_h and E_s and then seek for the roots of the corresponding equations. A convenient choice of the momenta is [20, 35]

$$\begin{aligned} P_h &= \int dz\, E_h h' = 0\,, \qquad G_h = \int dz\, E_h (2h/h_- - 1) h' = 0\,, \\ P_s &= \int dz\, E_s s' = 0\,, \qquad G_s = \int dz E_s\, (2s/s_+ - 1) s' = 0\,. \end{aligned} \tag{5.7}$$

These equations have a clear physical interpretation. $P_{h,s}$ correspond to the total pressures on the two walls. Thus the sum $P_h + P_s$ is the total pressure that acts on the system. Both pressures must vanish in the steady state regime, otherwise the walls would accelerate. As confirmed by the numerical analysis, we expect the combination $P_h + P_s$ to mostly depend on v_w and being less sensitive to the remaining parameters. The difference of pressures $P_h - P_s$, instead, depends mainly on the displacement δ_s. Finally $G_{h,s}$ take into account the presence of pressure gradients which may stretch or compress the walls. Thus the requirement $G_{h,s} = 0$ fixes the widths of the two walls.

In order to close the system of equations (5.7), one should include the Boltzmann equation for the out-of-equilibrium distributions. However, the perturbations that determine the friction depend on the unknown parameters v_w and L_h. To address this problem one can employ the iterative procedure outlined below:

1. Solve eq. (5.7) without the perturbations, namely at equilibrium, and compute the four parameters v_w, L_h, L_s and δ_s.

2. Use the four parameters to determine the out-of-equilibrium perturbations by solving the Boltzmann equation.

3. Insert the perturbations in eq. (5.4) and recompute the parameters from eq. (5.7).

4. Iterate the procedure from point 2 until the convergence of the four parameters is reached.

To numerically solve eq. (5.7) we implemented the Newton algorithm, while to solve the Boltzmann equation we followed the iterative procedure described in ref. [17] with the bracket term $\langle \delta f \rangle$ computed following the strategy explained in section 3. We report in table 2 our results for two benchmark points. In the table we show the values of the four parameters with and without the contributions of the out-of-equilibrium perturbations. The bubble speed is the parameter more strongly affected by the out-of-equilibrium contributions, followed by the width of the Higgs wall. For the first benchmark model with $m_s = 103.8\,\text{GeV}$, a difference of $\sim 30\%$ and of $\sim 20\%$ is present for the speed v_w and the

JHEP05(2023)194

	m_s (GeV)	λ_{hs}	λ_s	T_n (GeV)	T_c (GeV)	T_+ (GeV)	T_- (GeV)
BP1	103.8	0.72	1	129.9	132.5	130.3	129.9
BP2	80.0	0.76	1	95.5	102.8	97.5	95.5

	v_w	δ_s	$L_h T_n$	$L_s T_n$
BP1	0.39 (0.57)	0.79 (0.75)	9.7 (8.1)	7.7 (6.7)
BP2	0.47 (0.61)	0.81 (0.81)	5.2 (4.7)	4.3 (4.1)

Table 2. Critical and nucleation temperatures, temperatures in front and behind the DW and terminal values of the parameters v_w, δ_s, L_h, L_s for two benchmark points. The numbers in parentheses correspond to the results obtained neglecting the out-of-equilibrium perturbations.

wall width L_h, respectively, with respect to the same values computed in local equilibrium. The width L_s and the displacement δ_s show, instead, a difference of $\sim 15\%$ and a milder one of $\sim 5\%$ respectively. The four parameters in the second benchmark model with $m_s = 80\,\text{GeV}$ still present important differences with respect to the only-equilibrium case, but the impact of the out-of-equilibrium contributions is less severe. As for the previous benchmark model, the perturbations mostly impact on the speed on which they induce a change of $\sim 20\%$. The offset δ_s, instead, is almost unaffected by the inclusion of the out-of-equilibrium corrections.

To understand why the out-of-equilibrium perturbations have a different impact on the two benchmark models, it is useful to study the total pressure acting on the system. This will also clarify why the terminal speed v_w is the parameter more strongly affected by the out-of-equilibrium corrections. Using eq. (5.7) the total pressure acting on the system can be expressed as

$$P_h + P_s = \Delta V + \int dz\, \frac{T'}{T} w(T) + \int dz\, F(z) = 0 \tag{5.8}$$

where ΔV is the potential energy difference between the true and false vacuum. The size of this difference increases with the amount of supercooling in the PhT. For small supercooling, the friction is comparable to the potential difference and the out-of-equilibrium corrections have an important impact on the DW dynamics. As we notice from table 2, the model where the out-of-equilibrium corrections have a bigger impact indeed corresponds to the one with less supercooling.

We plot on the left panel of figure 3 the total pressure as a function of the wall speed, with (black line) and without (red line) the inclusion of the out-of-equilibrium distributions. In both curves we can observe the presence of a peak corresponding to the Jouguet velocity. The peak originates from hydrodynamic effects that heat up the plasma, thus generating a pressure barrier that slows down the DW motion in models with small supercooling [37]. This effect is described in eq. (5.8) by the term proportional to the enthalpy and its impact grows with the difference $T_+ - T_-$, so that it tends to be larger for hybrid walls.

At small velocities, instead, the pressure at equilibrium becomes constant. In this case the temperature difference across the wall becomes negligible and the value of the total

JHEP05(2023)194

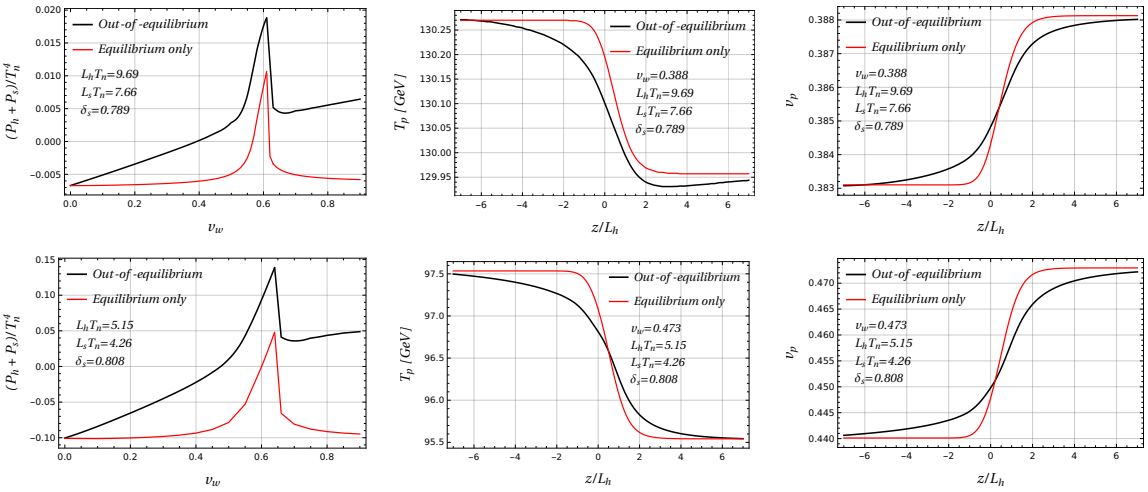

Figure 3. Total pressure as a function of the bubble speed, temperature and velocity profiles as functions of z/L_h for the two benchmark models reported in table 2 (BP1 on the upper row, BP2 on the lower row). The red solid lines are obtained by neglecting the out-of-equilibrium perturbations, while the black solid lines correspond to the complete computation. The peak in the pressure is located at the Jouguet velocity.

pressure settles to the potential energy difference between the false and true vacua at the nucleation temperature.

The out-of-equilibrium perturbations provide a correction that grows linearly with the velocity. This behaviour is consistent with the one found in ref. [17], where a linear dependence of the total friction was observed. From the above discussion we conclude that the perturbations have an important impact on the wall terminal speed and, therefore, an accurate modeling of the out-of-equilibrium perturbations is necessary to get a proper description of the PhT dynamics.

In the central and right panel of figure 3 we plot the temperature and velocity profiles, respectively, for the terminal values of v_w, L_h, L_s, δ_s of the two benchmark models reported in table 2. The plots clearly show that the out-of-equilibrium perturbations impact on the shape of the profiles, mostly in the region close to the DW. Among all the three terms in eq. (5.8), the modified shapes of the profiles have the largest effect on the term involving the temperature derivative.

We now give an estimation of the impact of the temperature and velocity profiles on the Boltzmann equation. They contribute to the source term through their derivatives and, thus, we expect their effect to be proportional to the relative difference between the temperature and velocity across the DW. This expectation is confirmed by our numerical analysis. We computed the integral of the friction for three benchmark velocities ($v_w = 0.4, 0.6, 0.9$) and we compared with the result obtained by considering a constant temperature and plasma velocity across the system. Our analysis showed that corrections of few % are present for $v_w = 0.4$ and $v_w = 0.9$, while we found larger corrections ($\sim 10\%$) for $v_w = 0.6$. Such result agrees with the expected behavior since the largest correction is found for velocities close to the Jouguet velocity, where the differences between the temper-

JHEP05(2023)194

ature and plasma velocity across the wall are larger. From these results we can conclude that, despite the profiles have to be included to compute the equilibrium part of the total pressure acting on the system, they may be typically neglected in the computation of the out-of-equilibrium friction.

Finally we comment on the comparison of our results with the previous literature. We found a fair agreement with the results given in ref. [35], in which the DW terminal speed for a similar potential is computed by solving the Boltzmann equation within the fluid approximation. This approach, as we showed in ref. [17], tends to overestimate the value of the friction for subsonic walls by $\sim 10\% - 20\%$. The results reported in table 2 show differences with respect to the values in ref. [35] that are compatible up to these effects.

On the other hand, we found much larger differences with respect to the results in ref. [20], in which the out-of-equilibrium perturbations are found to provide only a small correction to the DW terminal velocity. To investigate the source of discrepancy, we explicitly implemented the procedure proposed in ref. [20], decomposing the perturbations in terms of Chebyschev polynomials. With this approach we recovered the results obtained with our method up to $\sim 20\%$ differences, which are most probably due to the different size of the grids used to discretize the perturbations. Other sources of differences could be the choice of the scalar potential (and of its renormalization procedure) and of the model parameters, which could lead to a different amount of supercooling.

6 Conclusions

In this work we developed a new algorithm for the computation of the collision integrals in the Boltzmann equations that determine the distribution functions of plasma species in the presence of a travelling DW. This physical setup is relevant for a quantitative description of first-order PhTs in the early Universe and, in particular, for the computation of cosmic relics, such as the stochastic background of gravitational waves and the matter-antimatter asymmetry.

The method presented here exploits a spectral decomposition of the collision integral, reinterpreting it as a suitable Hermitian integral operator. This new approach significantly improves the computational efficiency of our previous algorithm [17] by effectively reducing a nine-dimensional integration into a much faster matrix multiplication. On top of that, since the eigenfunctions need to be computed only once, they can be reused in all the scanning procedure of the parameter space of an entire model.

To validate our new spectral method we compared it with the approach we developed in our previous work [17]. We found excellent agreement for the value of the friction and for the determination of the out-of-equilibrium perturbations in the plasma. Small deviations, of order 1% in the most relevant regions (see figure 2), could be systematically reduced by increasing the number of points in the grid used for the discretization of the collision operator.

We further complemented our analysis by including the contribution of the background species obtained by solving the hydrodynamic equations for their temperature and velocity profiles. Contrary to most of the previous approaches, following ref. [20], we did not

JHEP05(2023)194

linearize in the former quantities, thus avoiding any singular behavior at the speed of sound.

As an explicit application of our formalism, we applied it to the study of a first-order EWPhT in the Z_2-symmetric singlet extension of the SM. We inspected two benchmark points, calculating the relevant features of the wall dynamics, namely the wall speed, its width and the displacement between the two field profiles. In order to assess the impact of the out-of-equilibrium distributions we also reevaluated the same parameters without the friction. The main results are shown in figure 3 and in table 2, and clearly highlight the crucial impact of the out-of-equilibrium dynamics, which introduces large corrections, mainly to the speed of the bubble wall.

For the purpose of presenting the new computational strategy, we considered a simplified setup with the top quark being the only species out-of-equilibrium. Clearly, the inclusion of EW gauge bosons, or any other massive state, is straightforward once the kernels for the corresponding processes are computed. We leave this aspect for a future work.

On the technical level, a possible improvement in the kernel reconstruction could be obtained by the use of a suitable decomposition basis. As we mentioned in the main text, due to the rotational invariance of the collision operator, a natural choice is given by the Legendre polynomials in the angular variable. Such choice could be useful to reduce the number of eigenmodes needed to obtain good accuracy and to improve numercal stability. A full decomposition of the Boltzmann equation on such basis could also be worth exploring.

Finally, we remark that the decomposition method of the collision integrals presented in this work increases the feasibility of a scan of the parameter space of an entire model that otherwise would be extremely challenging due to the amount of required computational resources. As we mentioned before, the huge timing performance that we achieved allows to fully solve the Boltzmann equation efficiently and reliably. We plan to analyze some of the most relevant BSM scenarios providing signals of gravitational waves from cosmological first-order PhT in a following work.

Acknowledgments

We thank B. Laurent for useful discussions. This project was supported in part by the MIUR under contract 2017FMJFMW (PRIN2017). A.G.M. has been supported by the Secretariat for Universities and Research of the Ministry of Business and Knowledge of the Government of Catalonia and the European Social Fund.

A Boundary conditions for the hydrodynamic equations

In this appendix we briefly review the computation of the boundary values of the plasma velocity $v_{p\pm}$ and temperature $T_\pm$ (see refs. [20, 22] for more details).

The conservation of the energy-momentum tensor across the DW implies,

$$v_{p+}v_{p-} = \frac{1-(1-3\alpha_+)r}{3-3(1+\alpha_+)r} \qquad \frac{v_{p+}}{v_{p-}} = \frac{3+(1-3\alpha_+)r}{1+3(1+\alpha_+)r}, \tag{A.1}$$

JHEP05(2023)194

where v_{p+} and v_{p-} are computed in the wall reference frame and

$$\alpha_+ = \frac{\epsilon_+ - \epsilon_-}{a_+ T_+^4}\,, \qquad r = \frac{a_+ T_+^4}{a_- T_-^4}\,, \tag{A.2}$$

with

$$a_\pm = -\frac{3}{4T_\pm^3}\frac{\partial V}{\partial T}\bigg|_{\phi_i=\phi_i^\pm, T=T^\pm}\,, \qquad \epsilon_\pm = \left(-\frac{T_\pm}{4}\frac{\partial V}{\partial T} + V\right)\bigg|_{\phi_i=\phi_i^\pm, T=T^\pm}\,. \tag{A.3}$$

By using eq. (A.1) we can express two of the four boundary conditions as functions of the remaining two. The latter depend on the qualitative properties of the plasma which are, in turn, determined by the DW velocity v_w. It is possible to identify three different regimes, depending on the value of v_w, for the temperature and plasma velocity profiles, each one characterized by different boundary conditions: deflagration ($v_w < c_s^-$) where a shock wave precedes the DW, detonations ($v_w > v_J$) where a rarefaction wave trails the DW and hybrid ($c_s^- < v_w < v_J$), where both a shock and a rarefaction wave are present. The speed of sound inside the wall c_s^- can be computed from the definition of c_s, namely,

$$c_s^2 = \frac{\partial V/\partial T}{T\partial^2 V/\partial T^2}\,, \tag{A.4}$$

while v_J identifies the model-dependent Jouguet velocity, at which $|v_{p-}| = c_s^-$ holds.

In the case of detonations, the wall hits an unperturbed plasma in front of it and one can trivially identify $T_+ = T_n$ and $|v_{p+}| = v_w$ (in the wall frame), thus immediately determining, with the use of eq. (A.1), the four boundary conditions.

The determination of the boundary conditions in the deflagration and hybrid cases is much more involved and requires to evolve the temperature and velocity profiles between the DW and the shock wave. Assuming a spherical bubble and a thin wall, from the conservation of the energy-momentum tensor we find, in the reference frame of the bubble center,

$$\begin{aligned} 2\frac{v_p(\xi)}{\xi} &= \gamma(v_p(\xi))^2(1 - v_p(\xi)\xi)\left(\frac{\mu(\xi, v_p(\xi))^2}{c_s^2} - 1\right)\partial_\xi v_p(\xi) \\ \partial_\xi T(\xi) &= T(\xi)\gamma(v_p(\xi))^2\mu(\xi, v_p(\xi))\partial_\xi v_p(\xi), \end{aligned} \tag{A.5}$$

where ξ is the velocity of a given wave profile, $v_p(\xi)$ is the plasma velocity in the frame of the bubble center, while $\mu(\xi, v_p(\xi))$ is the Lorentz-transformed plasma velocity (in the reference frame of the wave profile)

$$\mu(\xi, v_p(\xi)) = \frac{\xi - v_p(\xi)}{1 - \xi v_p(\xi)}. \tag{A.6}$$

In the deflagration case the shock wave hits an unperturbed plasma in front of it, $T_+^{SW} = T_n$, and the plasma is at rest behind the DW, $v_{p-} = v_w$, with T_+^{SW} being the temperature in front of the shock wave. Thus the two boundary conditions are specified at different points in the plasma and the determination of $T_\pm$ and v_{p+} is non-trivial. For this purpose, we adopted a shooting method which is sketched below:

JHEP05(2023)194

1. We make an ansatz for T_- we determine T_+ and v_{p+} using eq. (A.1);

2. We use them as initial conditions to integrate eq. (A.5), provided v_{p+} is boosted in the reference frame of the bubble center ($v(\xi = v_w) = \mu(v_w, v_{p+})$);

3. We stop integration just behind the shock wave at $\xi_{\rm SW}$, which is given by the condition $v_{p-}^{\rm SW}\xi_{\rm SW} = c_s^+ = 1/\sqrt{3}$;

4. The outcome of the solution of eq. (A.5), namely the velocity and temperature of the plasma behind the shock wave $v_{p-}^{\rm SW}$, $T_-^{\rm SW}$, are used to compute $v_{p+}^{\rm SW}$, $T_+^{\rm SW}$ by exploiting again eq. (A.1);

5. The procedure is iterated adjusting T_- until the condition $T_+^{\rm SW} = T_n$ is reached.

To determine the boundary conditions for hybrid solutions we can adopt the same strategy, with the only difference that entropy conservation enforces $v_{p-} = c_s^-$.

References

[1] C. Caprini et al., *Science with the space-based interferometer eLISA. II: Gravitational waves from cosmological phase transitions*, *JCAP* **04** (2016) 001 [arXiv:1512.06239] [INSPIRE].

[2] C. Caprini et al., *Detecting gravitational waves from cosmological phase transitions with LISA: an update*, *JCAP* **03** (2020) 024 [arXiv:1910.13125] [INSPIRE].

[3] S. Kawamura et al., *The Japanese space gravitational wave antenna DECIGO*, *Class. Quant. Grav.* **23** (2006) S125 [INSPIRE].

[4] S. Kawamura et al., *The Japanese space gravitational wave antenna: DECIGO*, *Class. Quant. Grav.* **28** (2011) 094011 [INSPIRE].

[5] W.-R. Hu and Y.-L. Wu, *The Taiji Program in Space for gravitational wave physics and the nature of gravity*, *Natl. Sci. Rev.* **4** (2017) 685 [INSPIRE].

[6] W.-H. Ruan, Z.-K. Guo, R.-G. Cai and Y.-Z. Zhang, *Taiji program: Gravitational-wave sources*, *Int. J. Mod. Phys. A* **35** (2020) 2050075 [arXiv:1807.09495] [INSPIRE].

[7] TianQin collaboration, *TianQin: a space-borne gravitational wave detector*, *Class. Quant. Grav.* **33** (2016) 035010 [arXiv:1512.02076] [INSPIRE].

[8] C. Gowling and M. Hindmarsh, *Observational prospects for phase transitions at LISA: Fisher matrix analysis*, *JCAP* **10** (2021) 039 [arXiv:2106.05984] [INSPIRE].

[9] N. Turok, *Electroweak bubbles: Nucleation and growth*, *Phys. Rev. Lett.* **68** (1992) 1803 [INSPIRE].

[10] B.-H. Liu, L.D. McLerran and N. Turok, *Bubble nucleation and growth at a baryon number producing electroweak phase transition*, *Phys. Rev. D* **46** (1992) 2668 [INSPIRE].

JHEP05(2023)194

[11] S.Y. Khlebnikov, *Fluctuation - dissipation formula for bubble wall velocity*, *Phys. Rev. D* **46** (1992) R3223 [INSPIRE].

[12] P.B. Arnold, *One loop fluctuation - dissipation formula for bubble wall velocity*, *Phys. Rev. D* **48** (1993) 1539 [hep-ph/9302258] [INSPIRE].

[13] G.D. Moore and T. Prokopec, *Bubble wall velocity in a first order electroweak phase transition*, *Phys. Rev. Lett.* **75** (1995) 777 [hep-ph/9503296] [INSPIRE].

[14] G.D. Moore and T. Prokopec, *How fast can the wall move? A Study of the electroweak phase transition dynamics*, *Phys. Rev. D* **52** (1995) 7182 [hep-ph/9506475] [INSPIRE].

[15] B. Laurent and J.M. Cline, *Fluid equations for fast-moving electroweak bubble walls*, *Phys. Rev. D* **102** (2020) 063516 [arXiv:2007.10935] [INSPIRE].

[16] G.C. Dorsch, S.J. Huber and T. Konstandin, *On the wall velocity dependence of electroweak baryogenesis*, *JCAP* **08** (2021) 020 [arXiv:2106.06547] [INSPIRE].

[17] S. De Curtis et al., *Bubble wall dynamics at the electroweak phase transition*, *JHEP* **03** (2022) 163 [arXiv:2201.08220] [INSPIRE].

[18] G.C. Dorsch, S.J. Huber and T. Konstandin, *A sonic boom in bubble wall friction*, *JCAP* **04** (2022) 010 [arXiv:2112.12548] [INSPIRE].

[19] J.M. Cline, M. Joyce and K. Kainulainen, *Supersymmetric electroweak baryogenesis*, *JHEP* **07** (2000) 018 [hep-ph/0006119] [INSPIRE].

[20] B. Laurent and J.M. Cline, *First principles determination of bubble wall velocity*, *Phys. Rev. D* **106** (2022) 023501 [arXiv:2204.13120] [INSPIRE].

[21] A. Megevand and A.D. Sanchez, *Velocity of electroweak bubble walls*, *Nucl. Phys. B* **825** (2010) 151 [arXiv:0908.3663] [INSPIRE].

[22] J.R. Espinosa, T. Konstandin, J.M. No and G. Servant, *Energy Budget of Cosmological First-order Phase Transitions*, *JCAP* **06** (2010) 028 [arXiv:1004.4187] [INSPIRE].

[23] L. Leitao and A. Megevand, *Spherical and non-spherical bubbles in cosmological phase transitions*, *Nucl. Phys. B* **844** (2011) 450 [arXiv:1010.2134] [INSPIRE].

[24] A. Mégevand, *Friction forces on phase transition fronts*, *JCAP* **07** (2013) 045 [arXiv:1303.4233] [INSPIRE].

[25] S.J. Huber and M. Sopena, *An efficient approach to electroweak bubble velocities*, arXiv:1302.1044 [INSPIRE].

[26] A. Megevand and F.A. Membiela, *Stability of cosmological deflagration fronts*, *Phys. Rev. D* **89** (2014) 103507 [arXiv:1311.2453] [INSPIRE].

[27] L. Leitao and A. Megevand, *Hydrodynamics of phase transition fronts and the speed of sound in the plasma*, *Nucl. Phys. B* **891** (2015) 159 [arXiv:1410.3875] [INSPIRE].

[28] A. Megevand and F.A. Membiela, *Stability of cosmological detonation fronts*, *Phys. Rev. D* **89** (2014) 103503 [arXiv:1402.5791] [INSPIRE].

[29] A. Megevand, F.A. Membiela and A.D. Sanchez, *Lower bound on the electroweak wall velocity from hydrodynamic instability*, *JCAP* **03** (2015) 051 [arXiv:1412.8064] [INSPIRE].

[30] S. De Curtis et al., *Bubble wall dynamics at the electroweak scale*, *PoS* **ICHEP2022** (2022) 080 [INSPIRE].

JHEP05(2023)194

[31] S. De Curtis et al., *Dynamics of bubble walls at the electroweak phase transition*, *EPJ Web Conf.* **270** (2022) 00035 [arXiv:2209.06509] [INSPIRE].

[32] S.R. De Groot, *Relativistic Kinetic Theory. Principles and Applications*, North-Holland Publishing Company (1980) [INSPIRE].

[33] P.M. Morse and H. Feshbach, *Methods of theoretical physics*, McGraw-Hill Book Company (1953).

[34] S. De Curtis, L. Delle Rose and G. Panico, *Composite Dynamics in the Early Universe*, *JHEP* **12** (2019) 149 [arXiv:1909.07894] [INSPIRE].

[35] A. Friedlander, I. Banta, J.M. Cline and D. Tucker-Smith, *Wall speed and shape in singlet-assisted strong electroweak phase transitions*, *Phys. Rev. D* **103** (2021) 055020 [arXiv:2009.14295] [INSPIRE].

[36] M. Quiros, *Finite temperature field theory and phase transitions*, in the proceedings of the *ICTP Summer School in High-Energy Physics and Cosmology, Trieste, Italy, 29 June – 17 July 1998*, (1999) p. 187–259 [hep-ph/9901312] [INSPIRE].

[37] T. Konstandin and J.M. No, *Hydrodynamic obstruction to bubble expansion*, *JCAP* **02** (2011) 008 [arXiv:1011.3735] [INSPIRE].

JHEP05(2023)194

Paper 3: Lighten up Primordial Black Holes in the Galaxy with the QCD axion: Signals at the LOFAR Telescope

Lighten up Primordial Black Holes in the Galaxy with the QCD axion: Signals at the LOFAR Telescope

Ricardo Z. Ferreira[1, *] and Ángel Gil Muyor[2, †]

[1] *CFisUC, Department of Physics, University of Coimbra, P-3004 - 516 Coimbra, Portugal*
[2] *Institut de Física d'Altes Energies (IFAE) and Barcelona Institute of Science and Technology (BIST), Universitat Autònoma de Barcelona, 08193 Bellaterra, Barcelona, Spain*

(Dated: April 22, 2024)

In this work, we study the luminosity that results from the conversion of QCD axion particles into photons in the magnetic field of the plasma accreting onto black holes (BHs). For the luminosities to be large two conditions need to be met: i) there are large numbers of axions in the PBH surroundings as a result of the so-called superradiant instability; ii) there exists a point inside the accreting region where the plasma and axion masses are similar and there is resonant axion-photon conversion. For BHs accreting from the interstellar medium in our galaxy, the above conditions require the black hole to have subsolar masses and we are therefore led to consider a population of primordial black holes (PBHs). In the conservative window, where we stay within the non-relativistic behavior of the plasma and neglect the possibility of non-linear enhancement via magnetic stimulation, the typical frequencies of the emitted photons lie on the low-radio band. We thus study the prospects for detection using the LOFAR telescope, assuming the PBH abundance to be close to the maximal allowed by observations. We find that for PBH and QCD axion with masses in the range $10^{-5} - 10^{-4}\,M_\odot$ and 4×10^{-8} and 4×10^{-7} eV, respectively, the flux density emitted by the closest PBH, assuming it accretes from the warm ionized medium, can be detected at the LOFAR telescope. Coincidently, the PBH mass range coincides with the range that would explain the microlensing events found in OGLE. This might further motivate a dedicated search of these signals in the LOFAR data and other radio telescopes.

I. INTRODUCTION

Compact astrophysical objects such as core-collapse supernovae or neutron stars can be efficient QCD axion *factories* and therefore they provide important input in the quest to detect the QCD axion. Indeed, SN1987A explosion still provides the strongest upper bounds on the QCD axion mass [1, 2] and neutron stars have also been shown to provide interesting input in this direction [3]. But compact objects can also be efficient QCD axion *converters*, rather than factories, when they host large magnetic fields, such as those present in magnetars or white dwarfs. The presence of a plasma mass allows for a resonant conversion of non-relativistic axions into radio photons, and recent studies have already been able to place constraints using radio telescope data [4–13].

What about black holes (BHs)? What is peculiar about the BH case, when compared to the other compact objects, is that the QCD axion can be dynamically generated in very large numbers, in a cloud surrounding the BH, if the so-called superradiant condition is satisfied [14, 15]. The cloud can be very massive and store up to $\sim 10\%$ of the black hole mass [16, 17], and this purely gravitational phenomenon has already been used to exclude the QCD axion for the lightest masses [18–21].

However, this might not be the only way to probe the QCD axion with BHs. In contrast with other axion-like particles, the QCD axion necessarily couples photons with a strength that is mostly fixed by the axion mass. Therefore, if some mechanism is able to convert even a small percentage of the axions in the superradiant cloud into photons in the black hole surroundings, this can open new observational probes. In that sense, one possibility that has been considered is that the axions in the cloud decay to two photons, and stimulation effects can then result in fast radio bursts [22, 23]. The possibility of axion-photon conversion on the magnetic fields surrounding the cloud has also been discussed in previous literature [24, 25].

In this work, we will explore how the the accretion of plasma and magnetic field from the interstellar medium (ISM) onto the black hole can affect this picture and argue that the situation becomes closer to the resonant conversion that happens, for example, in magnetars. Axions can decay to two photons as long as the axion mass m_a is larger than twice the plasma mass ω_p. However, the presence of the magnetic field opens up a new channel, axion-to-photon conversion, that is typically more efficient than the decay to two photons and is, in fact, the only process kinematically allowed when $\omega_p > m_a/2$. Moreover, the plasma density and the magnetic field increase towards the BH horizon at a pace that depends on the accretion flow. Then, as long as the plasma mass of the medium is smaller than the QCD axion mass outside the accreting region, there can be a critical radius inside the accreting region where the QCD axion and the plasma mass are close to each other thus allowing resonant conversion between the two. If the critical radius happens to be close to the position of the superradiant cloud, where the axion densities are higher, it is then

* rzferreira@uc.pt
† agil@ifae.es

likely that many QCD axions will convert into photons. The ISM magnetic fields are much weaker than those observed in magnetars, but that can be largely compensated by the enormous number of axions in the cloud thus boosting the luminosity of the process. Moreover, contrarily to the case of neutron stars or white dwarfs, here the axions that convert into photons are dynamically generated by the superradiant instability, so the mechanism does not rely on the assumption of an initial axion profile.

However, when restricting to BHs in our galaxy, imposing that the critical radius occurs close to the superradiant cloud typically requires the BHs to have subsolar masses and we are therefore led to assume a population of primordial black holes (PBHs). We will then show that in the most conservative region, where we neglect the possibility of non-linear enhancement via magnetic stimulation and where the electrons are non-relativistic at the conversion point, the photons emitted from the resonance are on the low-radio band and can readily be searched for with the LOFAR radio telescope [26]. Coincidently, the region probed by LOFAR corresponds to PBH with masses in the range where there have been recent hints from microlensing events [27].

The manuscript is organized as follows. In section II we provide a brief summary of the superradiant phenomena and give the basic properties of the cloud and of the QCD axion. Section III A describes the typical properties of the interstellar medium in our galaxy in terms of electron density, temperature and magnetic fields. Section III B concerns the Bondi accretion onto black holes and the associated accreting profiles. The main mechanism of this work, the resonant conversion, is described in section IV. In section V, we discuss the observational prospects for detection with LOFAR. Finally in section VI we conclude and give some outlook for the future. Most of the technical details are left for the appendices. In appendix A we give the typical values of the properties of the interstellar medium that we use in this work. In appendix B and C we explain how we use the method of variation of parameters to find a solution for the equation of motion of the photon around the superradiant cloud, and find, in appendix D, a simplified expression for the luminosity of the system. Finally, in appendix E we discuss the phenomena of magnetic stimulation and discuss the region of parameters where we expect that to happen.

II. SUPERRADIANCE AND THE QCD AXION

Via the superradiant instability, it is possible to convert a significant part of the BH spin into dense QCD axions clouds [25]. The axions in these clouds are in quasi-bound states similar to the hydrogen atom, labeled by n, l, and m and with energies $\omega_{nlm} \simeq m_a(1-\alpha^2/2n^2)$, where

$$\alpha = GMm_a \tag{1}$$

is the gravitational coupling, analogous of the fine-structure constant, and m_a is the QCD axion mass. For the superradiant phenomena to be possible, the condition $m\Omega - \omega_{nlm} > 0$ has to be satisfied, where Ω is the BH angular velocity. This condition enforces the restriction $\alpha < \tilde{a}m/2$ where $|\tilde{a}| < 1$ is the dimensionless spin parameter of the BH.

Among the different superradiant states, the 2p state with $nlm = 211$, is the fastest growing one with rate [28]

$$\Gamma_{211} \simeq \frac{\alpha^8(\tilde{a}-4\alpha)}{24} m_a \,. \tag{2}$$

We will focus on the axions that populate this state as these exist in larger numbers than those in other states.

The axion field in this level $\bar{a}$ has a profile given by

$$\bar{a}(t,\vec{r}) = \sqrt{\frac{N}{2m_a}} \left[e^{-i\omega_{211}t} R_{21}(r) Y_{11}(\hat{r}) + h.c.\right] \tag{3}$$

where N is the number of axions in the cloud, $Y_{11}(\theta,\phi)$ is the $l = m = 1$, spherical harmonic and

$$R_{21}(r) = \left(\frac{1}{24a_0^3}\right)^{1/2} \frac{r}{a_0}\, e^{-r/(2a_0)} \tag{4}$$

is the radial bound state solution of the 211 level with $a_0 = 1/(m_a\alpha) = GM/\alpha^2$ the gravitational Bohr radius of the system, so that the average distance from the BH is

$$r_{\rm cl} \equiv \frac{\int r^3 R_{21}^2\, dr}{\int r^2 R_{21}^2\, dr} = 5a_0 \,. \tag{5}$$

Regarding the spin, each axion in the 2p state has $m = 1$ and so the angular momentum in the cloud is equal to the total number of axions $J_{\rm cl} = N$. Therefore, once most of the BH angular momentum $J_{\rm BH} = \tilde{a}GM_{\rm BH}^2$ is drained to the cloud $J_{\rm cl} \simeq J_{\rm BH}$, the cloud would get a mass

$$M_{\rm cl} = Nm_a = \tilde{a}\alpha M_{\rm BH} \,. \tag{6}$$

In the following sections, we will restrict to situations where the cloud had time to grow substantially until the present time. Therefore, we require the superradiance rate to be faster than the age of the universe which, jointly with the superradiant condition $\alpha < \tilde{a}/2$, sets the following upper and lower bounds on the QCD axion mass [1]

$$\frac{5.3\times10^{-4}}{\tilde{a}^{1/9}}\left(\frac{M_\odot}{M}\right)^{8/9} \lesssim \frac{m_a}{10^{-9}\ {\rm eV}} \lesssim 0.067\,\tilde{a}\left(\frac{M_\odot}{M}\right). \tag{8}$$

[1] In terms of the axion decay constant f_a, the range is

$$\frac{9.4\times10^{18}}{\tilde{a}^{-1/9}}\left(\frac{M}{M_\odot}\right)^{8/9} \gtrsim f_a/{\rm GeV} \gtrsim \frac{8.5\times10^{16}}{\tilde{a}}\left(\frac{M}{M_\odot}\right). \tag{7}$$

Current observational bounds restrict the QCD axion mass to lie roughly in the interval $10^{-11}-10^{-1}$ eV [29]. In particular, the absence of a superradiance cloud around the observed rotating stellar mass black holes is what sets the lower bound [20]. We are therefore led to consider QCD axion clouds that form around primordial black holes (PBH) that we will assume to exist with a fraction $f_{\rm PBH}$ of the total dark matter abundance. Moreover, we will be interested in the coupling between the QCD axion and the photon which has the form

$$\mathcal{L} \supset \frac{g_{a\gamma}}{4} a F_{\mu\nu}\tilde{F}^{\mu\nu} \tag{9}$$

where F is the electromagnetic field strength tensor, $\tilde{F}$ is its dual and $g_{a\gamma}$ is the axion-photon coupling constant which, in the QCD axion case, is directly related to its mass via the relation

$$g_{a\gamma} = 2\times 10^{-19} c_\gamma \left(\frac{m_a}{10^{-9}\text{eV}}\right) \text{GeV}^{-1}\,, \tag{10}$$

where c_γ is a model-dependent parameter of order one [29]. In this work, we will use the conservative value of $c_\gamma = 1$.

III. ACCRETION FROM THE INTERSTELLAR MEDIUM

The PBH hosting the QCD axion cloud does not live in isolation. In this section, we discuss the properties of the astrophysical environment surrounding the system. We will focus on PBHs that accrete from the interstellar medium (ISM) in our galaxy and so start by discussing a few relevant properties of the ISM that play a major role in the axion-photon conversion: the photon plasma mass ω_p, the magnetic field B and the sound speed c_s (that we summarize in Table A1). We then proceed with a discussion of the accreting dynamics onto the PBH and the resulting profiles.

A. Interstellar medium

Starting from the photon plasma mass, in the non-degenerate and non-relativistic limit, it is given by

$$\begin{aligned}\omega_p &= \left(\frac{4\pi\alpha_{\rm EM} n_e}{m_e}\right)^{1/2} \\ &= 1.2\times 10^{-11}\left(\frac{n_e}{0.1\text{cm}^{-3}}\right)^{1/2}\text{eV},\end{aligned} \tag{11}$$

where m_e is the electron mass, $\alpha_{\rm EM}$ is the electromagnetic coupling constant and n_e is the electron density that we normalized to the typical value in the warm ionized medium. The electron density is related to the medium density n_∞ by the ionization fraction x_e. The plasma mass can go down by one order of magnitude in the more rarified hot ionized medium but it can also be larger in denser components of the ISM. In Table A1 we show typical values of these quantities. For the conversion to take place, the frequency of the axions in the cloud $\omega_a = \omega_{211} \approx m_a$ needs to be larger than the photon plasma mass,

$$\omega_a \geq \omega_p\,. \tag{12}$$

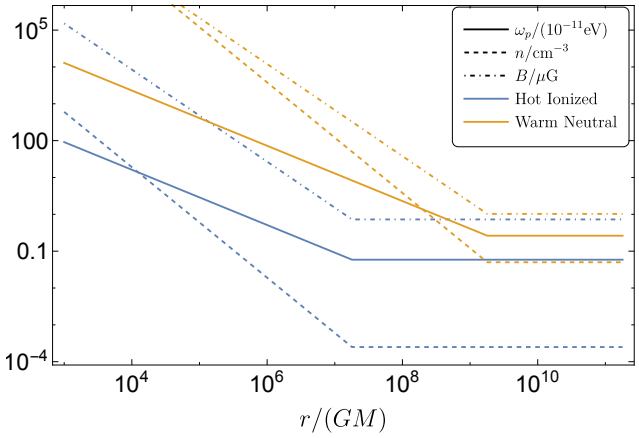

FIG. 1. Profiles for the plasma density, magnetic field and medium density in the hot ionized and warm neutral media.

The accretion of the plasma onto the black hole will further increase its local density and thus place stronger constraints on the possible axion masses that can be converted into photons, as we will study in detail in the following sections. Smaller ISM densities allow a wider range of axions to convert into photons; for that reason, and because of the large filling factors that ensure that there are many PBH in such environments [30], we will mostly focus on the warm and hot ionized components of our galaxy. [2]

Another important property for the axion-photon conversion is the magnetic field. In the ISM their typical strength is of order μG in the hot ionized bubble and the warm neutral medium [32–34] but larger values, of order 10μ G, have also been found in regions of Hydrogen gas and clouds [30]. The accretion onto the PBH will further increase the local value of the magnetic field towards the PBH and therefore the conversion can take place at values larger than the μG, as we will discuss next.

The last relevant property is the sound speed of the medium c_s that can take values from 0.6 km/sec in dense environments such as molecular clouds, to 100 km/sec in hot ionized medium (c.f. Table A1). The sound speed will affect the accreting properties of the PBH and therefore the conversion. Following [35], we will take the PBH

[2] In the extragalactic space, one expects smaller densities, that can go down to 10^{-7}cm^{-3} [31], and would allow the conversion of lighter QCD axion. However, here we focus on the conversion within our galaxy and leave the extragalactic case for future work.

to have a speed $v_{\rm rel}$ relative to the medium that is smaller or comparable to c_s.

B. Accretion onto the BH

We will assume that the PBH follows a simple model of spherical Bondi accretion [35–37] [3]

$$\dot{M} = \lambda \dot{M}_b \tag{13}$$

where $\lambda = 10^{-4} - 10^{-2}$ is an efficiency parameter [37] and $\dot{M}_b$ is the Bondi accretion rate given by [38, 39]

$$\dot{M}_b = \frac{\beta}{4}\pi\, v\, r_b^2\, n_\infty\, m_p, \tag{14}$$

where $v = \sqrt{v_{\rm rel}^2 + c_s^2}$,

$$r_b = \frac{2GM}{v^2} \tag{15}$$

is the Bondi radius that limits the accreting region, n_∞ is the medium density, m_p is the proton mass and $\beta \sim \mathcal{O}(1)$ is a coefficient that depends on the equation of state of the medium [39, 40].

This accretion is rather inefficient and so the accreting time scales are very large. For example, for medium densities and velocities typical of the hot ionized medium, the accreting time $\tau_{\rm acc} = M/\dot{M}$ is larger than the age of the universe for PBHs with (sub-)solar masses. Therefore, we can safely neglect the change in mass and spin of the PBH due to accretion. Similarly, the luminosity of the accreting flow is also very low. For sub-Eddington accretion rates as those described above the luminosity is $L = \eta \dot{M}$ where $\eta \sim \dot{M}/L_{\rm edd}$ and $L_{\rm edd}$ is the Eddington luminosity [37, 41], thus making these objects quite faint.

For a constant accretion rate with equipartition of kinetic and gravitational energies, the plasma velocity evolves as $v \sim \beta_v \sqrt{GM_{\rm BH}/r}$, where β_v is an order one coefficient that depends on the fluid being accreted, and the density profile can be obtained from Eq. 14 to be [39]

$$n(r) = \frac{\beta}{4\beta_v} n_\infty \left(\frac{r_b}{r}\right)^{3/2}, \qquad r \lesssim r_b\,. \tag{16}$$

For $r \gtrsim r_b$ the density saturates to the medium density n_∞. As a consequence, the photon plasma mass in Eq. 11 will also acquire a radial profile, since $n_e(r) = x_e n(r)$. We show the profiles for the density and the photon mass in Fig. 1. The presence of a radial dependent plasma mass has the important consequence of allowing for the presence of a critical radius $r_{\rm crit}$ such that

$$\omega_p(r_{\rm crit}) = m_a\,, \tag{17}$$

i.e. where the photons in the plasma and the QCD axion have the same mass and so can resonantly convert into each other. As explained in the next section, the conversion to photons of the axion in the cloud will be dominated by the dynamics around this radius (and not at the radius of the cloud). In terms of the model parameters, the critical radius is given by

$$r_{\rm crit} = \left(\frac{\omega_{p,\infty}^2}{4m_a^2}\right)^{2/3} r_b \tag{18}$$

where we have used Eqs. 11, 15 and 16, and defined $\omega_{p,\infty} \equiv \omega_p(r \to \infty)$. We will be interested in situations where the plasma frequency of the ISM is lower than the QCD axion mass, $\omega_{p,\infty} < m_a$, and therefore the critical radius will always be inside the accreting region.

Accretion will also enhance the magnetic field towards the PBH. Magnetic flux conservation requires the magnetic field to grow as $B \propto r^{-2}$ towards the black hole [42]. However, the magnetic field pressure cannot exceed the pressure of the accreting matter [4] and so the magnetic field profile will tend towards equipartition of magnetic, kinetic and gravitational energies [45–48]

$$\frac{B^2}{2} \sim \beta_B \frac{GM}{r} m_p n(r) \tag{19}$$

and thus grow more slowly, as $r^{-5/4}$ (see Fig. 1). The parameter β_B is the ratio between the gas pressure and the magnetic pressure that we take to be of order one as in [48]. Then, for example, for the benchmark properties of the hot ionized medium the typical strength of the magnetic field expected from equipartition is

$$\begin{aligned} B \;&=\; 0.7\sqrt{\frac{\beta_B \beta}{\beta_v}} \left(\frac{v}{100\,{\rm km/sec}}\right) \\ &\times \left(\frac{n_\infty}{10^{-3}\,{\rm cm}^{-3}}\right)^{1/2} \left(\frac{r_b}{r}\right)^{5/4} \mu{\rm G} \end{aligned} \tag{20}$$

consistently with the values discussed in Section III A outside the accretion region. The direction of the magnetic field is however harder to determine and can take different topologies [49]. In section IV we make some assumptions on the directionality and briefly discuss the dependence of the results on those assumptions.

Finally, let us discuss the evolution of the plasma temperature towards the black hole. The expression we used for the plasma frequency in Eq. 11 is valid as long as the electrons are non-relativistic and non-degenerate. However, in hot accretion flows electrons are expected to be

[3] The assumption of Bondi accretion is justified for low-luminosity BHs accreting from low-density regions, as the ones considered in this work.

[4] If the magnetic field pressure is larger than that given by the equipartition of energy the accretion might enter a magnetically dominated state [43, 44]. In this work, we will however only consider situations where the magnetic field strength is fixed by equipartition.

relativistic close to the black hole [50, 51]. We can estimate the radius at which electrons become relativistic by assuming that far enough from the black hole the equipartition of energy determines the electron temperature to be [48]

$$T \sim \frac{GMm_p}{r} \sim 0.9\, m_e \left(\frac{10^3 r_s}{r}\right). \tag{21}$$

At radius $r \lesssim r_{\rm rel} \equiv 10^3 r_s$, electrons become relativistic and the expression for the plasma density in Eq. 11 is no longer adequate. [5] As we will see in the next section, imposing that the axion-photon conversion occurs in a regime where the electrons are non-relativistic provides strong constraints on the parameter space.

IV. AXION-PHOTON CONVERSION IN THE BLACK HOLE VICINITY

Now that we have characterized the environment surrounding the black hole, we can explore its interactions with the axions in the cloud.

The axion-photon coupling in Eq. 10 allows axions to decay to two photons with energies $\omega_\gamma = m_a/2$ at a rate $\Gamma = g_{a\gamma}^2 m_a^3/(64\pi)$ and has been studied in the superradiance context [22, 23, 53–56]. However, axions can also be converted into photons in the accreting magnetic field. The conversion probability per unit length typically scales as $dp/dL \propto g_{a\gamma}^2 B^2 L$ where L is a length scale during which the conversion takes place and it is typically related to the magnetic field coherence length or the width of the resonance band [57]. For the typical values of the ISM magnetic field, $B \sim \mu{\rm G} \sim 10^{-8}{\rm eV}^2 \gg m_a^2$, the conversion process, if available, will likely dominate over the decay to two photons even if $L \sim 1/m_a$. Furthermore, in the region where the plasma frequency is larger than $m_a/2$ but below m_a the decay to photons is kinematically forbidden and the conversion is the only process allowed.

A. Toy model: Photon equation in a spherically symmetric potential

We proceed with the explicit computation of the photon luminosity from the conversion of the axions in the cloud.

The dynamics of photons in an accreting plasma around a rotating black hole has been the subject of several recent studies [58–62]. In particular, there has been an interesting discussion about the possible development of photon superradiance in the presence of a plasma mass. We disregard here this possibility, which has been argued to be unlikely for realistic astrophysical accretions [60], but rather focus on the photon free-state solutions that will be created from the presence of an axion and magnetic field profiles. We follow the approach of [60] and take the Klein-Gordon equation

$$\left[\Box + \omega_p^2(r)\right] \bar{A}(t,\vec{r}) = S(t,\vec{r}) \tag{22}$$

as a toy model for the propagation in the accreting region of the component of the photon field that is parallel to the magnetic field $\bar{A}$, which is the one that interacts with the axion [57]. We also added a source term $S(t,\vec{r})$ that contains the information about the magnetic field and axion cloud profiles. We will assume for simplicity that at the conversion point, the magnetic field is perpendicular to the line of sight and neglect ray-bending effects. On the other hand, we leave the angle between the BH rotation axis and the line of sight free.

As discussed before, one of the constraints we need to impose is that $r_{\rm crit} > 10^3 r_s$ to ensure the non-relativistic behavior of the electrons in the plasma. This means that in the region of the parameter space fulfilling this condition, the conversion point will be far from the PBH horizon and therefore we can safely take the weak field limit of Eq. (22) [20, 28]

$$\left[\partial_t^2 - \nabla^2 + \omega_p(r)^2\left(1 - \frac{2GM_{\rm BH}}{r} + \hat{K}\right)\right]\bar{A}(t,\vec{r}) = g_{a\gamma\gamma}\partial_t \bar{a}(t,\vec{r}) B(r) \tag{23}$$

where ∇ is the gradient operator in spherical coordinates. The terms in $\hat{K}$ includes corrections to the Newtonian potential that are suppressed by α in the non-relativistic limit (see Appendix B of [20]). We will neglect $\hat{K}$ in the remainder of this section.

The magnetic field has a stationary profile, therefore, energy conservation imposes that only the mode of $\bar{A}$ with frequency $\omega_a = \omega_{211} \approx m_a$ will be excited. Moreover, following Sec. III B, we consider that the B field has a radial profile $B(r,\theta,\phi) \simeq B(r)$ so that the decomposition of the source term in terms of spherical harmonics only has non-vanishing coefficients for $l = m = 1$ and the created photon inherits the same angular dependence.

After decomposing the photon and the scalar field, $X = \{A, a\}$, as $\bar{X}(t,\vec{r}) = X(\vec{r})e^{-im_a t} + X^*(\vec{r})e^{im_a t}$ we then find

$$\left[-m_a^2 - \nabla^2 + \omega_p(r)^2\right] A(\vec{r}) = f(\vec{r}) \tag{24}$$

where we have defined $f(\vec{r}) \equiv -im_a g_{a\gamma\gamma} a(\vec{r}) B(r)$.

In Appendices B and C we solve in detail the differential equation 24 and summarize here the main findings. After decomposing the solution in spherical harmonics and applying the method of variation of parameters, the behavior of the solution for A at $r \to \infty$ can be written as

$$A(\vec{r}) \to Y_{11}(\hat{r}) \frac{e^{i\theta(k_\infty r)}}{ik_\infty r} \int f_{11}(r') F(r') r' dr' \tag{25}$$

[5] The value of $r_{\rm rel}$ obtained agrees with more dedicated studies of hot accretion flows [51, 52].

where θ is a phase such that $\partial_r\theta(r\to\infty)=k_\infty$ with $k_\infty=\sqrt{m_a^2-\omega_{p,\infty}^2}$ the photon momentum at infinity, $f_{11}(r)$ the projection of $f(\vec{r})$ over the spherical harmonic $Y_{11}(\hat{r})$, and $F(r)$ the homogeneous solution of Eq. 24 that we find, using WKB methods, to be given by Eq. C12. The factor of k_∞ dividing in Eq. 25 arises from the modulation of the outgoing wave due to the non-constant plasma mass [4]. This factor would have been missed if we had reduced Eq. 24 to a first-order differential equation.

The time-averaged luminosity in the radial direction is related to the Poynting vector $\vec{E}\times\vec{B}$ of the outgoing wave, where $\vec{E}$ is the electric field, and at infinity it is given by

$$\left\langle\frac{dP}{dA}\right\rangle=\left\langle\frac{dP}{r^2d\Omega}\right\rangle = \langle\partial_r\bar{A}(t,\vec{r})\partial_t\bar{A}(t,\vec{r})\rangle = 2\mathrm{Re}(im_aA(\vec{r})^*\partial_rA(\vec{r}))\,. \quad (26)$$

Therefore, the average photon luminosity per unit solid angle simplifies to

$$\left\langle\frac{dP}{dA}\right\rangle=2m_ak_\infty|A(\vec{r})|^2 \quad (27)$$

where we have used the fact that the plasma frequency asymptotes to a small constant value at the Bondi radius, Using Eq. 25 we then find

$$\left\langle\frac{dP}{d\Omega}\right\rangle = |Y_{11}(\hat{r})|^2\,\frac{m_a^2}{k_\infty}g_{a\gamma\gamma}^2N \times\left|\int B(r')R_{21}(r')F(r')r'dr'\right|^2\,. \quad (28)$$

where N is the total number of axions in the cloud given in Eq. 6.

In appendix C we compute the remaining integral. We find that if $\rho_{\rm crit}\equiv m_a\,r_{\rm crit}>1$, most of the support of the integration comes from a region around the critical point, $r\sim r_{\rm crit}$ with width $\Delta L\sim\rho_{\rm crit}^{1/3}$, where the homogeneous solution behaves like an Airy function. For $r\ll r_{\rm crit}$ the photon mass is bigger than the axion energy and the conversion is kinematically blocked whereas for $r\gg r_{\rm crit}$ the homogeneous solution oscillates quickly and the integral is also strongly suppressed.

Furthermore, if the condition $4\rho_{\rm crit}^{2/3}/|3-2\alpha\rho_{\rm crit}|\gtrsim 1$ is verified, both the magnetic field and the radial wave function are approximately constant around the conversion window thus allowing to simplify the expression for the luminosity to:

$$\left\langle\frac{dP}{d\Omega}\right\rangle(\hat{r}) = \frac{m_a}{2}\tilde{n}_{\rm crit}\,\frac{r_{\rm crit}^2}{a_0^3}(L\,g_{a\gamma\gamma}\,B_{\rm crit})^2 \simeq 8\times10^9\,\tilde{a}\left(\frac{\tilde{n}_{\rm crit}}{N}\right)\left(\frac{M_{\rm BH}}{10^{-2}M_\odot}\right)^8\left(\frac{m_a}{10^{-9}\ {\rm eV}}\right)^{\frac{22}{3}} \times\left(\frac{n_\infty}{10^{-3}\,{\rm cm}^{-3}}\right)^{4/3}\left(\frac{100\,{\rm km/sec}}{v}\right)^4{\rm W}. \quad (29)$$

where $n=\tilde{n}/a_0^3=N|R_{21}(r_{\rm crit})Y_{11}(\hat{r})|^2$ is the number density of axions at the critical radius, $B_{\rm crit}$ is the value of the magnetic field at the critical radius and we have normalized quantities to typical values in the hot ionized medium. We have also defined $L=\sqrt{\pi/\omega_p'(r_{\rm crit})}=\sqrt{4\pi\rho_{\rm crit}/3}$ which is sometimes called the width of the conversion region although in this context we find a smaller conversion width of $\Delta L\propto L^{2/3}$. We also verified numerically that the analytical approximation gives a good estimation of the total luminosity.

B. Results

Figure 2 shows the luminosity emitted from the axion-photon conversion, using Eq. 29, for different values of the QCD axion and PBH masses and for two different media in which the PBH accretes: the hot ionized medium and warm ionized medium.

When restricting to parameters below the gray band, we find luminosities as high as 10^7 W for PBHs with masses around $10^{-2}M_\odot$ and QCD axion masses around 10^{-9} eV when the accretion happens in the hot ionized medium. For and accretion in the warm ionized medium, we find instead 10^{12} W for PBH masses around $10^{-5}M_\odot$ and QCD axion masses around 10^{-7} eV. The gray band is the region where the electrons in the accreting plasma are relativistic at the conversion radius (c.f. Eq. 21) and therefore the expression for the plasma mass in Eq. 11 is no longer valid. We do not expect a dramatic change when entering the relativistic limit, given that the plasma mass does not change significantly, but it would require a dedicated computation that goes beyond the scope of this paper.

In Fig. 2, the most luminous region lies around the cyan line which corresponds to the cases where the conversion radius coincides with the average position of the cloud $r_{\rm crit}=r_{\rm cl}$ and requires

$$\frac{m_{\rm a}}{10^{-7}\ {\rm eV}}\approx\left(\frac{n_\infty}{10^{-3}\ {\rm cm}^{-3}}\right)^{1/2}\left(\frac{100\ {\rm km/s}}{v}\right)^{3/2}\alpha^{3/2}\,. \quad (30)$$

We have also restricted the parameter space by the constraints in Eqs. 8 and Eq. 12 that ensure, respectively, that superradiance happens and within the lifetime of the universe, and that the emitted photons can escape the accreting region and propagate throughout the medium. To have an analytical solution we also had to require that $\rho_{\rm crit}>1$. Note that all these constraints are independent of the axion-photon coupling.

As we move to larger α, we expect other effects to become important. Namely, as QCD axion mass increases both the cloud and the critical radius become closer to the PBH and gravitational corrections to Eq. 23 will start becoming important. On the other hand, around the cyan line, as we increase α at some point the magnetic field generated from the conversion becomes larger

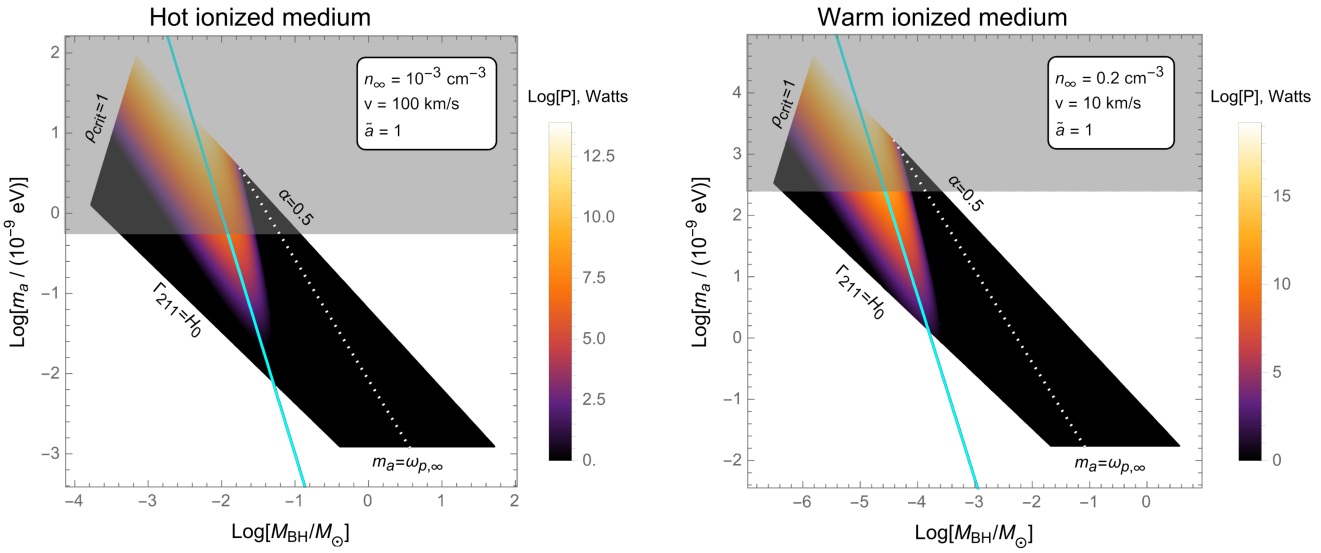

FIG. 2. Luminosity from the resonant conversion to photons of QCD axions in a superradiant cloud for typical values of the hot ionized medium (left plot) and warm ionized medium (right plot) and for a spin parameter $\tilde{a}$ close to one. The cyan line corresponds to when $r_{\rm crit} = r_{\rm cl}$. Inside the gray region, the electrons in the plasma become relativistic at the critical radius. We have also fixed $c_\gamma = 1$ in Eq. 10.

than the original one from accretion and the system is expected to enter a magnetically stimulated regime that we discuss in Appendix E. However, for the media considered in this work, the gravitational effects and the stimulated regime are only relevant inside the gray region and we therefore neglect them in the rest of the analysis.

Finally, to the right of the dotted white line, $4\rho_{\rm crit}^{2/3}/|3-2\alpha\rho_{\rm crit}| < 1$, the magnetic field and the axion profile start varying significantly around the resonant point and Eq. 29 is no longer valid. In this regime, we calculated numerically the luminosity using Eq. 28 and verified that the luminosity is still much suppressed compared to the region around the cyan line.

V. DETECTION PROSPECTS AT RADIO TELESCOPES

In this section, we study the prospects of detecting the signals studied in the previous section with the radio telescope.

The frequency ν of the photons emitted from the conversion is related to the mass of the non-relativistic axions in the cloud:

$$\nu = \frac{m_a}{2\pi} \simeq 0.24 \left(\frac{m_a}{10^{-9}\ \text{eV}}\right) \text{MHz}\,. \tag{31}$$

However, the requirement that the electrons in the plasma are non-relativistic at the conversion radius (see Eq. 21) requires, for the hot ionized medium, that $m_a \lesssim 10^{-9}$ eV and so a maximal photon frequency of approximately 0.2 MHz which is hard to measure with Earth-based telescopes because of the ionosphere screening at 10 MHz, although space-based radio telescopes might allow to go beyond this boundary [63, 64]. Nonetheless, for the warm ionized media the bound is weaker, $\nu_{\rm max} < 100$ MHz, thus leaving open the possibility of detection with radio telescopes. In particular, at these low-radio frequencies the radio telescope LOFAR is the one with the best sensitivities and we therefore proceed with a dedicated study of detectability with LOFAR [26, 65].

The relevant quantity for radio observations is the flux density that is related to the luminosity emitted per solid angle computed in Sec. IV by

$$S = \frac{1}{d^2 \Delta\nu}\frac{dP}{d\Omega} \tag{32}$$

where d is the distance to the source, and $\Delta\nu$ is the typical width of the signal which is related to the variance in the effective velocity of the axions in the cloud $\Delta\nu/\nu \sim \langle v_{\rm cl}^2\rangle = \alpha/2$ [22] since the relative velocity between the BH and the medium is much smaller than $\alpha/2$.

Regarding the typical distance to the closest PBH (d), from Fig. 2, we concluded that photon emission is mostly efficient for PBH with subsolar masses, between $10^{-6} - 10^{-1}\ M_\odot$ depending on the medium. In this range of masses, the PBH cannot account for all the dark matter but can still account for a fraction $f_{\rm PBH} = 1 - 10\%$ of the total [66]. By fixing $f_{\rm PBH}$ we can then estimate the typical distance to the closest PBH to be

$$d = \frac{1}{n_{\rm PBH}^{1/3}} = \left(\frac{M_{\rm BH}}{f_{\rm PBH}\ \rho_{\rm DM}}\right)^{1/3} \tag{33}$$

$$= 0.33 \left(\frac{0.1}{f_{\rm PBH}}\right)^{1/3} \left(\frac{M_{\rm BH}}{10^{-5} M_\odot}\right)^{1/3} \text{ly} \tag{34}$$

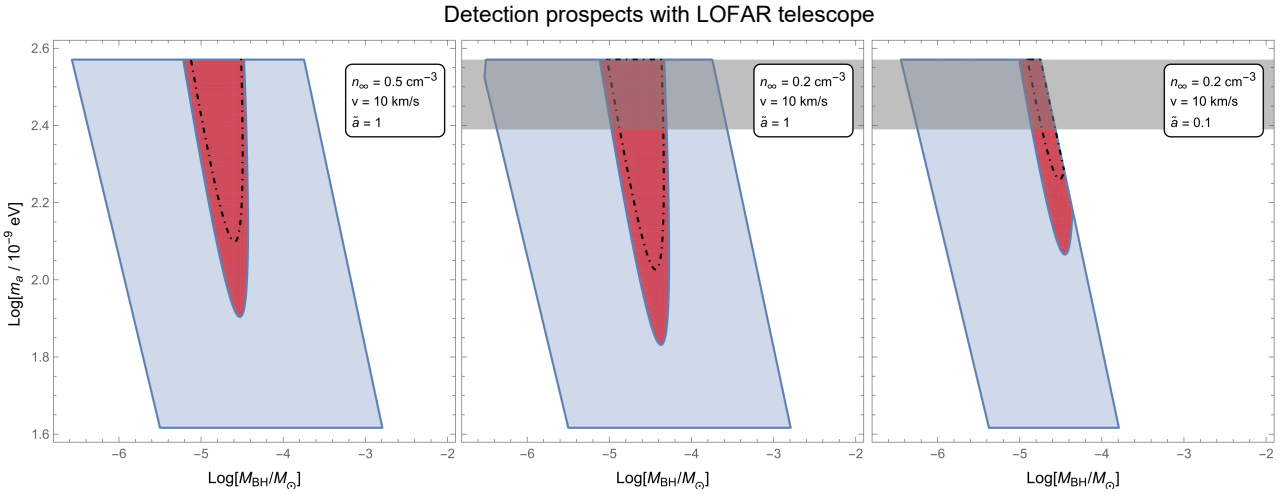

FIG. 3. Parameter space (QCD axion mass vs PBH mass) where the emitted photons lie in the frequency band of LOFAR and i) satisfy the superradiant constraints as in Fig. 2 (Blue region) and ii) can be detected at LOFAR with 8 hours of observation time (Red region). We fixed the PBH fraction to $f_{\rm PBH} = 0.1$, with spin parameter $\tilde{a} = 0.1$ and close to 1 and assumed the closest PBH to be accreting from the warm ionized medium with densities of $n_\infty = 0.2$ and 0.5 cm^{-3} and a relative velocity of $v = 10$ km/s. The angle between the BH rotation axis and the line of sight was fixed to $\pi/2$. The dot-doshed line is the corresponding border for $\pi/8$. Inside the gray region, the electrons are relativistic at the conversion point. We also fixed $c_\gamma = 1$ in Eq. 10.

where $n_{\rm PBH}$ is the number density of PBH. We fixed the dark matter density to the local value $\rho_{\rm DM} = 0.36$ GeV/cm^3 [67] and assumed the PBHs to be roughly uniformly distributed within this region. It is then likely that the closest PBH is within our Local Bubble which is characterized by low densities and large ionization fractions [68]. Then, using the previous equation and the luminosity calculated in Eq. 29 we find that, for some benchmark values of the parameters, the flux density S in Janksys that is expected from the axion-photon conversion is

$$S = 2.54\times10^{10}\ \tilde{a}\left(\frac{\tilde{n}_{\rm crit}}{N}\right)\left(\frac{f_{\rm PBH}}{0.1}\right)^{2/3}\left(\frac{100\,{\rm km/sec}}{v}\right)^4 \times\left(\frac{n_\infty}{10^{-3}\,{\rm cm}^{-3}}\right)^{4/3}\left(\frac{M_{\rm BH}}{M_\odot}\right)^{16/3}\left(\frac{m_a}{10^{-9}\ {\rm eV}}\right)^{13/3}{\rm Jy}. \quad (35)$$

Let us now compare this value with the sensitivity reach of LOFAR that is currently formed by an array of 52 stations spread across northern Europe. Each station has low and high-band antennas; the low-band ones are sensitive to frequencies in the range $10-90$ MHz that we are interested in. The minimum energy flux that a given station can detect is given by the radiometer equation by [26, 65]

$$S_{\rm station} = \frac{2k_B T_{\rm sys}}{A_{\rm eff}\sqrt{\Delta\nu\Delta t}} \quad (36)$$

where k_B is the Boltzmann constant, $T_{\rm sys}$ is the noise temperature of the system, $A_{\rm eff}$ is the effective area, and Δt the observation time. For LOFAR, we take the fiducial values $T_{\rm sys} = 60(\lambda/(1\ {\rm m}))^{2.55}$ Kelvin, and $A_{\rm eff} = 48\lambda^2/3$, where λ is the wavelength of the signal [26]. In the case of an array of $N = 52$ stations, the sensitivity is

$$S_{\rm array} = \frac{2k_B T_{\rm sys}}{A_{\rm eff}\sqrt{2N(N-1)\Delta\nu\Delta t}} \quad (37)$$

which in terms of our model parameters corresponds to

$$S_{\rm array} = 23\left(\frac{M_\odot}{M_{\rm BH}}\right)\left(\frac{10^{-9}\ {\rm eV}}{m_a}\right)^{2.05}\left(\frac{8\ {\rm h}}{\Delta t}\right)^{1/2}{\rm mJy}\,. \quad (38)$$

We then perform a sensitivity analysis where we look for the parameter space where the flux density emitted by the axion-photon conversion in Eq. 35 is larger than the sensitivity levels of LOFAR in Eq. 38, with typical observation time of 8 hours.

The results are shown in Fig. 3. The red region is the range of PBH and QCD axion masses where the signal can in principle be detected at LOFAR with a dedicated analysis. In the innermost part of the red region, the flux density is rather large and the signal can be detected with high significance. In each plot, the red region is enclosed by the blue band which corresponds to the range of parameters where the emitted photons lie in the frequency band of the LOFAR low-band array while satisfying the superradiant constraints as in Fig. 2. Inside the gray region, the electrons in the plasma are relativistic at the conversion point and so outside the range of validity of the expressions we used.

In the analysis, we fixed the velocity parameter to $v = 10$ km/s and the PBH fraction to $f_{\rm PBH} = 0.1$. We have also chosen an angle between the line of sight and the rotation axis of the BH of $\pi/2$ but showed the results for another representative value of $\pi/8$ (dot-dashed curve). We then considered two different values of the medium density, $n_\infty = 0.5\,{\rm cm}^{-3}$ and $0.2\,{\rm cm}^{-3}$, typical of the warm ionized medium, and two different values of the initial PBH spin, $\tilde{a} = 0.1$ and close to 1. Note that by decreasing $\tilde{a}$ the superradiant condition $\alpha < \tilde{a}/2$ becomes stronger and therefore the allowed parameter space is smaller. In particular, for $\tilde{a} = 0.01$ the parameter space is too narrow and there is no detectable region.

The red region in Fig. 3 corresponds to PBH masses around $10^{-5} - 10^{-4}\ M_\odot$. Coincidently, this range of PBH masses is within the range that can explain the ultra-short-timescale microlensing events measured by the OGLE experiment (see Fig. 8 of [27]).

VI. DISCUSSION AND OUTLOOK

The main outcome of this work was to show that the QCD axion can illuminate the vicinity of PBH with subsolar masses and that if the latter amounts to $1 - 10\%$ of the total dark matter abundance the resulting signals could be detected at radio telescopes such as LOFAR.

The mechanism relied on two main ingredients, superradiance and the accretion onto the PBH. On one hand, the superradiant instability dynamically creates a dense cloud of axions around the PBH and therefore our results do not assume an initial QCD axion profile. On the other hand, the accretion of the interstellar medium ensures the presence of a critical radius, where the QCD axion mass and the effective plasma mass are equal, and therefore where the resonant conversion can occur. As explained in section III, we used a model of Bondi accretion and assumed that the plasma behaves non-relativistically in the relevant region for the axion-photon conversion. This condition is fulfilled far away from the Schwarzschild radius, which allowed us to also neglect gravitational corrections.

To compute the luminosity that results from the conversion, we considered in section IV a Klein-Gordon-like equation for the component of the photon field parallel to the external magnetic field, which is the one that interacts with the QCD axion. For simplicity, we assumed this magnetic field to be perpendicular to the line of sight in the relevant region for the conversion, and neglected ray-bending effects. We also neglected self-interactions and backreaction in the QCD axion cloud. The former is justified by the fact that we restricted to subsolar PBHs with masses such that self-interactions are only relevant above the QCD axion line [20]; the latter because of the restriction to non-relativistic plasmas at the conversion point that enforces that the interesting magnetically stimulated regime that we discuss in Appendix E, where the produced magnetic fields are larger than the original ones, does not happen.

In solving the photon equation for finding the luminosity of the system we solved the second-order photon equation instead of reducing it to a first-order one, which is common practice in the literature. We found that, under two simplifying assumptions that hold in the most efficient part of the allowed parameter space, i.e. when the critical point and the most populated part of the superradiant cloud are not far from each other, most photons are produced around the critical radius. These simplifications, also allowed us to arrive at an analytical expression for the luminosity in Eq. 29 that is similar to that in the axion-photon conversion literature.

The resulting luminosity of the process was shown in Fig. 2 for different interstellar media. In the conservative region of the parameter space, we found luminosities as high as 10^{12} W for an accretion from the warm ionized medium. These high luminosities confirmed our hypothesis: even if the magnetic field in the ISM is very weak when compared with the magnetic fields around neutron stars or magnetars, this is highly compensated by the huge amount of QCD axions generated by superradiance.

Finally, in section V we studied the possibility of directly detecting the emitted electromagnetic signals with existing radio telescopes. We considered the low band antenna of the LOFAR telescope, which is the one with the best sensitivity in the conservative region of our parameter space, and found that PBHs and QCD axions in the mass range between $10^{-5} - 10^{-4}\,M_\odot$ and $4 \times 10^{-7} - 4 \times 10^{-8}$, respectively, could potentially be detected (see Fig 3). Interestingly, this region coincides with the range of PBH masses used in [27] to explain some microlensing events observed by the OGLE experiment. This is a clear motivation to look for further evidence in the LOFAR data.

This work has left a few interesting avenues that we believe will be interesting to pursue in more detail in the future. We focused on the possibility of directly detecting the light coming from the closest PBH but it would be interesting to study the stochastic signal that would be produced by the cosmological PBH population. It would also be interesting to extend the results to accretion models that account for angular momentum as the advection-dominated accretion flow [51], and to explore the possibility of large magnetic fields via the Blandford instability [43]. On the other hand, although we have restricted to cases where the plasma is non-relativistic around the conversion radius, we do not expect significant changes in the plasma mass in the relativistic case and therefore the prospects that we find in this work likely extend to the relativistic region. Moreover, this would allow signals at larger frequencies that could be probed at other radio telescopes. Finally, the methods we developed are directly extensible to axion-like particles (ALPs), which opens up the parameter space since the mass and the coupling are not correlated.

VII. ACKNOWLEDGEMENTS

We would like to thank Erik Engstedt for participation in the early stages of this project and M.C. David Marsh and João Rosa for discussions. R.Z.F. acknowledges the financial support provided through national funds by FCT - Fundação para a Ciência e Tecnologia, I.P., reference 2022.03283.CEECIND as well as the FCT projects CERN/FIS-PAR/0027/2021, UIDB/04564/2020 and UIDP/04564/2020, with DOI identifiers 10.54499/CERN/FIS-PAR/0027/2021, 10.54499/UIDB/04564/2020 and 10.54499/UIDP/04564/2020, respectively. Á.G.M. has been supported by the Secretariat for Universities and Research of the Ministry of Business and Knowledge of the Government of Catalonia and the European Social Fund. Á.G.M. acknowledges the support from the Departament de Recerca i Universitats from Generalitat de Catalunya to the Grup de Recerca 'Grup de Física Teòrica UAB/IFAE' (Codi: 2021 SGR 00649). IFAE is partially funded by the CERCA program of the Generalitat de Catalunya.

Appendix A: Components of the interstellar medium

Table 1: Components of the interstellar medium and reference values for some of their properties. Adapted from [30, 32, 42, 69].

Component	Temperature (**K**)	Density (cm^{-3})	Sound speed (km/sec)	Ionized fraction x_e
Molecular clouds	$10-50$	10^2-10^6	0.6	$10^{-7}-10^{-4}$
Cold neutral medium (CNM)	100	30	10	10^{-3}
Warm neutral medium (WNM)	5000	$0.2-0.5$	10	0.1
Warm ionized medium (WIM)	10^4	$0.2-0.5$	10	1
Hot ionized medium (HIM)	10^6	$10^{-3}-10^{-2}$	100	1

(A1)

Appendix B: Method of variation of parameters

In this appendix, we provide the details that allowed us to arrive at the asymptotic solution for the field $A(t,\vec{r})$ in Eq. 25 using the method of variation of parameters. Starting from Eq. 24

$$\left(-m_a^2-\nabla^2+\omega_p^2(r)\right)A(\vec{r})=f(\vec{r})\,, \tag{B1}$$

and after decomposing the source $f(\vec{r})$ and $A(\vec{r})$ in spherical harmonics, we arrive at:

$$\partial_r^2(rA_{lm}(r))+\left[m_a^2-\omega_p^2(r)-\frac{l(l+1)}{r^2}\right](rA_{lm}(r))=-rf_{lm}(r) \tag{B2}$$

where $A_{lm}(r)$, $f_{lm}(r)$ are respectively the projections of the field and the source over the harmonics.

Since $\omega_{p,\infty}$ is a non-zero constant, the homogeneous solutions of Eq. (B2) are $F_l(r)$, $G_l(r)$ [6] such that $F_l(r\to\infty)\to\cos(\theta_l(k_\infty r))$ and $G_l(r\to\infty)\to\sin(\theta_l(k_\infty r))$, with $k_\infty^2=m_a^2-\omega_{p,\infty}^2$, where $\partial_r\theta_l\to k_\infty$ when $r\to\infty$. For convenience, in the following, we choose F_l and $H_l(r)=F_l(r)+iG_l(r)$ as the pair of independent solutions. Then, the particular solution of B1 can be written as

$$A_{lm}(r)=\frac{F_l(r)}{r}\int_r^\infty\frac{r'f_{lm}(r')}{W(F_l,H_l)}H_l(r')\,dr'\;+\;\frac{H_l(r)}{r}\int_0^r\frac{r'f_{lm}(r')}{W(F_l,H_l)}F_l(r')\,dr' \tag{B3}$$

[6] Eq. (B2) does not depend on the angular number m, so for each mode the homogeneous solutions depend only on l.

where $W(F_l, H_l) = F_l(r)H_l'(r) - F_l'(r)H_l(r)$ is the Wronskian operator. The constant limits of integration are arbitrary; here they have been chosen to fix initial conditions. For $r \to \infty$, we fixed the solution to behave like $H_l(r)/r = e^{i\theta_l(r)}/r$, and for $r \sim 0$ as $F_l(r)/r$. The choice of F_l rather than G_l is related to the fact that, as can be seen in the next appendix, $\lim_{r\to 0} F_l(r) = 0$; this is a sensible initial condition since in our setup the plasma mass is very large at small radii and the conversion into photons becomes kinematically forbidden.

In general, the Wronskian for two solutions ϕ_1, ϕ_2 of a second order differential homogeneous equation without first-order term $\phi_{1,2}''(r) + p(r)\phi_{1,2}(r) = 0$, like Eq. (B2), is constant. Using this together with the fact that the Wronskian is a multilinear operator, we can find its value to be:

$$W(F_l, H_l) = iW(F_l, G_l) \to iW(\cos\theta_l(k_\infty r), \sin\theta_l(k_\infty r)) = ik_\infty\,. \tag{B4}$$

In the end, we are interested in the luminosity at infinity, so we substitute the asymptotic expressions in Eq. (B3) and find

$$A_{lm}(r\to\infty) = \frac{e^{i\theta_l(k_\infty r)}}{ik_\infty r}\int_0^\infty r' f_{lm}(r')F_l(r')\,dr'\,. \tag{B5}$$

The asymptotic expression for the photon field is $A(\vec{r}) = \sum_{lm} Y_{lm}(\hat{r})A_{lm}$. In our case, the source only has non-vanishing contributions for $l = m = 1$, so the asymptotic expression further simplifies to

$$A(\vec{r}) \to Y_{11}(\hat{r})\frac{e^{i\theta_l(k_\infty r)}}{ik_\infty r}\int_0^\infty r' f_{lm}(r')F_l(r')\,dr' \tag{B6}$$

with radial derivative $\partial_r A(\vec{r}) = ik_\infty A(\vec{r})$, where we used that $\partial_r\theta_l(kr) \to k$ and neglected terms proportional to $1/r^2$.

Appendix C: Solution of the homogeneous equation

In appendix B we derived the general formula for the luminosity in terms of a convolution of the homogenous solution of the differential equation with the source term. Now we proceed with the derivation of the homogeneous solution $F_l(r)$ of Eq. B2. We start by rewriting the differential equation in terms of the adimensional parameter $\rho = m_a r$ as

$$\partial_\rho^2(F(\rho)) + \tilde{k}(\rho)^2 F(\rho) = 0 \tag{C1}$$

where $\tilde{k}(\rho)^2 = 1 - (\rho_{\rm crit}/\rho)^{3/2}$ is the effective momentum in units of m_a, we neglected the small angular momentum contribution (and for that reason we drop the subindex l) and defined $\rho_{\rm crit} \equiv m_a r_{\rm crit}$.

We can now use the WKB method to find the solution of the equation of motion for both large $\rho > \rho_{\rm crit}$ and small $\rho < \rho_{\rm crit}$. In the intermediate region, $\rho \sim \rho_{\rm crit}$, where the WKB approximation does not hold, we will instead Taylor expand the effective momentum $\tilde{k}$ and look for exact solutions that we then match to the WKB regimes for large and small ρ.

a. $\rho > \rho_{crit}$*:* When $\rho > \rho_{\rm crit}$ the general WKB solution is given by

$$F(\rho) = \sqrt{\frac{1}{\tilde{k}(\rho)}}\left(a_1\cos\left[\int_{\rho_{\rm crit}}^\rho \tilde{k}(\rho')d\rho' - \pi/4\right] + a_2\sin\left[\int_{\rho_{\rm crit}}^\rho \tilde{k}(\rho')d\rho' - \pi/4\right]\right), \qquad \rho > \rho_{\rm crit}. \tag{C2}$$

The lower limit of integration and the $\pi/4$ phase are taken for convenience. In app. B we required $F(\rho) \to \cos(\theta(kr))$ as $r \to \infty$, so we need to set $a_2 = 0$ and $a_1 = \sqrt{\tilde{k}_\infty}$.[7]

b. $|\rho - \rho_{crit}| \ll \tilde{L}^2/(2\pi)$*:* The WKB approximation breaks down around the resonant point $\rho = \rho_{\rm crit}$. To find a solution in this regime we Taylor expand $\tilde{k}(\rho)$ around $\rho_{\rm crit}$ to first order,

$$\tilde{k}(\rho)^2 \sim \frac{2\pi}{\tilde{L}^2}(\rho - \rho_{\rm crit}) \tag{C3}$$

[7] Actually, F is an exact solution of C1 for $\rho > \rho_b$ where ρ_b is the value of ρ at the Bondi radius where the momentum approaches a constant, $\tilde{k} \to k_\infty/m_a$.

where $\tilde{L} = m_a\sqrt{\pi/\omega_p'(\rho_{\rm crit})} = \sqrt{4\pi\rho_{\rm crit}/3}$ is the width of the critical region in units of m_a (the derivative is taken with respect to r). We then obtain the differential equation:

$$\partial_\rho^2(F(\rho)) + \frac{2\pi}{\tilde{L}^2}(\rho - \rho_{\rm crit})F(\rho) = 0 \tag{C4}$$

whose solutions are Airy functions

$$F(\rho) = b_1\ \text{AiryAi}\left[\left(\frac{\tilde{L}^2}{2\pi}\right)^{-1/3}(\rho_{\rm crit}-\rho)\right] + b_2\ \text{AiryBi}\left[\left(\frac{\tilde{L}^2}{2\pi}\right)^{-1/3}(\rho_{\rm crit}-\rho)\right], \qquad |\rho-\rho_{\rm crit}| \ll \tilde{L}^2/(2\pi) \tag{C5}$$

and b_1, b_2 are integration constants.

To find these constants we match the solutions for F in the overlapping region of validity of both branches which is when $\tilde{L}^2/(2\pi) \gg \rho - \rho_{\rm crit} \gg \left(\tilde{L}^2/(2\pi)\right)^{1/3}$. Namely, the Taylor expansion of $\tilde{k}(\rho)^2$ in C2 yields

$$F(\rho) \sim \sqrt{\tilde{k}_\infty}\left(\frac{\tilde{L}^2}{2\pi}\right)^{1/4}(\rho-\rho_{\rm crit})^{-1/4}\cos\left[\frac{2\sqrt{2\pi}}{3\tilde{L}}(\rho_{\rm crit}-\rho)^{3/2} - \pi/4\right], \tag{C6}$$

which we then match to the asymptotic expansion of Eq. C5 for $\rho \gg \rho_{\rm crit}$

$$F(\rho) \simeq \sqrt{\pi}\left(\frac{\tilde{L}^2}{2\pi}\right)^{1/12}(\rho-\rho_{\rm crit})^{-1/4}\left(b_1\cos\left[\frac{2\sqrt{2\pi}}{3\tilde{L}}(\rho_{\rm crit}-\rho)^{3/2}-\pi/4\right] - b_2\sin\left[\frac{2\sqrt{2\pi}}{3\tilde{L}}(\rho_{\rm crit}-\rho)^{3/2}-\pi/4\right]\right) \tag{C7}$$

to find $b_2 = 0$ and $b_1 = \sqrt{\pi\tilde{k}_\infty}(\tilde{L}^2/(2\pi))^{1/6}$.

c. $\rho < \rho_{crit}$: Finally, we look at the region where $\rho < \rho_{\rm crit}$. The general WKB solution is

$$F(\rho) = \frac{1}{\sqrt{|\tilde{k}(\rho)|}}\left(c_1\ \text{Exp}\left[\int_0^\rho |\tilde{k}(\rho')|d\rho'\right] + c_2\ \text{Exp}\left[-\int_0^\rho |\tilde{k}(\rho')|d\rho'\right]\right), \qquad \rho < \rho_{\rm crit}\,. \tag{C8}$$

The integration limits were chosen for convenience, and c_1, c_2 are integration constants that we again fix by matching Eqs. C5 and C8 in the common region of validity, i.e. $\tilde{L}^2/(2\pi) \gg \rho_{\rm crit} - \rho \gg \left(\tilde{L}^2/(2\pi)\right)^{1/3}$. Namely, we match the expansion of Eq. C5 for $\rho_{\rm crit} - \rho \gg \left(\tilde{L}^2/(2\pi)\right)^{1/3}$

$$F(\rho < \rho_{\rm crit}) \to \frac{\sqrt{\tilde{k}_\infty}}{2}\left(\frac{\tilde{L}^2}{2\pi}\right)^{1/4}(\rho_{\rm crit}-\rho)^{-1/4}\text{Exp}\left[\frac{-2\sqrt{2\pi}}{3\tilde{L}}(\rho_{\rm crit}-\rho)^{3/2}\right], \tag{C9}$$

where we used the values of b_1, b_2 found before, with the Taylor expansion of Eq. C8 close to the critical radius, $|\tilde{k}(\rho)| \sim \left(\frac{2\pi}{\tilde{L}^2}(\rho_{\rm crit}-\rho)\right)^{1/2}$,

$$F(\rho < \rho_{\rm crit}) \sim c_1\left(\frac{\tilde{L}^2}{2\pi}\right)^{1/4}(\rho_{\rm crit}-\rho)^{-1/4}C^{-1}\text{Exp}\left[\frac{-2\sqrt{2\pi}}{3\tilde{L}}(\rho_{\rm crit}-\rho)^{3/2}\right], \tag{C10}$$

where c_2 was fixed to zero and

$$C \equiv \text{Exp}\left[-\int_0^{\rho_{\rm crit}}|\tilde{k}(\rho')|d\rho'\right] = \text{Exp}\left[-\frac{2\sqrt{\pi}\Gamma(7/6)}{\Gamma(5/3)}\rho_{\rm crit}\right], \tag{C11}$$

and find $c_1 = C\sqrt{\tilde{k}_\infty}/2$. Note that $\lim_{\rho\to 0}F(\rho) = 0$, consistently to what we imposed in Appendix B. [8]

[8] The WKB approximation breaks down when $\rho \sim 0$. In that limit, the exact solution, which can be found exactly using $\tilde{k}^2 \sim (\rho_{\rm crit}/\rho)^{3/2}$, is a Bessel function that also fulfills the requirements of F_ρ.

We can now put all the solutions together to find the complete solution for $F(\rho)$

$$F(\rho) = \begin{cases} \frac{C}{2}\sqrt{\frac{\tilde{k}_\infty}{|\tilde{k}(\rho)|}}\ \mathrm{Exp}\left[\int_0^\rho |\tilde{k}(\rho')|d\rho'\right] & , \rho < \rho_{\rm crit} \\ \sqrt{\pi\tilde{k}_\infty}(2\pi)^{-1/6}\tilde{L}^{1/3}\mathrm{AiryAi}\left((2\pi)^{1/3}\tilde{L}^{-2/3}(\rho_{\rm crit}-\rho)\right) & , |\rho-\rho_{\rm crit}| \ll \tilde{L}^2/(2\pi) \\ \sqrt{\frac{\tilde{k}_\infty}{\tilde{k}(\rho)}}\cos\left[\int_{\rho_{\rm crit}}^\rho \tilde{k}(\rho')d\rho' - \pi/4\right] & , \rho > \rho_{\rm crit} \end{cases} \tag{C12}$$

Appendix D: Analytical computation of the luminosity

In this appendix, we derive a simplified formula for the photon luminosity that results from the axion to photon conversion and elaborate under which conditions the formula applies. From Eqs. 25 and 27, the expression for the luminosity emitted per solid angle is

$$\left\langle \frac{dP}{d\Omega} \right\rangle = |Y_{11}(\hat{r})|^2\ \frac{m_a^2}{k_\infty} g_{a\gamma\gamma}^2 N \left| \int B(r')R_{21}(r')F(r')r'dr' \right|^2 . \tag{D1}$$

For $\rho < \rho_{\rm crit}$ (recall that $\rho = m_a r$) the homogenous solution $F(r)$ is exponentially suppressed if $\rho_{\rm crit} \gg 1$, so we can neglect this contribution to the integral. Similarly, the region $\rho > \rho_{\rm crit}$ can be neglected due to the highly oscillatory behavior of $F(r)$. Therefore, the main contribution to the luminosity comes from the region $|\rho - \rho_{\rm crit}| \ll \tilde{L}^2/(2\pi)$, i.e. from the region around the resonance $m_a \simeq \omega_p(r_{\rm crit})$. [9]

However, we can further simplify the integral by noting, as we will do next, that in the cases of interest most of its support is in an even smaller window of size proportional to $\tilde{L}^{2/3}$ which is parametrically smaller than the typical scale of variability of $g(\rho) \equiv B(\rho)R_{21}(\rho)\rho$ around $\rho_{\rm crit}$ which is

$$\left| \frac{g'(\rho_{\rm crit})(\rho - \rho_{\rm crit})}{g(\rho_{\rm crit})} \right| < 1 \iff |\rho - \rho_{\rm crit}| < \frac{4\rho_{\rm crit}}{|3 - 2\alpha\rho_{\rm crit}|} . \tag{D2}$$

To verify that, we will approximate $g(\rho) \sim const.$ and then check by inspection under what conditions the remaining integral has most of its support in a region smaller than Eq. D2. Following these steps, we find that

$$\int_{\rho_0}^{\rho_f} F(\rho')d\rho' = \sqrt{\frac{\tilde{k}_\infty}{2}}\tilde{L}\left[1 - \frac{1}{2\sqrt{\pi}(c\Delta_0)^{3/4}}e^{-2(c\Delta_0)^{3/2}/3} + \frac{1}{\sqrt{\pi}(c\Delta_f)^{3/4}}\sin\left(\frac{\pi}{4} - \frac{2}{3}(c\Delta_f)^{3/2}\right)\right] \tag{D3}$$

where $c = (3\rho_{\rm crit}^2/2)^{1/3}$, $\Delta_0 = (1 - \rho_0/\rho_{\rm crit})$, $\Delta_f = (\rho_f/\rho_{\rm crit} - 1)$. Whenever $c\Delta_0, c\Delta_f \gg 1$ or, correspondingly, when the integration window is $|\rho_f - \rho_0| \gg \rho_{\rm crit}^{1/3} = (3\tilde{L}^2/(4\pi))^{1/3}$, the integral becomes insensitive to the integration limits and simplifies to

$$\int_{\rho_0}^{\rho_f} F(\rho')d\rho' = \sqrt{\frac{\tilde{k}_\infty}{2}}\tilde{L} . \tag{D4}$$

Therefore, the support of the integral is inside the region in Eq. D2 where the function $g(\rho)$ is approximately constant, if

$$\left| \frac{4\rho_{\rm crit}}{3 - 2\alpha\rho_{\rm crit}} \right| \gtrsim \rho_{\rm crit}^{1/3} . \tag{D5}$$

If this condition, together with $\rho_{\rm crit} > 1$, is fulfilled, then we can further simplify Eq. D1 and find

$$\left\langle \frac{dP}{d\Omega} \right\rangle = |Y_{11}(\hat{r})|^2\ \frac{m_a^2}{k_\infty} g_{a\gamma\gamma}^2 B_{\rm crit}^2 N R_{21}(r_{\rm crit})^2 r_{\rm crit}^2 \left| \int F(r')dr' \right|^2 \simeq m_a\ n_{\rm crit}\ r_{\rm crit}^2 \frac{(L\ g_{a\gamma\gamma}\ B_{\rm crit})^2}{2} \tag{D6}$$

[9] Numerically we verified that for $\rho_{\rm crit} \gtrsim 5$ and α within the range of interest, the region around the resonance dominates over the others.

where he have defined $n_{\rm crit} = N R_{21}(r_{\rm crit})^2$ and used Eq. D4. Interestingly, this last term is reminiscent of the standard expression for the axion-photon conversion probability [57]. This might not be surprising as we have concluded that the magnetic field and the axion cloud are approximately constant in the conversion region and therefore the conversion becomes closer to the more standard processes studied in the literature.

Note that the fact that the luminosity at infinity does not depend on the momentum at infinity can be counter-intuitive. However, one should take into account that the energy released at conversion is fixed: the evolution in the plasma mass afterward does not change the flux. Taking the particle perspective, a change in the photon mass can be understood as a change in the number of photons. Conservation of energy implies that the energy flux is the same.

Appendix E: Magnetic stimulation and cloud quenching

The photons converted from the axion cloud will themselves generate an electric and magnetic field. When this new induced magnetic field $B_{\rm ind}$ becomes comparable

$$\langle |B_{\rm ind}(r)|^2 \rangle \sim B^2(r) \tag{E1}$$

with the background interstellar magnetic field B that generated the axion-to-photon conversion in the first place (the brackets denote a time-average) the system is expected to enter a *magnetically stimulated* stage where the conversion rate could grow very fast, in a snowball effect, analogously to other stimulation effects that have been studied in the literature (e.g. [22, 23, 55]) even though here the process is initially linear, one axion converts to one photon.

To understand the region of parameters where this might happen we estimate the induced magnetic field as

$$\langle |B_{\rm ind}(r)|^2 \rangle = \left| \frac{2}{r} \partial_r \left(r A \right) \right|^2 \sim \frac{a_0^{-3} \tilde{n}_{\rm crit}}{2} \frac{k(r)^2}{k_\infty^2} \left(g_{a\gamma\gamma} B(r) L \right)^2 \tag{E2}$$

where we have used the fact that the conversion is highly dominated by the dynamics around the critical radius, and therefore the field $A(t, \vec{r})$ will behave like Eq. 25 shortly after that point, and assumed Eq. 29 to be satisfied.

The maximum value of the previous expression takes place at the maximum of $k(x)^2/x^2$ is, with $x = \rho/\rho_{\rm crit}$, and turns out to be $\simeq 0.2$, at $\rho \simeq 1.45 \rho_{\rm crit}$. Then, to be sure that the stimulated resonance does not occur, we impose

$$\max \left[\frac{\langle |B_{\rm ind}|^2 \rangle}{B^2} \right] = \frac{0.2 m_a^5}{k_\infty} \frac{(g_{a\gamma\gamma} L)^2}{2} \tilde{n}_{\rm crit} \big|_{\theta = \pi/2} < 1 \tag{E3}$$

where we chose an angle of $\pi/2$ since $|Y_{11}|^2$ is maximized in that direction. Note that if the radius at which the ratio is maximized lies outside the relevant interval for conversion, the axion-photon conversion might not be affected by the magnitude of $|B_{\rm ind}|^2$. For this reason, Eq. E3 is not an exact characterization of the magnetic stimulation, but rather a conservative bound to ensure that such stimulation does not occur.

Although this regime might be the one leading to the largest observable signatures, as it might lead to an explosion of the cloud into photons, to have a robust understanding of what happens beyond the threshold of magnetic stimulation we would need to backreact the effect of the cloud on the dynamics of the accretion. Moreover, this constraint is weaker than that coming from imposing the electrons to be non-relativistic at the conversion radius. Therefore, we conservatively discard it in the main text.

[1] G. G. Raffelt, Astrophysical axion bounds, Lect. Notes Phys. **741**, 51 (2008), arXiv:hep-ph/0611350.

[2] P. Carenza, T. Fischer, M. Giannotti, G. Guo, G. Martínez-Pinedo, and A. Mirizzi, Improved axion emissivity from a supernova via nucleon-nucleon bremsstrahlung, JCAP **10** (10), 016, [Erratum: JCAP 05, E01 (2020)], arXiv:1906.11844 [hep-ph].

[3] M. Buschmann, C. Dessert, J. W. Foster, A. J. Long, and B. R. Safdi, Upper Limit on the QCD Axion Mass from Isolated Neutron Star Cooling, Phys. Rev. Lett. **128**, 091102 (2022), arXiv:2111.09892 [hep-ph].

[4] A. Hook, Y. Kahn, B. R. Safdi, and Z. Sun, Radio signals from axion dark matter conversion in neutron star magnetospheres, Phys. Rev. Lett. **121**, 241102 (2018).

[5] A. J. Millar, S. Baum, M. Lawson, and M. C. D. Marsh, Axion-photon conversion in strongly magnetised plasmas, JCAP **11**, 013, arXiv:2107.07399 [hep-ph].

[6] S. J. Witte, D. Noordhuis, T. D. P. Edwards, and C. Weniger, Axion-photon conversion in neutron star magnetospheres: The role of the plasma in the Goldreich-Julian model, Phys. Rev. D **104**, 103030 (2021), arXiv:2104.07670 [hep-ph].

[7] R. A. Battye, B. Garbrecht, J. I. McDonald, F. Pace, and S. Srinivasan, Dark matter axion detection in the radio/mm-waveband, Phys. Rev. D **102**, 023504 (2020), arXiv:1910.11907 [astro-ph.CO].

[8] J. W. Foster, S. J. Witte, M. Lawson, T. Linden, V. Gajjar, C. Weniger, and B. R. Safdi, Extraterrestrial Axion Search with the Breakthrough Listen Galactic Center Survey, Phys. Rev. Lett. **129**, 251102 (2022), arXiv:2202.08274 [astro-ph.CO].

[9] C. Dessert, D. Dunsky, and B. R. Safdi, Upper limit on the axion-photon coupling from magnetic white dwarf polarization, Phys. Rev. D **105**, 103034 (2022), arXiv:2203.04319 [hep-ph].

[10] A. Caputo, S. J. Witte, A. A. Philippov, and T. Jacobson, Pulsar nulling and vacuum radio emission from axion clouds (2023), arXiv:2311.14795 [hep-ph].

[11] B. R. Safdi, Z. Sun, and A. Y. Chen, Detecting axion dark matter with radio lines from neutron star populations, Physical Review D **99**, 10.1103/physrevd.99.123021 (2019).

[12] F. P. Huang, K. Kadota, T. Sekiguchi, and H. Tashiro, Radio telescope search for the resonant conversion of cold dark matter axions from the magnetized astrophysical sources, Physical Review D **97**, 10.1103/physrevd.97.123001 (2018).

[13] M. Leroy, M. Chianese, T. D. Edwards, and C. Weniger, Radio signal of axion-photon conversion in neutron stars: A ray tracing analysis, Physical Review D **101**, 10.1103/physrevd.101.123003 (2020).

[14] S. A. Teukolsky, Rotating black holes: Separable wave equations for gravitational and electromagnetic perturbations, Phys. Rev. Lett. **29**, 1114 (1972).

[15] V. Cardoso, O. J. Dias, J. P. Lemos, and S. Yoshida, The Black hole bomb and superradiant instabilities, Phys. Rev. D **70**, 044039 (2004).

[16] W. E. East and F. Pretorius, Superradiant Instability and Backreaction of Massive Vector Fields around Kerr Black Holes, Phys. Rev. Lett. **119**, 041101 (2017), arXiv:1704.04791 [gr-qc].

[17] C. A. R. Herdeiro, E. Radu, and N. M. Santos, A bound on energy extraction (and hairiness) from superradiance, Phys. Lett. B **824**, 136835 (2022), arXiv:2111.03667 [gr-qc].

[18] A. Arvanitaki, M. Baryakhtar, and X. Huang, Discovering the qcd axion with black holes and gravitational waves, Phys. Rev. D **91**, 084011 (2015).

[19] A. Arvanitaki, M. Baryakhtar, S. Dimopoulos, S. Dubovsky, and R. Lasenby, Black hole mergers and the qcd axion at advanced ligo, Phys. Rev. D **95**, 043001 (2017).

[20] M. Baryakhtar, M. Galanis, R. Lasenby, and O. Simon, Black hole superradiance of self-interacting scalar fields, Phys. Rev. D **103**, 095019 (2021), arXiv:2011.11646 [hep-ph].

[21] V. M. Mehta, M. Demirtas, C. Long, D. J. E. Marsh, L. Mcallister, and M. J. Stott, Superradiance Exclusions in the Landscape of Type IIB String Theory, (2020), arXiv:2011.08693 [hep-th].

[22] J. G. Rosa and T. W. Kephart, Stimulated axion decay in superradiant clouds around primordial black holes, Phys. Rev. Lett. **120**, 231102 (2018).

[23] T. Ikeda, R. Brito, and V. Cardoso, Blasts of light from axions, Phys. Rev. Lett. **122**, 081101 (2019).

[24] A. Arvanitaki, S. Dimopoulos, S. Dubovsky, N. Kaloper, and J. March-Russell, String axiverse, Phys. Rev. D **81**, 123530 (2010).

[25] A. Arvanitaki and S. Dubovsky, Exploring the string axiverse with precision black hole physics, Phys. Rev. D **83**, 044026 (2011).

[26] M. P. van Haarlem *et al.*, LOFAR: The LOw-Frequency ARray, Astron. Astrophys. **556**, A2 (2013), arXiv:1305.3550 [astro-ph.IM].

[27] H. Niikura, M. Takada, S. Yokoyama, T. Sumi, and S. Masaki, Constraints on Earth-mass primordial black holes from OGLE 5-year microlensing events, Phys. Rev. D **99**, 083503 (2019), arXiv:1901.07120 [astro-ph.CO].

[28] S. Detweiler, Klein-gordon equation and rotating black holes, Phys. Rev. D **22**, 2323 (1980).

[29] L. Di Luzio, M. Giannotti, E. Nardi, and L. Visinelli, The landscape of QCD axion models, Phys. Rept. **870**, 1 (2020), arXiv:2003.01100 [hep-ph].

[30] B. T. Draine, *Physics of the interstellar and intergalactic medium* (Princeton University Press, 2010).

[31] T. Dalton, S. L. Morris, M. Fumagalli, and E. Gatuzz, Probing the physical properties of the intergalactic medium using blazars, Mon. Not. Roy. Astron. Soc. **508**, 1701 (2021), arXiv:2109.06632 [astro-ph.HE].

[32] K. M. Ferrière, The interstellar environment of our galaxy, Rev. Mod. Phys. **73**, 1031 (2001).

[33] J. Xu and J. L. Han, Magnetic fields in the solar vicinity and in the Galactic halo, Monthly Notices of the Royal Astronomical Society **486**, 4275 (2019).

[34] V. Pelgrims, K. Ferrière, F. Boulanger, R. Lallement, and L. Montier, Modeling the magnetized Local Bubble from dust data, aap **636**, A17 (2020), arXiv:1911.09691 [astro-ph.GA].

[35] V. D. Luca, G. Franciolini, P. Pani, and A. Riotto, The evolution of primordial black holes and their final observable spins, Journal of Cosmology and Astroparticle Physics **2020** (04), 052–052.

[36] J. R. Chisholm, S. Dodelson, and E. W. Kolb, Stellar-Mass Black Holes in the Solar Neighborhood, Astrophys. J. **596**, 437 (2003), arXiv:astro-ph/0205138.

[37] R. P. Fender, T. J. Maccarone, and I. Heywood, The closest black holes, Mon. Not. Roy. Astron. Soc. **430**, 1538 (2013).

[38] H. Bondi, On Spherically Symmetrical Accretion, Mon. Not. Roy. Astron. Soc. **112**, 195 (1952).

[39] J. R. Ipser and R. H. Price, Accretion onto pregalactic black holes., Astrophys. J. **216**, 578 (1977).

[40] S. L. Shapiro, A. P. Lightman, and D. M. Eardley, A two-temperature accretion disk model for Cygnus X-1: structure and spectrum., Astrophys. J. **204**, 187 (1976).

[41] J. Manshanden, D. Gaggero, G. Bertone, R. M. Connors, and M. Ricotti, Multi-wavelength astronomical searches for primordial black holes, J. Cosmol. Astropart. Phys. **2019**, 026–026 (2019).

[42] K. Ioka, T. Matsumoto, Y. Teraki, K. Kashiyama, and K. Murase, GW 150914-like black holes as Galactic high-energy sources, Mon. Not. Roy. Astron. Soc. **470**, 3332 (2017), arXiv:1612.03913 [astro-ph.HE].

[43] R. D. Blandford and R. L. Znajek, Electromagnetic extractions of energy from Kerr black holes, Mon. Not. Roy. Astron. Soc. **179**, 433 (1977).

[44] G. S. Bisnovatyi-Kogan and A. A. Ruzmaikin, The Accretion of Matter by a Collapsing Star in the Presence of a Magnetic Field. II: Self-consistent Stationary Picture, pass **42**, 401 (1976).

[45] V. F. Shvartsman, Halos around "black holes"., Soviet astron. **15**, 377 (1971).

[46] G. Beskin and S. Karpov, Low-rate accretion onto isolated stellar mass black holes, Astron. Astrophys. **440**,

223 (2005).
[47] J. R. Ipser and R. H. Price, Synchrotron radiation from spherically accreting black holes, Astrophys. J. **255**, 654 (1982).
[48] K. Akiyama, A. Alberdi, W. Alef, K. Asada, and R. Azulay (Event Horizon Telescope collaboration), First M87 event horizon telescope results. v. physical origin of the asymmetric ring, Astrophys. J. Lett. **875**, L5 (2019).
[49] K. Akiyama *et al.* (Event Horizon Telescope), First M87 Event Horizon Telescope Results. VIII. Magnetic Field Structure near The Event Horizon, Astrophys. J. Lett. **910**, L13 (2021), arXiv:2105.01173 [astro-ph.HE].
[50] M. Colpi, L. Maraschi, and A. Treves, Two-temperature model of spherical accretion onto a black hole., Astrophys. J. **280**, 319 (1984).
[51] R. Mahadevan and E. Quataert, Are particles in advection-dominated accretion flows thermal?, Astrophys. J. **490**, 605 (1997).
[52] F. Yuan and R. Narayan, Hot accretion flows around black holes, Annu. Rev. Astron. Astrophys. **52**, 529 (2014).
[53] A. Caputo, S. J. Witte, D. Blas, and P. Pani, Electromagnetic signatures of dark photon superradiance (2021).
[54] D. Blas and S. J. Witte, Quenching mechanisms of photon superradiance, Phys. Rev. D **102**, 123018 (2020).
[55] D. Blas and S. J. Witte, Imprints of axion superradiance in the cmb, Phys. Rev. D **102**, 103018 (2020).
[56] N. P. Branco, R. Z. Ferreira, and J. a. G. Rosa, Superradiant axion clouds around asteroid-mass primordial black holes, JCAP **04**, 003, arXiv:2301.01780 [hep-ph].
[57] G. Raffelt and L. Stodolsky, Mixing of the Photon with Low Mass Particles, Phys. Rev. D **37**, 1237 (1988).
[58] J. G. Rosa and S. R. Dolan, Massive vector fields on the Schwarzschild spacetime: quasi-normal modes and bound states, Phys. Rev. D **85**, 044043 (2012), arXiv:1110.4494 [hep-th].
[59] J. P. Conlon and C. A. Herdeiro, Can black hole superradiance be induced by galactic plasmas?, Phys. Lett. B **780**, 169 (2018).
[60] A. Dima and E. Barausse, Numerical investigation of plasma-driven superradiant instabilities, Class. Quant. Grav. **37**, 175006 (2020), arXiv:2001.11484 [gr-qc].
[61] E. Cannizzaro, A. Caputo, L. Sberna, and P. Pani, Plasma-photon interaction in curved spacetime: Formalism and quasibound states around nonspinning black holes, Physical Review D **103**, 10.1103/physrevd.103.124018 (2021).
[62] E. Cannizzaro, A. Caputo, L. Sberna, and P. Pani, Plasma-photon interaction in curved spacetime. II. Collisions, thermal corrections, and superradiant instabilities, Phys. Rev. D **104**, 104048 (2021), arXiv:2107.01174 [gr-qc].
[63] B. Cecconi, Goniopolarimetry: Space-borne radio astronomy with imaging capabilities, C. R. Phys. **15**, 441 (2014).
[64] B. Cecconi, M. Dekkali, C. Briand, B. Segret, J. N. Girard, A. Laurens, A. Lamy, D. Valat, M. Delpech, M. Bruno, P. Gélard, M. Bucher, Q. Nenon, J.-M. Grießmeier, A.-J. Boonstra, and M. Bentum, Noire study report: Towards a low frequency radio interferometer in space, 2018 IEEE Aerospace Conference , 1 (2018).
[65] LOFAR Imaging capabilities and sensitivity, `https://science.astron.nl/telescopes/lofar/lofar-system-overview/observing-modes/lofar-imaging-capabilities-and-sensitivity/`, [Accessed: 11-April-2024].
[66] A. M. Green and B. J. Kavanagh, Primordial black holes as a dark matter candidate, J. Phys. G Nucl. Part. Phys. **48**, 043001 (2021).
[67] Y. Sofue, Rotation curve of the milky way and the dark matter density (2020), arXiv:2004.11688 [astro-ph.GA].
[68] M. I. R. Alves, F. Boulanger, K. Ferrière, and L. Montier, The Local Bubble: a magnetic veil to our Galaxy, aap **611**, L5 (2018), arXiv:1803.05251 [astro-ph.GA].
[69] C. F. McKee and J. P. Ostriker, A theory of the interstellar medium: three components regulated by supernova explosions in an inhomogeneous substrate., Astrophys. J. **218**, 148 (1977).